ALMA MATER STUDIORUM
UNIVERSITÀ DI BOLOGNA

DEPARTMENT OF PHYSICS AND ASTRONOMY ”A. RIGHI”

SECOND CYCLE DEGREE

PHYSICS

Surface Guided Radiotherapy for Breast in Deep Inspiration Breath Hold: Sentinel® Validation and Dosimetric Impact

Research Conducted at the Istituto Romagnolo per lo Studio e la Cura dei Tumori “Dino Amadori” in Meldola (April–August 2025)

Supervisor:	**Defended by:**
Dr. Roberto Spighi	**Letizia Frassineti**

Co-supervisors:

Dr. Anna Sarnelli
Dr. Giacomo Feliciani

Graduation Session: 25-26 September 2025

Academic Year 2024/2025

To Giulia, Silvia, Anna, and
to all the women who silently fight
against diseases invisible to the eye.
This work is for you.

Abstract

Surface guided radiotherapy, a tracking technique that reconstructs the three-dimensional surface of the patient in real time using optical imaging, is nowadays used to improve patient positioning accuracy, speed up workflows, and potentially lower imaging dose by reducing cone beam imaging checks before treatment delivery. This thesis analyzes its use for left-sided breast treatment in deep inspiration breath hold in a retrospective cohort of 35 patients, asking if the system is reliable and if residual positioning errors have a dosimetric impact on treatment quality. The vertical elevation of the primary gating point recorded by the Sentinel® system at simulation, defined as the difference in chest-wall elevation between free breathing and deep inspiration breath hold respiratory conditions, was validated against the elevation measured between the computed tomography acquired in free breathing and deep inspiration breath hold. The two measures showed a high level of agreement, confirming the reliability of the Sentinel® system for motion tracking. Residual positioning errors, verified with cone beam imaging before treatment, were generally small but variable, with some shifts and rotations large enough to affect target coverage and organ at risk doses. The recalculation of the treatment plans using the average shifts found during the treatment course with the cone beam imaging, confirmed that most cases maintained adequate dose coverage, while some patients showed underdosage of the breast and an increase in cardiac and contralateral breast doses. A 3D gamma analysis, a standard tool to compare planned and recalculated dose distributions, highlighted that while some patients retained near perfect agreement between the original and the recalculated plan, others experienced relevant degradation. Overall, surface guided radiotherapy provides accurate, non ionizing positioning, but inter-patient variability persists, suggesting a strategy of early imaging verification, robustness checks, and individualized imaging frequency.

Sommario

La radioterapia guidata dalla superficie, una tecnica di tracciamento che ricostruisce in tempo reale la superficie tridimensionale del paziente mediante imaging ottico, è oggi utilizzata per migliorare l'accuratezza del posizionamento dei pazienti, rendere più rapido il workflow e, potenzialmente, ridurre la dose da imaging grazie a un minor numero di controlli con tomografia computerizzata a fascio conico prima della somministrazione del trattamento. Questa tesi analizza l'utilizzo della radioterapia guidata dalla superficie per il trattamento della mammella sinistra in apnea inspiratoria profonda, in una coorte retrospettiva di 35 pazienti, con l'obiettivo di valutarne l'affidabilità e verificare se gli errori residui di posizionamento abbiano un impatto dosimetrico sulla qualità del trattamento. L'elevazione verticale del punto di gating primario, registrata dal sistema Sentinel® durante la tomografia computerizzata di pianificazione e definita come la differenza nell'elevazione del torace tra le condizioni di respiro libero e apnea inspiratoria profonda, è stata confrontata con l'elevazione misurata sulle corrispondenti tomografie computerizzate acquisite in respiro libero e in apnea inspiratoria profonda. La concordanza tra le due misure è risultata buona, confermando l'affidabilità del sistema Sentinel® nel tracciamento del movimento respiratorio. Gli errori residui di posizionamento, verificati con tomografia computerizzata a fascio conico prima del trattamento, sono risultati generalmente piccoli ma variabili, con alcune traslazioni e rotazioni sufficientemente grandi da influenzare la copertura del bersaglio e la dose agli organi a rischio. Il ricalcolo dei piani di trattamento, basato sulle traslazioni medie riscontrate durante il corso della terapia con tomografia computerizzata a fascio conico, ha confermato che nella maggior parte dei casi è stata mantenuta una buona copertura di dose, mentre in alcuni pazienti si è osservato un sottodosaggio della mammella e un aumento della dose al cuore e alla mammella controlaterale. Un'analisi gamma 3D, strumento standard per confrontare la distribuzione di dose pianificata con quella ricalcolata, ha evidenziato che in alcuni pazienti vi era un accordo perfetto tra il piano originale e quello ricalcolato, mentre in altri si osservava una degradazione rilevante. Complessivamente, la radioterapia guidata dalla superficie rappresenta un metodo accurato e non ionizzante per il posizionamento del paziente, ma persiste una variabilità tra pazienti che suggerisce l'adozione di una strategia basata su verifica precoce con imaging, controlli di robustezza del piano di trattamento e una frequenza di imaging personalizzata.

Contents

List of Figures

List of Tables

Introduction

Breast cancer is one of the most common oncological diseases worldwide and a major health issue for the female population. Radiotherapy is a fundamental part of the management of this disease, both in adjuvant and, in selected cases, in radical settings. The technological evolution in the field of radiation oncology has led to the development of increasingly precise treatment techniques, aimed at maximizing tumor control while minimizing irradiation of surrounding healthy tissues and organs at risk.

In left-sided breast cancer, one of the main challenges is the reduction of radiation dose to the heart, the left anterior descending coronary artery (LAD), and the controlateral breast. Deep inspiration breath hold technique has been introduced to address this issue, due to the anatomical displacement of the heart and LAD away from the chest wall during deep inspiration. This approach has been shown to significantly reduce the exposure to organs at risk without compromising target coverage.
In this context, surface guided radiotherapy, which is an optical surface tracking system that reconstructs the three-dimensional surface of the patient in real time using optical imaging without the need for external markers such as tattoos or the use of ionizing radiations, has emerged as a method that improves the precision of patient positioning and allows intrafraction motion monitoring, since it has the ability to interrupt the radiation beam when thresholds of motion are exceeded. By integrating systems such as Sentinel® and Catalyst®, surface guided radiotherapy allows for real-time monitoring of the patient's surface and respiratory pattern. The Sentinel® system, typically installed in the computed tomography simulation room, uses structured light projection and stereoscopic cameras to acquire a high resolution model of the patient's external surface and to record the respiratory signal during simulation. This information is important to define the reference surface and the gating parameters that will be used during treatment; while the Catalyst® system, positioned in the treatment room, is an optical surface scanner that allow to perform patient positioning corrections in six degrees of freedom and that continuously monitors the respiratory motion during beam delivery, automatically enabling or interrupting irradiation according to the predefined gating window. Together, these two systems create a fully integrated surface guided radiotherapy workflow. In clinical practice, visual and audio coaching are used to standardize breath holds, and a patient-

specific gating window is defined at simulation, and the primary gating point is placed reproducibly, ideally at the xiphoid, which is the cartilaginous section at the lower end of the sternum not attached to any ribs.

Despite the clinical adoption of surface guided radiotherapy in many centers, the geometric reliability of surface imaging devices and their dosimetric impact under realistic treatment conditions require systematic evaluation. In particular, understanding the correlation between external surface tracking and internal anatomical positioning, as well as quantifying the potential deviations introduced by translational and rotational setup errors, is important to assess whether the positioning achieved through surface guided radiotherapy can consistently reproduce the intended treatment geometry. Moreover, it is important to determine whether residual setup uncertainties, even if within clinically acceptable tolerances, could lead to dose distribution changes large enough to compromise target coverage or increase the exposure of organs at risk. Addressing these questions is essential to ensure that surface guided radiotherapy can be reliably used as a positioning method, reducing or even eliminating the need for tattoos, lasers, and additional imaging procedures.

The aim of this work is to perform a comprehensive validation of the Sentinel® system, assessing its geometric accuracy in reproducing the true anatomical elevation of the primary gating point, which is the difference in elevation between the free breathing and deep inspiration breath hold respiratory conditions. Furthermore, dosimetric assessments are conducted to quantify the impact of measured positioning errors and simulated rotational deviations on treatment plan quality, using three-dimensional gamma analysis. This method, widely adopted in radiotherapy, provides a quantitative metric that evaluates dose differences and spatial deviations between dose distributions. In this work, it was applied to compare the original treatment plan with recalculated plans that incorporated the average positioning shifts observed during treatment, thereby offering a measure of agreement. The study also investigates the relationship between breast volume, setup accuracy, and dosimetric robustness, providing additional insight into potential patient-specific predictors of surface guided radiotherapy performance.
Methodologically, the study integrates computed tomography based surface projections, time-series analysis of the primary gating point (including heartbeat extraction), and plan recalculation with isocenter offsets, complemented by three-dimensional gamma evalu-

ation. All the analyses were conducted, under institutional approval, using routine clinical data of a cohort of 35 patients with left-sided breast cancer, treated at the IRCCS Istituto Romagnolo per lo Studio dei Tumori IRST “Dino Amadori” in Meldola (FC), Italy, between October 2024 and May 2025.

The thesis is organized into five chapters, each addressing a specific aspect of the research and progressing from the theoretical background to the experimental analyses.
Chapter 1 provides an overview of the theoretical and clinical foundations of radiotherapy, with a focus on breast cancer, treatment planning principles, and an introduction of the deep inspiration breath hold technique, while chapter 2 describes in detail the clinical workflow of surface guided radiotherapy, explaining how Sentinel® and Catalyst® systems are integrated from the computed tomography simulation to treatment delivery.
The experimental core of the thesis is presented in Chapters 3 to 5. Chapter 3 presents the geometric validation of the Sentinel® system, including respiratory stability analysis, evaluation of geometric accuracy, and comparison with data from the literature to contextualize the findings.
Chapters 4 and 5 provide a comprehensive evaluation of the clinical performance of surface guided radiotherapy under real treatment conditions.
In particular, chapter 4 reports the analysis performed after cone beam computer tomography based setup verification, quantifying the residual translational and rotational errors following the initial surface guided alignment. The results are examined in relation to clinical thresholds, compared with previously published data, and statistically analysed to investigate correlations with patient-specific anatomical factors.
In the end, chapter 5 presents the dosimetric evaluation through dose-volume histograms and three-dimensional gamma analysis, assessing the impact of simulated translational and rotational setup errors on the delivered dose distribution. Both local (5% dose threshold / 3 mm distance to agreement) and global (3% of the maximum dose / 2 mm distance to agreement) gamma criteria are applied, with and without the exclusion of a peripheral shell of the breast, in order to evaluate the magnitude of the discrepancies.

Through this approach, the thesis aims to provide a clinically oriented assessment of surface guided radiotherapy in left-sided breast cancer, highlighting its potential to improve treatment precision, reduce radiation exposure to critical organs, and support its integration as a reliable standard in modern radiotherapy workflows.

1 Theoretical and Clinical Foundations of Radiotherapy

This chapter provides an overview of the fundamental principles behind radiotherapy, starting from the interaction mechanisms between photons and matter, which explain how radiation deposits energy within biological tissues. These physical processes form the basis for the clinical application of radiotherapy, where accurate treatment planning and dose calculation are essential to deliver effective and safe treatments.
In this context, dosimetric quantities used to quantify energy deposition and assess biological impact are also discussed.

The second part of the chapter focuses on the clinical implementation of these principles, and introduces the main radiotherapy planning techniques used in current practice, like three-dimensional conformal radiotherapy (3D-CRT) and volumetric modulated arc therapy (VMAT).
The chapter concludes with a focus on breast cancer: treatment protocols, positioning strategies, and the dosimetric challenges specific to breast irradiation are presented. Furthermore, deep inspiration breath hold (DIBH) is presented as a promising technique used to reduce cardiac dose during left-sided breast treatments by increasing the distance between the heart and the irradiated volume.

1.1 Photons Interactions with Matter

When a photon beam passes through a medium, its intensity is attenuated as a function of the thickness x of the crossed material. This attenuation follows an exponential law that depends on the physical properties of the medium:

$$N = N_0 \cdot e^{-\mu x} \tag{1.1}$$

with

$$\mu = \frac{N_A}{A} \cdot \rho \cdot \sigma \tag{1.2}$$

where N_0 is the number of the incident photons, μ is the absorption coefficient, N_A is the Avogadro's number, A is the atomic mass number, ρ is the density of the crossed material and σ is the cross section. Equation 1.1 is known as the Beer-Lambert Law.

However, since μ depends on the material's density, it can be difficult to compare different substances directly. For this reason the mass attenuation coefficient $\frac{\mu}{\rho}$ is often used, as it expresses the attenuation per unit mass and facilitates the comparison of photon interactions across different materials, independently of their physical density.

At the energies typically used in radiotherapy (ranging from a few hundred keV to several MeV), electromagnetic radiation interacts with target atoms through the three main ionization processes showed in Figure 1.1:

- photoelectric effect;
- Compton scattering;
- pair production.

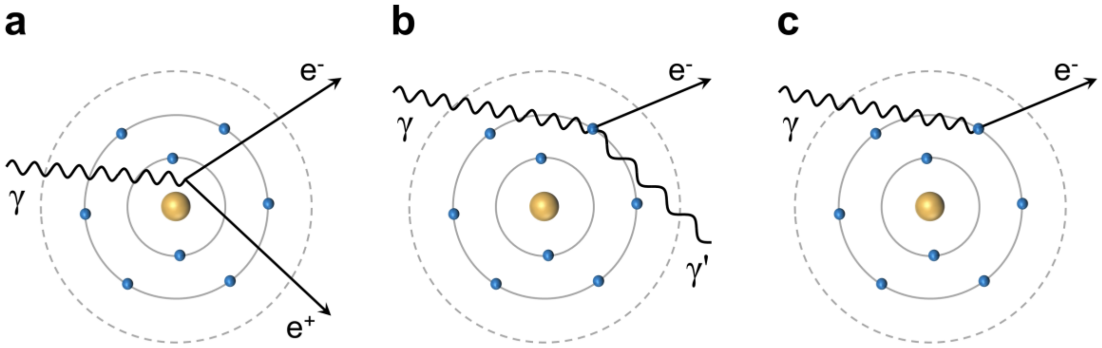

Figure 1.1: Schematic representation of [A] pair production, [B] Compton scattering and [C] photoelectric effect [1].

The attenuation of the electromagnetic beam, due to the combined effect of these interactions, is given by:

$$N = N_0 \cdot e^{-\mu_{\text{tot}} x} \tag{1.3}$$

with

$$\mu_{\text{tot}} = \mu_{\text{photoelectric}} + \mu_{\text{Compton}} + \mu_{\text{pairproduction}} \tag{1.4}$$

since each of these phenomena is characterized by its own cross section and absorption coefficient [2].

1.1.1 Photoelectric Effect

When a photon (E_γ) interacts with a bound electron, it may transfer enough energy to overcome the electron's binding energy (E_b), resulting in its ejection from the atom with a kinetic energy (E_{kin}) equal to the difference between the photon energy and the binding energy:

$$E_{\text{kin}} = E_\gamma - E_b \tag{1.5}$$

This ionization process creates a vacancy in an inner shell, which is filled by an electron from a higher shell, and the atom reorganizes into a more stable configuration.The excess energy generated by the electron transition can be released in two ways:

- through the emission of a characteristic X-ray photon;
- in atoms with a low atomic number, by transferring this energy to another electron, which is then ejected as an Auger electron.

The cross section of the photoelectric effect increases with the atomic number Z of the material and decreases as the photon energy E_γ increases:

$$\sigma \propto \frac{Z^4}{{E_\gamma}^{\frac{7}{2}}} \tag{1.6}$$

1.1.2 Compton Scattering

Compton scattering is an elastic collision that occurs when an incident photon interacts with a weakly bound or quasi-free electron. During the interaction, the photon transfers part of its energy to the electron, which is then ejected with a kinetic energy, and the photon is scattered at an angle that determines the resulting change in its wavelength. The differential cross section $\frac{d\sigma}{d\Omega}$ of this process is given by the Klein-Nishina formula [3]:

$$\frac{d\sigma}{d\Omega} = \frac{r_e^2}{2}\left(\frac{E'}{E}\right)^2\left(\frac{E'}{E} + \frac{E}{E'} - \sin^2\theta\right) \tag{1.7}$$

with

$$E' = \frac{E}{1 + \frac{E}{m_e c^2}(1 - \cos\theta)} \tag{1.8}$$

where r_e is the classical electron radius, E is the initial energy of the incident photon, E' is the energy of the scattered photon and θ is the scattering angle of the photon.

The Compton cross section per atom is independent of the mass atomic number Z and depends only on the photon energy E; however, when considering photon attenuation in bulk materials:

$$\sigma \propto \frac{Z}{E} \tag{1.9}$$

This is because the number of electrons per unit mass scales with Z, while the interaction cross section per electron decreases as the photon energy E increases.

1.1.3 Pair Production

When a gamma photon has an energy $E \geq 1.02$ MeV, it can interact with the electromagnetic field of a nucleus, resulting in the creation of an electron–positron (e^-e^+) pair. In this process, the photon's energy E is converted into the rest mass of the two particles $2m_ec^2$, while the excess energy is distributed as kinetic energy between the two particles ($K_{\text{pair}} = K_{e^-} + K_{e^+}$) and the recoil nucleus (K_{recoil}):

$$E = 2m_ec^2 + K_{\text{pair}} + K_{\text{recoil}} \tag{1.10}$$

The produced electron loses energy through ionization, while the positron, after encountering an electron, undergoes annihilation, typically resulting in the emission of two 511 keV photons in opposite directions.

At photon energies up to a few tens of MeV, the cross section for pair production can be approximated by:

$$\sigma \propto Z^2 \ln(E) \tag{1.11}$$

At higher energies, on the order of hundreds of MeV, the dependence becomes approximately linear:

$$\sigma \propto Z^2 \tag{1.12}$$

1.1.4 Energy Dependence of Photon-Matter Interactions

Figure 1.2 illustrates the energy dependence of the three main photon interaction mechanisms.

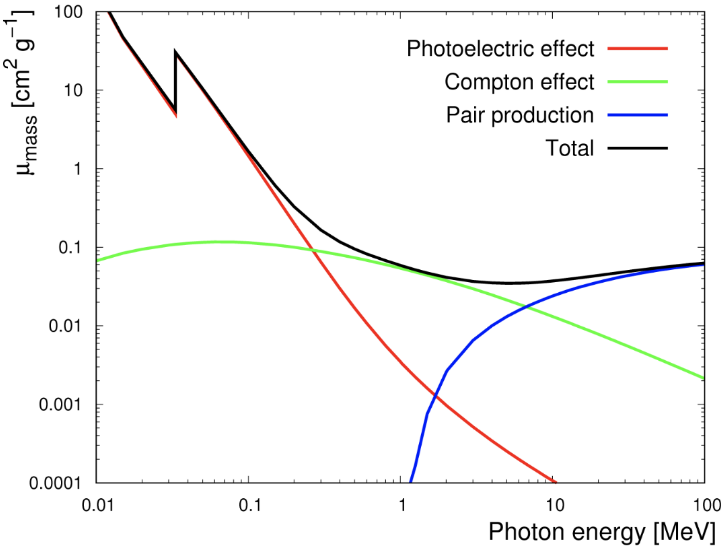

Figure 1.2: Energy dependence of the three main photon interaction processes in matter [4].

- At low photon energies, the photoelectric effect dominates, particularly in materials with an high atomic number Z.
- As energy increases, Compton scattering becomes the prevailing interaction, especially in soft tissues; in fact, it is the most relevant process in the energy range of clinical radiotherapy.
- At higher energies (above 1.022 MeV), pair production contributes significantly, especially in dense materials or in high-energy treatment modalities.

1.2 Principles of Radiotherapy

Radiotherapy is one of the most common methods of cancer treatment, and it can be used alone or in combination with surgery and chemotherapy, depending on the type and stage of the disease. The aim of radiotherapy is to destroy cancer cells while preserving healthy tissues as much as possible.

The radiotherapy process begins with the spatial localization of the tumor within the patient's body; then the planning target volume (PTV), showed in Figure 1.3, is defined during the treatment planning phase. This volume includes the entire three-dimensional shape of the tumor (gross tumor volume, GTV), surrounding tissues potentially affected by microscopic disease (clinical target volume, CTV), and an additional safety margin to account for positioning and delivery uncertainties.

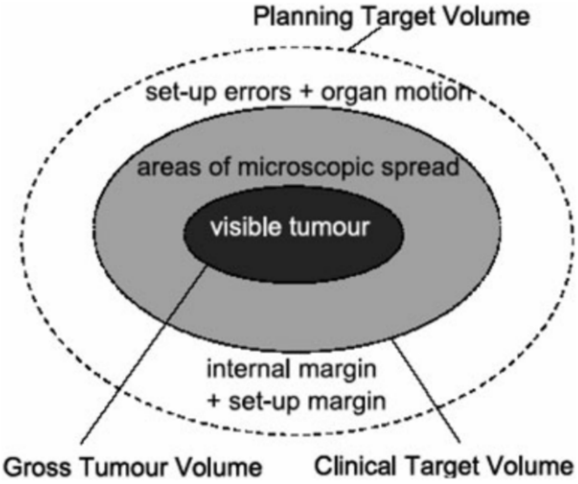

Figure 1.3: Definition of the planning target volume (PTV) from the gross tumor volume (GTV) [5].

Once the PTV is established, a treatment planning system (TPS) is used to determine the optimal irradiation strategy. This includes the selection of the number, type, energy, intensity, and angles of the radiation beams, in order to ensure the maximum dose is delivered to the target while minimizing exposure to healthy tissues.

The most commonly used planning techniques include:

- **Three-dimensional conformal radiotherapy (3D-CRT)**:
  a technique that uses multiple fixed beams shaped to match the tumor geometry.
- **Volumetric modulated arc therapy (VMAT)**:
  a type of therapy that delivers radiation continuously as the machine rotates around the patient, modulating beam intensity and shape in real time.

1.2.1 Fundamentals of Radiation Dosimetry

As explained in subsection 1.1, when ionizing radiation interacts with matter, part of its kinetic energy is transferred to the electrons of the medium.

These electrons are then set in motion, initiating a cascade of interactions within the irradiated tissue. As they travel, they can lose energy through collisions with other electrons or by emitting secondary radiation such as bremsstrahlung X-rays.

The absorbed dose D_R is defined as the amount of energy deposited by ionizing radiation per unit mass of a material. It is given by the ratio between the differential energy dE imparted to an infinitesimal mass element dm:

$$D_R = \frac{dE}{dm} \tag{1.13}$$

The absorbed dose D_R is measured in Gray (Gy) where $1Gy = 1\frac{J}{kg}$.

The absorbed dose represents the dosimetric quantity used to quantify the energy deposited at each point along the path of the radiation beam. However, as a purely physical measure, the absorbed dose is not sufficient to accurately describe the resulting biological effects.

The equivalent dose D_{eq} is introduced to account for the potential biological impact of different types of radiation, and is calculated by weighting the absorbed dose D with a radiation weighting factor ω_R, which is typically equal to 1 for photons.

$$D_{\text{eq}} = \sum_R w_R \cdot D_R \tag{1.14}$$

Since $\omega_R \approx 1$ for photons, the equivalent dose numerically coincides with the absorbed dose, but it is expressed in Sievert (Sv) instead of Gray (Gy).

A more accurate estimate of the biological impact of radiation can be obtained by accounting for the different radiosensitivities of various tissues.

Table 1.1 shows some of the tissue weighting factors ω_T, established by international guidelines for clinical radiation safety. These factors are used to calculate the effective dose D_{eff}, which reflects not only the absorbed dose D_R but also the varying biological response of each organ or tissue type.

Tissue	w_T
Gonads	0.20
Red bone marrow, colon, lung, stomach	0.12
Heart, kidneys, pancreas	0.12
Bladder, esophagus, liver, thyroid	0.04
Bone surface, skin, brain	0.01

Table 1.1: Tissue weighting factors w_T used for the calculation of the effective dose, as recommended by international radiological protection guidelines [6].

Thus, the effective dose D_{eff} is defined as:

$$\begin{aligned} D_{\text{eff}} &= \sum_T w_T \cdot D_{\text{eq}} \qquad (1.15) \\ &= \sum_T w_T \cdot \sum_R w_R \cdot D_R \qquad (1.16) \end{aligned}$$

This quantity, expressed in Sieverts (Sv), provides a more comprehensive estimate of the biological impact of the radiation, and accounts for both the type of radiation and the radiosensitivity of different tissues.

1.2.2 Radiation-Induced Cellular Effects: DNA and Intracellular Damage

During the treatment phase, cancer cells are targeted by the incident radiation and led to death through intracellular damage mechanisms; in fact, their genetic code, which carries the instructions responsible for the disease, can be disrupted either directly by ionization or indirectly through the action of free radicals generated by the radiolysis of water molecules.

The deoxyribonucleic acid (DNA) is a double-helix molecule composed of two antiparallel chains of nucleotides, each consisting of a phosphate group, a deoxyribose sugar, and one of the four possible nitrogenous base (adenine (A), thymine (T), cytosine (C), and guanine (G)). These bases are paired through hydrogen bonds (A with T, and C with G), and they encode the genetic information of the cell [7].
When cells are exposed to ionizing radiation, two main types of DNA damage can occur: single-strand breaks (SSBs) and double-strand breaks (DSBs), illustrated in Figure 1.4.

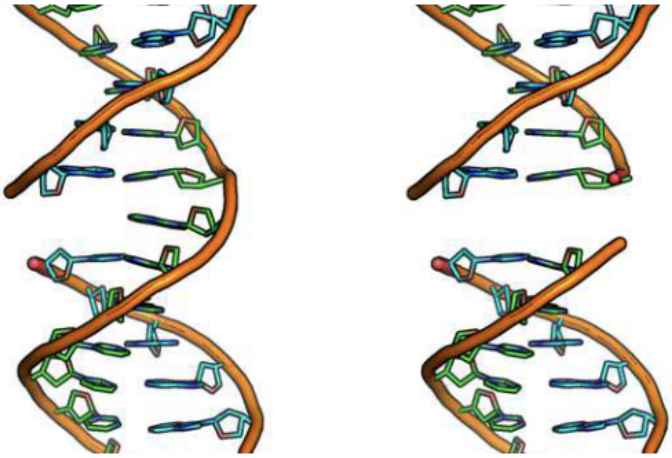

Figure 1.4: Representation of single-strand breaks (left) and double-strand break (right).

- **Single-strand breaks (SSBs):** involve damage to only one of the two DNA strands, and those damages are typically repairable by the cell using the intact complementary strand as a template.
  They are the most common form of radiation-induced damage and occur at a rate of approximately 1000 SSBs per Gy of radiation, with a frequency that increases linearly with the absorbed dose.
- **Double-strand breaks (DSBs):** occur when both strands of DNA are broken at the same location. These damages are more cytotoxic and difficult to repair, and often result in irreversible outcomes such as cell death or genetic mutations. Approximately 50–100 DSBs are induced per Gy of radiation.

Depending on the extent and type of damage, the biological effects may be:

- lethal, leading to irreversible cell death;
- sublethal, if the damage is repairable by enzymatic mechanisms;
- potentially lethal, if the damage could be repaired given favorable post-irradiation conditions [8].

Since the human body is primarily composed of water, the indirect effects of ionizing radiation can be modeled by considering the interaction between a water molecule (H_2O) and an incident gamma photon in the energy range of 5–10 MeV.

The incident photon ionizes the water molecule, which ejects an electron (e^-) and forms a positively charged water ion (H_2O^+):

$$H_2O + \gamma \longrightarrow H_2O^+ + e^-$$

After its emission, the electron (e^-) gradually loses energy as it travels through the medium and may eventually be captured by another water molecule, resulting in the formation of a transient negative ion (H_2O^-):

$$H_2O + e^- \longrightarrow H_2O^-$$

The produced positive (H_2O^+) and negative (H_2O^-) water ions dissociate through the following reactions:

$$H_2O^+ \longrightarrow H^+ + OH^\circ$$
$$H_2O^- \longrightarrow OH^- + H^\circ$$

Thus, the final products of water radiolysis are one hydrogen ion (H^+), one hydroxide ion (OH^-), and two neutral free radicals: the hydroxyl radical (OH°) and the hydrogen radical (H°).

In this scenario, multiple chemical reactions can take place, and some of them may ultimately lead to the death of the cell where radiolysis has occurred; for example:

$$H^\circ + OH^\circ \longrightarrow H_2O \qquad \text{innocuous reaction}$$
$$OH^\circ + OH^\circ \longrightarrow H_2O_2 \qquad \text{harmful reaction}$$

However, cells are equipped with a natural defense mechanisms that regulate the production and elimination of reactive species; in fact, specific enzymes can mitigate the cytotoxic effects of free radicals.

For example, catalase catalyzes the following reaction:

$$2\,H_2O_2 \longrightarrow 2\,H_2O + O_2$$

thereby dissociating and neutralizing hydrogen peroxide.

The impact of free radicals depends on the balance between their production and the cell's ability to neutralize them, and exposure to external sources like therapeutic radiation can disrupt this balance, causing oxidative stress and potential cellular damage.

To reduce side effects on healthy tissues and improve treatment outcomes, radiotherapy techniques have become increasingly precise. This evolution has led to the development of approaches that allow for better control of the dose delivered to the tumor.

1.2.3 Three-Dimensional Conformal Radiotherapy (3D-CRT)

Three-Dimensional Conformal Radiotherapy (3D-CRT), showed in Figure 1.5, was introduced at the beginning of the '90s as a promising technique that allowed the dose distribution to conform more accurately to the shape of the tumor, compared to the traditional two-dimensional techniques that had been employed until that time.
A field denotes a stationary beam delivered at a fixed gantry angle with a fixed collimator aperture; the gantry does not move while the beam is on. 3D-CRT delivers dose with a small number of fixed fields, and during each field the gantry is stationary and the multileaf collimator (MLC) is used to conform the aperture to the planning target volume, so the leaf positions remain static while the beam is on.

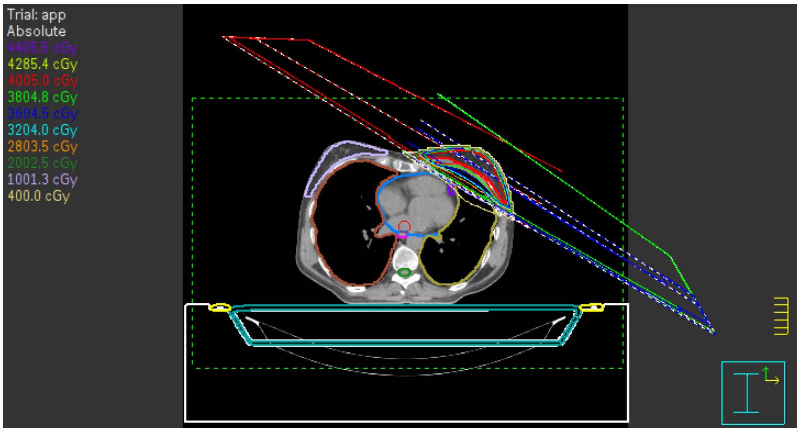

Figure 1.5: Example of a breast radiotherapy treatment plan using three-dimensional conformal radiotherapy (3D-CRT).

The major advantage of 3D-CRT is that radiation beams can be shaped and directed on the basis of detailed imaging data, typically from computed tomography (CT). This enables improved dose homogeneity within the planning target volume, and the isodose distribution is conformed to the three-dimensional geometry of the tumor, reducing un-necessary irradiation to healthy tissue.

However, this technique is sensitive to organ motion and setup uncertainties; thus, to compensate, slightly larger treatment volumes may be irradiated to maintain appropriate target coverage throughout the treatment course.

To ensure accurate and safe dose delivery, clinical protocols typically define standardized beam arrangements, establish appropriate margins from the clinical target volume to the planning target volume, and set dose constraints for nearby organs at risk (OARs), including the ipsilateral lung, heart, the left anterior descending artery (LAD), and the contralateral breast [9].

1.2.4 Volumetric Modulated Arc Therapy (VMAT)

The first type of arc therapy, known as intensity modulated arc therapy (IMAT), was first described in 1995 [10]. This technique required the use of multiple superimposed arcs to achieve a clinically acceptable dose distribution.

Volumetric modulated arc therapy (VMAT), introduced in 2007, represented a significant evolution by allowing the simultaneous modulation of three key parameters during treatment delivery:

- gantry rotation speed;
- dose rate;
- shape of the treatment aperture, controlled by the movement of the multileaf collimator (MLC) leaves.

An arc denotes a continuous sweep of the gantry over a specified angular range during which dose is delivered, and along an arc, both the multileaf collimator (MLC) aperture and dose rate may vary.
Modern VMAT techniques enable the irradiation of the entire target volume using one or two arcs, although more complex clinical cases may require additional arcs.

In breast cancer radiotherapy, VMAT is an effective alternative to conventional radiotherapy (CRT), a technique that uses four to five non-coplanar fields. In fact, VMAT achieves similar target coverage, a slightly better dose conformity, and significantly reduces the dose to critical structures such as the ipsilateral lung and adjacent healthy breast tissue. Moreover, VMAT requires fewer monitor units and a shorter treatment time [11] [12].

Nowadays there are two most common VMAT techniques, showed in Figure 1.6 which differ primarily in the extent of arc coverage used during treatment:

- **Standard VMAT:** the gantry rotates over a wide angular range (typically 180°), allowing full modulation of dose delivery from multiple directions.
- **Butterfly VMAT:** employs one or more restricted arcs, avoiding certain beam angles to reduce radiation exposure to critical organs.

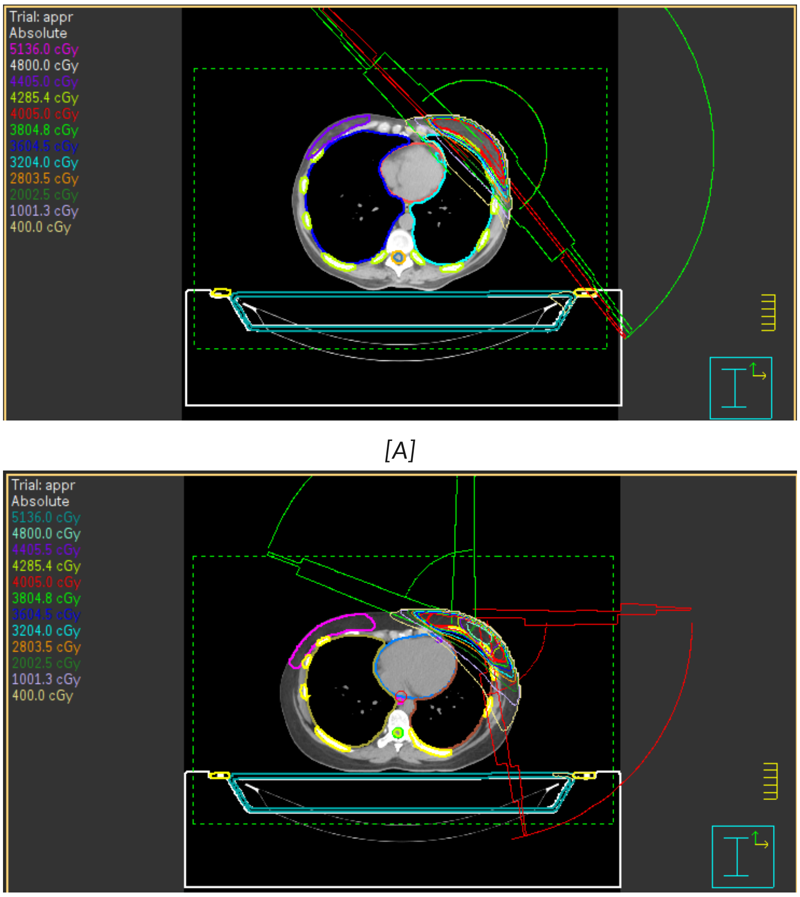

[A]

[B]

Figure 1.6: Comparison between [A] standard VMAT technique and [B] butterfly VMAT technique .

1.2.5 Hybrid Approach: Combination of 3D-CRT and VMAT

In clinical practice, during the last few years, it is common to combine 3D-CRT with VMAT in order to take advantage of the strengths of both techniques.

This hybrid approach, illustrated in Figure 1.7, allows for an initial conformal dose distribution using 3D-CRT beams, followed by a VMAT arc that refines the coverage and improves conformity, especially in regions close to organs at risk.

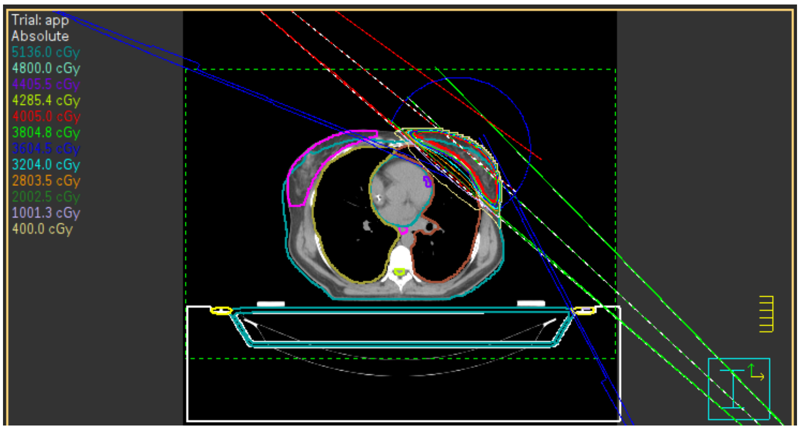

Figure 1.7: Example of a hybrid radiotherapy plan combining 3D conformal radiotherapy (3D-CRT) and volumetric modulated arc therapy (VMAT).

The 3D component provides a robust dose coverage, while the VMAT arc enables finer modulation to optimize dose distribution [13].

This technique can be particularly effective in complex breast cancer cases, where anatomical variations and proximity to OARs like the heart or LAD require careful dose shaping.

1.3 Breast Cancer and Radiotherapy

Breast cancer is the most common malignancy among female patients and it is the leading cause of cancer-related death in women. For example, according to national estimates for 2024, in Italy there were approximately 55900 new cases and 12500 deaths due to breast cancer, accounting for about 29.3% of female cancers [14].
In many European countries, the standard of care for breast radiotherapy is 40 Gy delivered in 15 fractions, with 2.7 Gy per fraction. For early-stage breast cancer, the FAST-

Forward trial validated the use of 26 Gy in 5 consecutive fractions, with 5.2 Gy per fraction [15]; this hypofractionated regimen requires higher precision because each fraction delivers a larger dose, with smaller safety margins and steeper dose gradients. In order to deliver the dose correctly and protect nearby organs like the heart and lungs, it is important to reduce both interfractional and intrafractional uncertainties [16].

1.3.1 The Patient Alignment

In clinical practice, the initial patient alignment in breast radiotherapy relies on skin tattoos to ensure reproducibility with the planning computed tomography (CT) scan. Typically, one anterior and two lateral tattoos are placed on the patient's skin and used as primary reference points for setup positioning, as the quality of the delivered treatment strongly depends on the ability to position the patient accurately and reproducibly throughout the course of radiotherapy [17].

To ensure that the tattoo locations are visible on the planning CT scan, small radiopaque markers, shown in Figure 1.8, are temporarily placed on the patient's skin by the radiation technologist and tattoos are then marked at those exact positions after the acquisition.

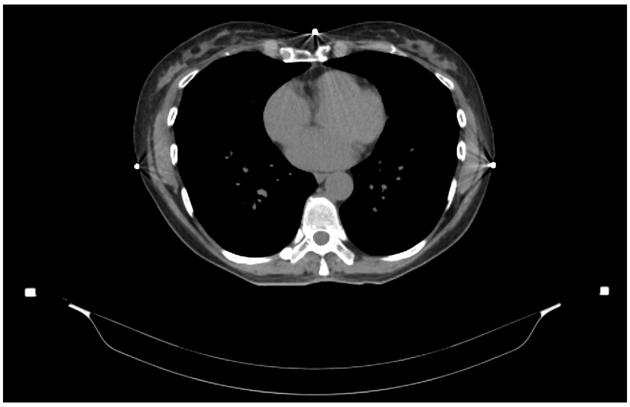

Figure 1.8: Axial CT slice displaying radiopaque skin markers, visible as distinct hyperdense dots on the patient's surface.

1.3.2 Clinical Challenges in Breast Radiotherapy

Tattoo-based setups present several challenges, such as skin mobility and the resulting variability in tattoo positions; in fact, radiation technologists often need to manipulate the skin to achieve proper patient alignment [15].

Moreover, tattoos do not provide any postural feedback regarding the position of the arm or chin, both of which can affect setup reproducibility and thus the accuracy of target positioning. Furthermore, in recent years, increased attention has also been given to the potential psychological impact of permanent tattoos on patients [18].

Moreover, it is important to highlight that setup reproducibility can be particularly challenging in patients with a higher body mass index or large and pendulous breasts. This is primarily due to the high deformability of breast tissue, which can result in variable positioning across treatment sessions. Such anatomical variations often require additional attention during patient setup to ensure an accurate dose delivery [19].

1.3.3 Dosimetric Advantages of Deep Inspiration Breath Hold Treatments

Deep inspiration breath hold (DIBH) is a technique that has been widely used in recent years to spare the dose to the heart in left-sided breast cancer.
DIBH is based on the observation that, during deep inspiration, the diaphragm flattens, the lungs expand, and the heart moves away from the chest wall, as shown in Figure 1.9.

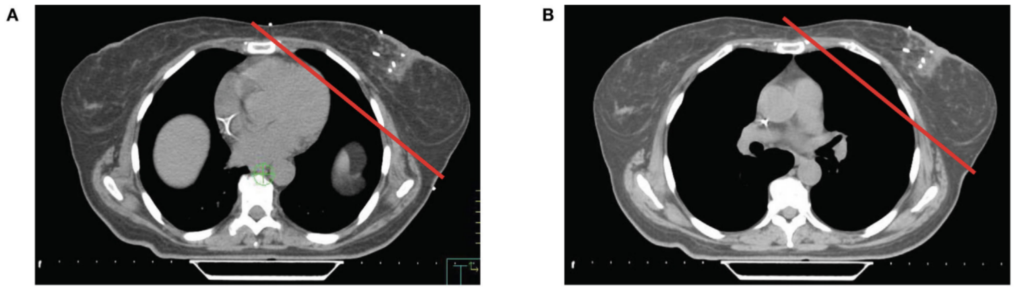

Figure 1.9: Axial CT slices from the same level of the breast in [A] free breathing and [B] DIBH CT scans [20].

By asking the patient to take a deep breath and hold it during both simulation and treatment, it is possible to increase the distance between the heart and the irradiated volume. This temporary anatomical shift allows for a significant reduction in the radiation dose delivered to the heart, lungs, controlateral breast and left anterior descending artery (LAD).

For example, Table 1.2 shows the reduction in mean dose to the heart and the LAD achieved with the use of DIBH compared to free breathing (FB) across multiple clinical studies.

Study	**Mean LAD dose (Gy)**			**Mean heart dose (Gy)**		
	FB	**DIBH**	**Reduction**	**FB**	**DIBH**	**Reduction**
[21]	11.4	5.5	52%	5.1	1.7	67%
[22]	26.3	16.0	39%	4.5	2.5	44%
[23]	14.9	4.0	73%	2.5	0.9	64%

Table 1.2: Summary of DIBH dosimetric benefits compared to FB.

Thus, numerous studies have demonstrated that DIBH leads to significant reductions in both mean heart dose and mean LAD dose, with respective decreases ranging from 25% to 67% and from 20% to 73% when comparing the same patients planned with free breathing and DIBH.

Nowadays there are two commonly used techniques for DIBH:

- **Moderate DIBH (mDIBH):** is an approach that uses active breathing control (ABC) devices, integrated with a spirometer, that can monitor the respiratory cycle and stop the airflow at a preset inspiratory threshold. The patient is required to hold its breath at that volume while the radiation beam is delivered, and this method ensures good reproducibility.
- **Voluntary DIBH (vDIBH):** is a technique in which the patient is coached to voluntarily hold their breath during deep inspiration. Respiratory motion is tracked using external systems that records chest displacements. The beam is automatically gated and interrupted if the breathing trace moves outside a defined threshold. This method, explained in section 2, is less invasive and commonly used in clinical practice.

Moderate DIBH (mDIBH) and voluntary DIBH (vDIBH) techniques achieve comparable dosimetric outcomes in terms of mean heart and LAD dose reduction, but vDIBH offers advantages in patient comfort, reduced setup time, and cost-effectiveness [20].

As radiotherapy is continuously evolving toward greater precision and personalization, the accurate monitoring of patient positioning and motion is becoming increasingly important. In this context, new technologies based on real-time surface tracking, such as surface-guided radiotherapy (SGRT), are becoming an effective way to improve treatment precision and ensure patient safety.

2 Principles of Surface Guided Radiotherapy in Breast Cancer

Surface guided radiotherapy (SGRT) is an optical surface tracking system that reconstructs the three-dimensional surface of the patient in real time using optical imaging without the need for external markers such as tattoos [15].

The main advantage of SGRT is that it is nonionizing, thus it can be used daily for initial positioning, continuous monitoring of intrafractional motion, and to interrupt the radiation beam when thresholds of motion are exceeded [24].

This chapter explains the clinical workflow of surface guided radiotherapy, highlighting its integration into the radiotherapy process from simulation to treatment delivery.

The entire SGRT process can be divided into key phases, each involving specific actions and parameters essential for accurate patient setup and motion monitoring, as shown in Figure 2.1.

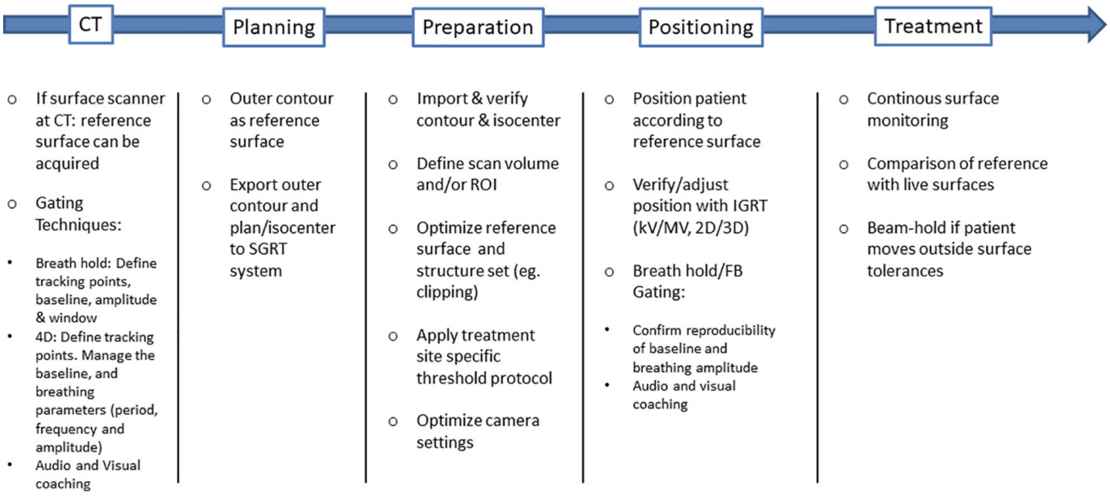

Figure 2.1: Diagram of a standard SGRT workflow and the main steps and parameters to be considered [25].

2.1 Planning Phase of Surface Guided Radiotherapy

This section describes the first part of the SGRT workflow, corresponding to the CT, Planning, and Preparation phases illustrated in Figure 2.1.

During these stages, the reference surface is acquired, and the surface data is integrated into the treatment planning system and surface tracking software. These steps are essential to establish a configuration that ensures accurate patient setup and motion monitoring through the course of radiotherapy.

2.1.1 Computed Tomography Simulation

The first use of computed tomography dates back to 50 years ago, and since then it has undergone significant improvements.
Modern multidetector CT (MDCT) systems, such as the one shown in Figure 2.2, enable fast acquisition of 3D images using multiple detector rows and a wide X-ray beam. Since their introduction in 1998, MDCT scanners have evolved from 4 to 320 detector rows, making it possible to scan the region of interest (ROI) at sub-millimeter resolution in a short time.

Figure 2.2: CT scan by Siemens® installed in "Istituto Romagnolo per lo Studio dei Tumori Dino Amadori".

During a CT scan, X-ray beams are attenuated as they pass through the body and are then detected by an array of detectors. The system acquires multiple projections that are reconstructed through an algorithm in order to generate image slices.

The resulting 3D CT dataset is composed of voxels, which are volumetric units defined in X, Y, and Z dimensions. The X and Y dimensions correspond to pixel size in the image plane, while the Z dimension represents slice thickness.
A CT number is assigned to each voxel on the basis of the average X-ray attenuation of the tissues it contains. These values are expressed in Hounsfield units (HU), a metric that allows the definition of the grayscale intensity of each pixel in the image, using water as the reference (0 HU) and air as -1000 HU [26].

A planning computed tomography (CT) scan is performed, after diagnosis, for all the patients that are eligible for radiotherapy. This scan is acquired in order to provide the anatomical information required for treatment planning, such as the target volumes and surrounding OARs.
The planning CT, which is acquired with the patient in treatment position, serve as the basis for the construction of a personalized treatment plan with one of the techniques explained in subsection 1.2. The spatial information obtained from the CT is used by the medical physicist to define the dose distribution and to determine the most appropriate beam configuration for each patient.

In the case of left-side breast cancer, the protocol establish that two CT scans must be acquired: one in free breath and one in deep inspiration breath hold; this dual-scan protocol allows for the creation of two separate treatment plans, enabling a dosimetric comparison and the selection of the optimal plan [27].

2.1.2 Sentinel® System and Reference Surface Acquisition

The Sentinel® system is a surface imaging device designed to be used in the radiotherapy workflows, in particular during the phase of the planning CT.

This system, illustrated in Figure 2.3, employs structured light projection and stereoscopic camera technology; in fact, a known light pattern is projected onto the patient's surface, and a camera capture its deformation to reconstruct a 3D surface model of the patient with high spatial resolution.

Sentinel® is used in the clinical workflow in order to enable accurate and reproducible patient positioning, and to acquire respiratory motion data that can be also used for both prospective and retrospective 4DCT image reconstruction:

- In prospective 4DCT the image acquisition is synchronized in real time with the patient's respiratory signal.
- In retrospective 4DCT the data is acquired continuously and then sorted into respiratory phases based on the recorded breathing trace.

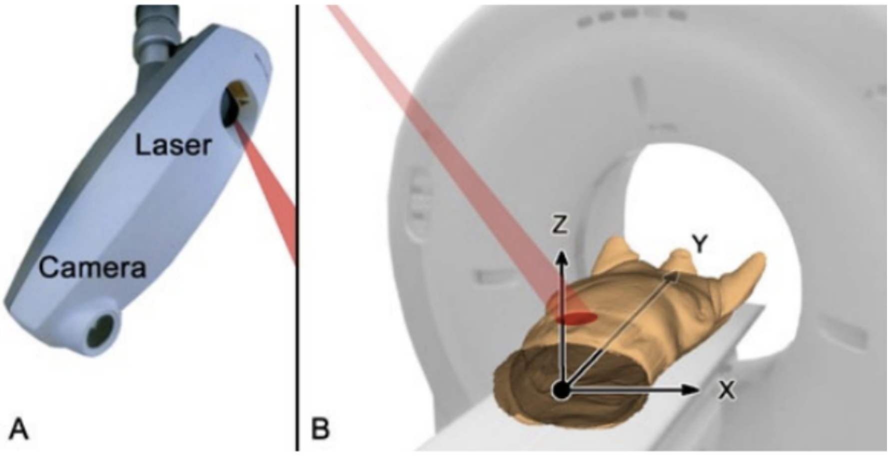

Figure 2.3: : (A) Sentinel® unit mounted at the ceiling and (B) patient setup and coordinate reference system [28].

Thus, this system provides information about the patient's external contour and respiratory pattern, but it does not directly localize internal anatomical structures.

During the acquisition of the planning CT for a patient with left-side breast cancer that will be treated in DIBH, the Sentinel® system is turned on, and the patient's surface is continuously monitored in real time.

A specific tracking point, called primary gating point, and corresponding to a circular surface of 30 mm of diameter, is selected by the radiation technologist on the surface of the anterior thoracic wall, in particular on the xiphoid process, which is the cartilaginous section at the lower end of the sternum not attached to any ribs.
This primary gating point, enhanced in red in Figure 2.4 [A], is placed with the Sentinel® software on the patient's surface in order to evaluate the vertical elevation of the location at which it is placed during the breathing cycle.

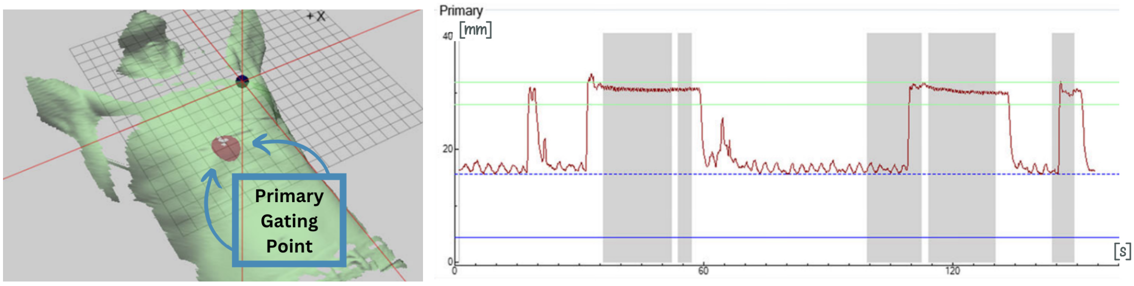

[A] *[B]*

Figure 2.4: Graphical demonstration of the c4D-tool: [A] the red point on the patients surface is the primary gating point for tracking the vertical amplitude during breath hold, and [B] is an amplitude over time plot reconstructed by the Sentinel® system [29].

The Sentinel® system records the respiratory trace obtained with the tracking of the vertical elevation of the primary gating point and displays the breathing curve shown in Figure 2.4 [B], in order to allow the evaluation of the amplitude, frequency, and stability of the respiratory pattern.

Before the acquisition of the CT, patients are asked to perform comfortable breath holds without any visual feedback, and this scheme is repeated few times in order to ensure consistency. On the basis of the vertical elevation recorded by the primary gating point during the training cycles, a patient-specific gating window that encompasses the amplitude range corresponding to the breath hold level is manually defined by the radiation technologist. This gating window is represented by two green lines in Figure 2.4 [B], and contains the part of the breathing curve that corresponds to the deep inspiration breath hold phases.

The accurate definition of the gating window is fundamental because it corresponds to the range of respiratory amplitude within which the radiation beam will be automatically enabled during treatment. In clinical practice, the gating window has a maximum width of 4 mm [30].

Once the optimal breath-hold reproducibility is achieved, the procedure is repeated with an audio and a visual feedback, as shown in Figure 2.5, and the planning CT scan is then acquired in DIBH under gated conditions.

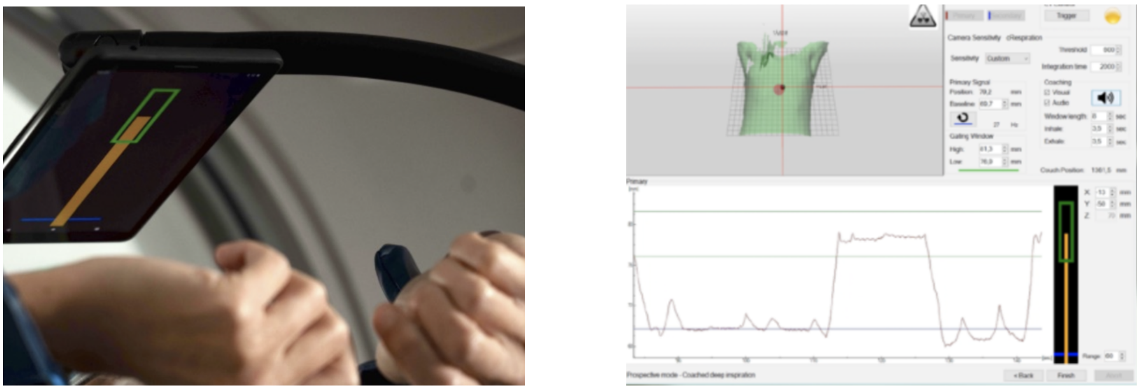

[A] *[B]*

Figure 2.5: The view of [A] the patient and [B] the radiation technologist during the planning CT scan [31].

This initial phase of the SGRT workflow is important for all subsequent steps in the treatment process; in fact, the data acquired at simulation will be used by the optical surface scanner Catalyst® in the treatment room to guide patient positioning and enable beam gating.

2.1.3 Data Export and Contour Definition

Once the surface and the respiratory curve are acquired, reference surface and gating parameters are saved and exported.

From the Sentinel® software, it is possible to export an `.xml` file containing all the information related to the patient's respiratory study; in particular:

- The minimum and maximum amplitude, measured in millimeters, of the gating window (highlighted in red in Figure 2.6).
- The baseline value (highlighted in blue in Figure 2.6), which represents the average elevation of the patient's respiratory signal during free breathing.
  Unlike the gating window, which is manually defined by the radiation technologist, the baseline is automatically calculated by the Sentinel® system from the initial breathing cycles recorded when the system is turned on.
- The vertical elevation of the primary gating point, sampled every 0.02 seconds, which defines the patient's breathing curve over time with high temporal resolution, as shown in Figure 2.6.

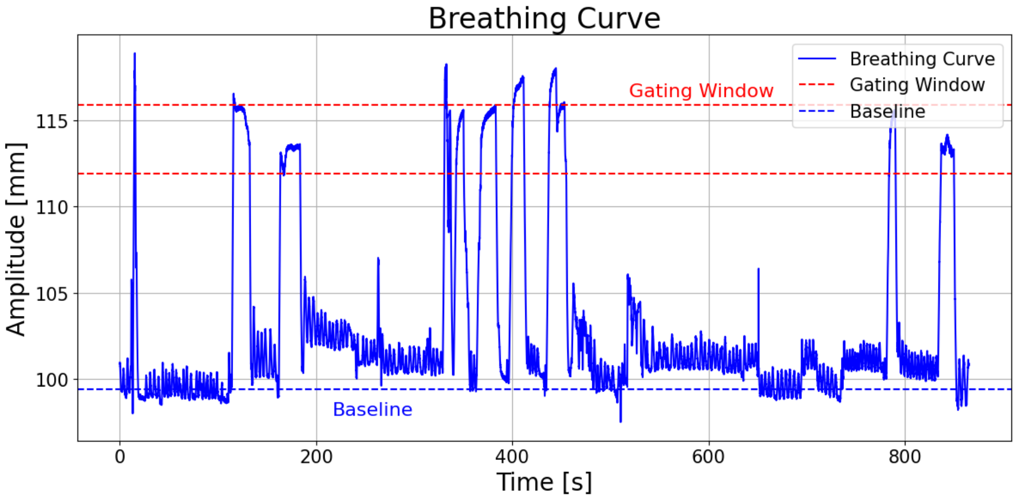

Figure 2.6: Breathing curve generated from the data acquisition of a real patient.

At this point the exported respiratory data and reference surface can be integrated into the treatment workflow.

Based on the CT images, the medical physicists and radiation oncologists can now define the most appropriate irradiation strategy and delineate the regions of interest (ROIs), including the target volumes and surrounding organs at risk.
The exported respiratory data and 3D surface are then transferred to the Catalyst® system, where they will be used for surface-based patient positioning and respiratory motion monitoring during the treatment phase.

2.2 Treatment Phase of Surface Guided Radiotherapy

This section focuses on the final part of the SGRT workflow, corresponding to the Positioning and Treatment blocks shown in Figure 2.1.

In this phase, the patient is aligned using the reference surface acquired during the planning CT scan, and real-time surface tracking is employed during the whole treatment session. Advanced SGRT systems such as Catalyst® enable precise patient setup verification and continuous intra-fraction motion monitoring, ensuring that radiation is delivered only when the vertical elevation of the primary point of the patient remains within the predefined gating window.

2.2.1 Initial Patient Alignment Techniques

In SGRT, patient alignment is firstly based on the comparison between the surface acquired in the treatment room and the reference surface exported during the planning CT. This method offers an anatomically accurate alternative to conventional tattoo-based alignment.

In clinical practice, especially in centers with recent SGRT installations, it is common to perform an initial alignment using tattoos and lasers, and once the patient is roughly positioned, the SGRT system is used for surface matching and postural corrections.

Figure 2.7 summarizes the main steps involved in both tattoo and laser alignment and SGRT alignment.

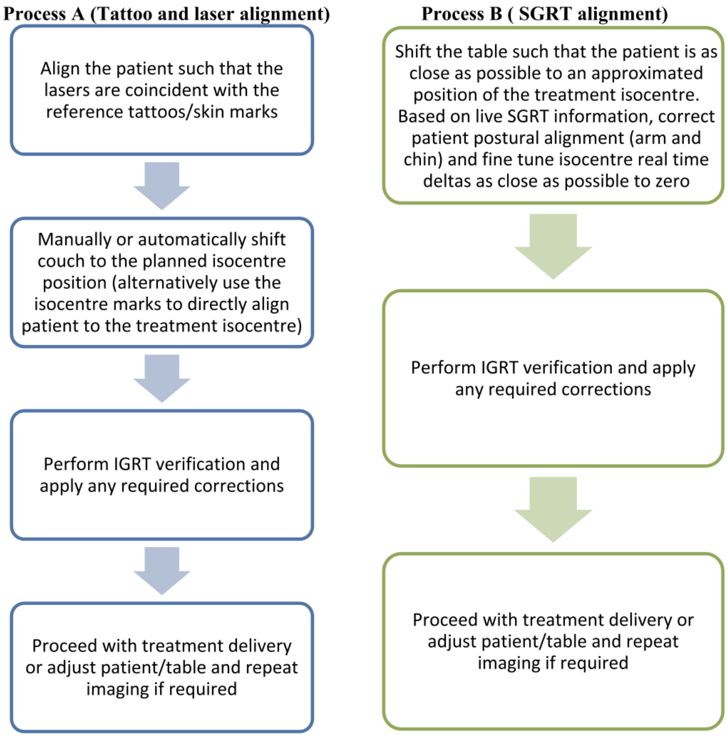

Figure 2.7: Flowcharts illustrating the workflow of a typical breast radiotherapy setup using conventional tattoos and lasers (Process A) compared to a surface-guided radiotherapy (SGRT) approach (Process B) [15].

- In traditional tattoo-based setups, the alignment of the patient is performed by positioning the skin tattoos at the intersection of the lasers in the treating room,

]

and then the patient is automatically shifted to the planned isocenter.
After this first alignment, a cone beam computed tomography (CBCT) is performed in order to check the accuracy of the setup before treatment.

- In SGRT the patient's surface is matched to the reference surface acquired during simulation, and it is possible to achieve an accurate positioning in six degrees of freedom (6DOF, three translational: lateral, longitudinal, vertical, and three rotational: pitch, roll, yaw axes), and perform postural corrections that are not possible with tattoos alone.
  Also in this case, after this first alignment, a cone beam computed tomography (CBCT) is performed in order to check the accuracy of the setup before treatment.

Even if some workflows still include tattoo and laser alignment as a further check, there is a clear evidence that the integration of SGRT can simplify the setup process and reduce the setup time. For example, in [32], over 38 breast cancer patients, the mean total setup time for initial positioning plus imaging was 314 s (5.2 minutes) with SGRT, versus 331 s (5.5 minutes) with skin marks and lasers, corresponding to a 5% reduction in time.

2.2.2 Catalyst® System and Patient Setup

The Catalyst® system, shown in Figure 2.8, is an optical surface scanner that enables high-precision patient positioning, intrafraction motion monitoring, and respiratory gating during radiotherapy treatments.

[A] *[B]*

Figure 2.8: [A] The Catalyst® main unit and [B] its integration in the treatment room [33].

As shown in Figure 2.8 [B], for an optimal coverage of the patient two additional units can be installed in an angle left and right from the main unit shown in Figure 2.8 [A].

The three main applications that can be performed with the Catalyst® system are:

- **cPosition:** measures the patient live surface, compares this with a reference surface and shows the correct patient position.
- **cMotion:** continuously compares the patient's current surface with the reference one and detects any motion during treatment, both at the isocenter and over the whole surface.
- **cRespiration:** tracks the breathing motion of a specific ROI for respiratory gated treatment.

The Catalyst® system is synchronized with the treatment couch and oncology information systems such as MOSAIQ® [34], allowing automatic patient recognition, live control of the couch position, and monitoring of the treatment beam [35].

Once the setup workflow is started, the Catalyst® system begins to scan the patient in real time and generates a live 3D surface which is compared to the reference surface acquired during the planning CT scan, and a non-rigid surface registration is performed to calculate the necessary couch shifts in six degrees of freedom (6DOF), as shown in Figure 2.9.

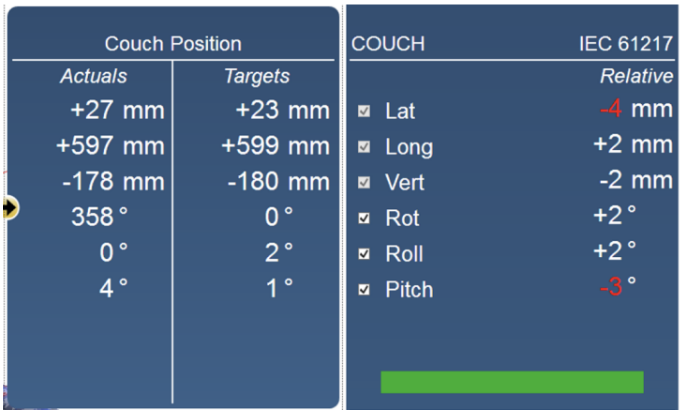

Couch Position

Actuals	Targets
+27 mm	+23 mm
+597 mm	+599 mm
-178 mm	-180 mm
358 °	0 °
0 °	2 °
4 °	1 °

COUCH	IEC 61217 Relative
☑ Lat	-4 mm
☑ Long	+2 mm
☑ Vert	-2 mm
☑ Rot	+2 °
☑ Roll	+2 °
☑ Pitch	-3 °

Figure 2.9: Example of the couch correction panel displayed by the Catalyst® software. On the left, the actual and target positions of the treatment couch, and on the right the relative deviations in all six degrees of freedom [33].

In order to proceed with treatment, the deviations from the reference position must be within 3 mm for translations and 3° for rotations.

The 3D view seen by the radiation technologists shows the real-time overlay of the patient's live surface with the planning reference surface; and misalignments are highlighted on the patient's surface using back-projection, as shown in Figure 2.10.

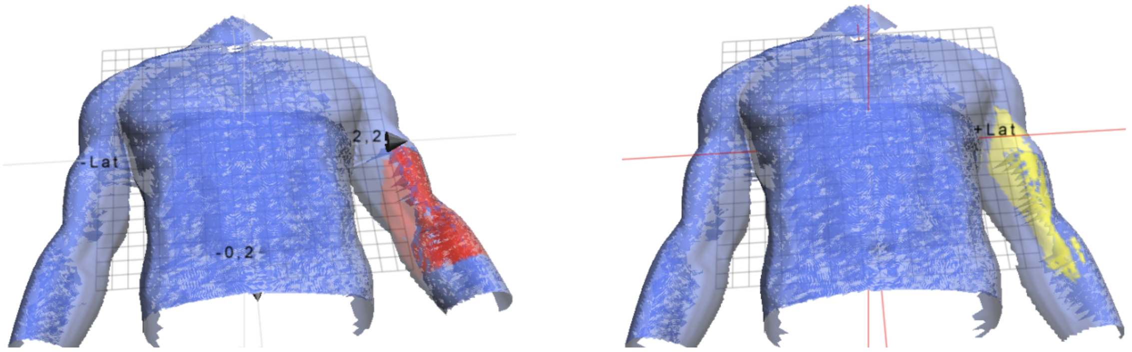

[A] *[B]*

Figure 2.10: Overlay of the live and reference surfaces during the initial patient setup.
[A] Red regions that should be lowered and [B] yellow regions that should be raised [33].

Red areas are regions that are too elevated and should be lowered, while yellow areas are regions that are too low and need to be raised.
This visual feedback allows the radiation technologist to correct the patient's posture manually.

Once the patient setup is complete and within the allowed tolerance, a cone beam computed tomography (CBCT) is performed in order to verify the internal anatomical alignment of the target before the treatment session.

2.2.3 Imaging Verification with Cone Beam Computed Tomography

Cone beam computed tomography (CBCT) is an imaging technique that has many differences from conventional computed tomography (CT).
First of all, the CBCT scanner uses a flat panel detector (FPD), which is a square 2D array of detectors, to capture a cone-beam of X-rays, while CT uses multirow detectors. Furthermore, the CBCT scanner uses a cone X-ray beam rather than a conventional linear fan beam to provide images, and as a result the CBCT provides a volume of data instead of a set of consecutive slices.
When reconstruction algorithms are applied to the volumetric CBCT data, a stack of 2D

grayscale images that represents the scanned anatomical region is generated, and the reconstructed dataset can be visualized in the sagittal, coronal, and axial plane.

The compact design and low radiation dose of CBCT systems make them suitable for imaging sensitive regions of the body, such as the breast. For this reason, CBCT is daily used in radiotherapy sessions to verify patient's position and anatomy before treatment delivery [36].

In DIBH treatments, the CBCT scan is performed while the patient holds the breath, guided in real time by the device showed in Figure 2.5 [A]. After the CBCT evaluation, additional couch translations and rotations can be applied in order to correct residual setup errors that may still be present despite the initial alignment performed with the Catalyst® system.

2.2.4 Treatment Delivery and Motion Monitoring

Once the final patient setup is completed and has been verified with the CBCT, the treatment delivery phase starts.

The Catalyst® system controls the LINAC's therapeutic beam, which, during DIBH treatments, is delivered only when the patient is in the correct breath hold level, as shown in Figure 2.11 [A].

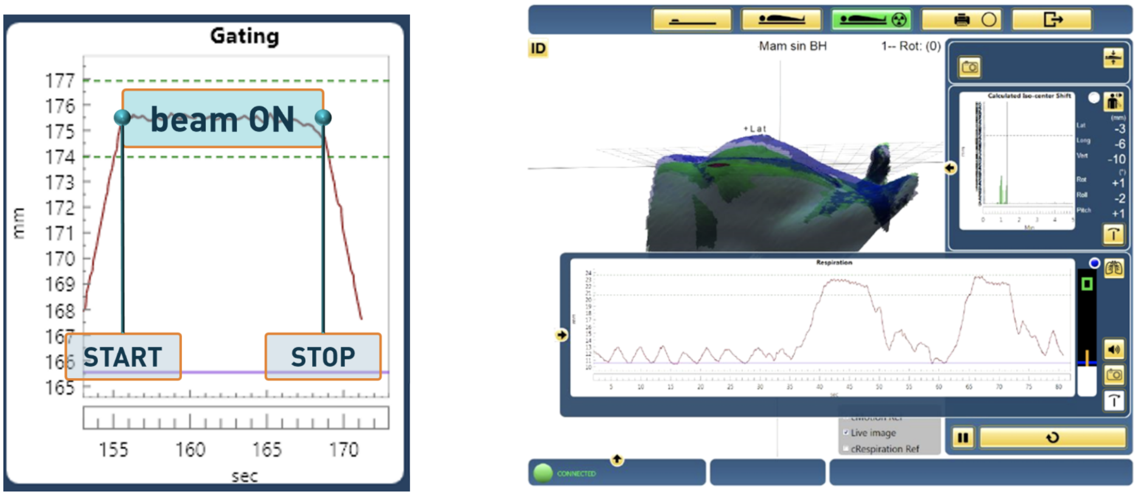

[A] [B]

Figure 2.11: [A] Example of the gating window logic and [B] Catalyst® system interface during DIBH treatment [33].

Thus, the Catalyst® system allows the synchronization of the radiation beam with the respiratory cycle of the patient.
The treatment procedure typically begins with an audio instruction performed by the radiation technologist that asks the patient to take a deep breath and hold it; and once the vertical elevation of the primary gating point is stable and falls within the predefined gating window, the treatment beam can be activated. The dose is typically delivered over successive breath holds of about 20 s each.

The Catalyst® interface, shown in Figure 2.11 [B], provides the visualization of the surface of the patient and its respiratory curve, which enables the radiation technologist to verify if the breath hold is stable and within the gating window during treatment.

At the end of the the first breath hold in which the dose has been delivered, the patient is instructed to breathe normally, and the beam is automatically stopped by Catalyst®.
Furthermore, as the system monitors continuously the breathing signal, if the patient exits the gating window before the agreed time, the beam is interrupted in order to prevent radiation delivery to incorrect anatomical regions.
After a brief recovery period, when the free breath of the patient has returned to the defined baseline, the breath-hold is repeated, and the treatment beam resumes dose delivery as soon as the breathing signal is entered in the gating window.
This cycle of breath hold and free breathing continues until the full dose for the session has been delivered. The process explained in subsection 2.2 is repeated daily for a total of 5 or 15 treatment sessions, depending on the clinical protocol, as explained in subsection 1.3.

This chapter explained the fundamental principles and clinical workflow of SGRT, and the integration of the Sentinel® and Catalyst® systems from planning to treatment delivery.
In the next chapter, a quantitative analysis of the geometric accuracy of the Sentinel® system will be presented, with the aim to assess its ability to reproduce the true anatomical elevation of the primary gating point during deep inspiration breath hold.

3 Geometric Measurements Reliability of the Sentinel® System

This chapter presents an analysis of the accuracy and consistency of the measurements provided by the Sentinel® system as used in clinical practice. All analyses were conducted retrospectively on a cohort of 35 breast cancer patients treated with DIBH, and their clinical DICOM data, including respiratory traces, CT scans, and radiotherapy structures, were used as input for a series of analyses performed in Python.

The analysis focus is on the stability of the primary gating point signal acquired by the Sentinel® system during the acquisition of the planning CT scan; in particular, what is validated is the vertical elevation of the primary gating point measured by the Sentinel® system against the surface elevation of the same point observed in CT scans.
Furthermore, a statistical comparison of these measurements was performed with previously published data.

3.1 Patient Dataset

All SGRT systems, including Catalyst® and Sentinel®, were installed at the Istituto Scientifico Romagnolo per lo Studio e la Cura dei Tumori (IRST) IRCCS "Dino Amadori" in Meldola in June 2024, this was when the institution began using SGRT for breast cancer treatments.
The dataset analyzed in this study consists of 35 female patients, all diagnosed with left-sided breast cancer and treated with DIBH technique at Istituto Scientifico Romagnolo per lo Studio e la Cura dei Tumori between October 2024 and May 2025.
The patients included in the study, labeled from patient 1 to patient 35, range in age from 34 to 77 years, in line with the common age distribution for early-stage breast cancer [37].
Regarding treatment protocols:

- 5 patients received hypofractionated radiotherapy with a total dose of 26 Gy delivered in 5 fractions.
- 30 patients were treated with a conventional regimen of 40 Gy in 15 fractions.

These patient data were used in order to perform an analysis of the accuracy and reliability of SGRT-based positioning.

3.2 Quantitative Evaluation of Sentinel® Primary Gating Point Elevation

To evaluate the accuracy of the Sentinel® primary gating point position, which is showed in Figure 2.4, the vertical elevation measured by tracking the primary gating point with the Sentinel® system (subsubsection 3.2.1), and the anatomical elevation occurring between the free breathing and breath hold conditions visualized on CT scans (subsubsection 3.2.2), were compared.
In this study, the elevation of the primary gating point is defined as the difference in elevation between the free breathing and deep inspiration breath hold respiratory conditions.

3.2.1 Primary Point Elevation Measurements with Sentinel® System

For the primary gating point elevation measured by the Sentinel® system, the difference between the average elevation during the breath hold phase, illustrated between the two red lines in Figure 3.1, and the baseline level, computed as the mean amplitude of the 100 data points (2 seconds) immediately preceding the start of the acquisition breath hold, highlighted in green in Figure 3.1 was calculated for all the patients of this cohort.

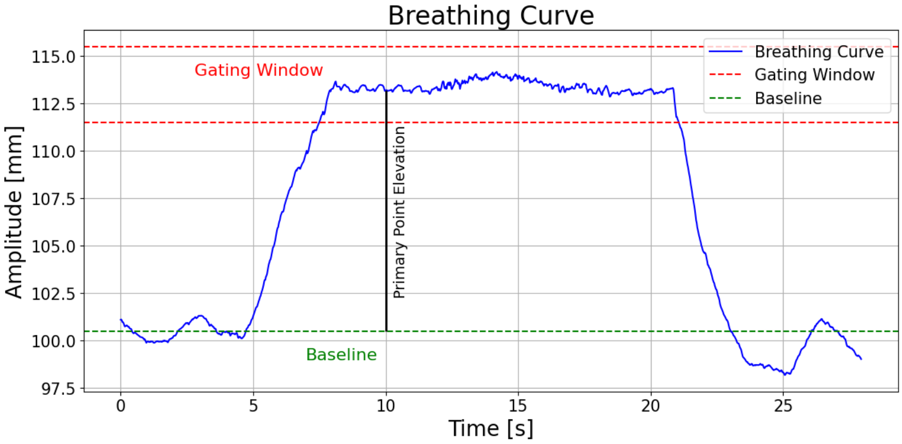

Figure 3.1: Example of a breathing curve acquired by the Sentinel® system. The primary point elevation corresponds to the difference between the breath hold amplitude and the baseline.

What is obtained, is the elevation of the primary gating point returned by the Sentinel® system, highlighted in black in Figure 3.1, and reported in Table A.1 as Sentinel® elevation.

3.2.2 Primary Point Elevation Measurements on CT Scans

For the primary gating point elevation measured on real CT scans, the mean distance between corresponding points sampled on two spheres with a diameter of 30 mm, positioned on the external contours of the CT scans acquired in free breath and breath hold, was computed in order to simulate the primary point positioned by the radiation technologist during the acquisition of the planning CT scan.

Figure 3.2 shows the elevation from the free breath phase (blue contour) to the breath hold phase (green contour), highlighting in red the difference between these two configurations, which is, in a first approximation, the primary gating point elevation measured on real CT scans.

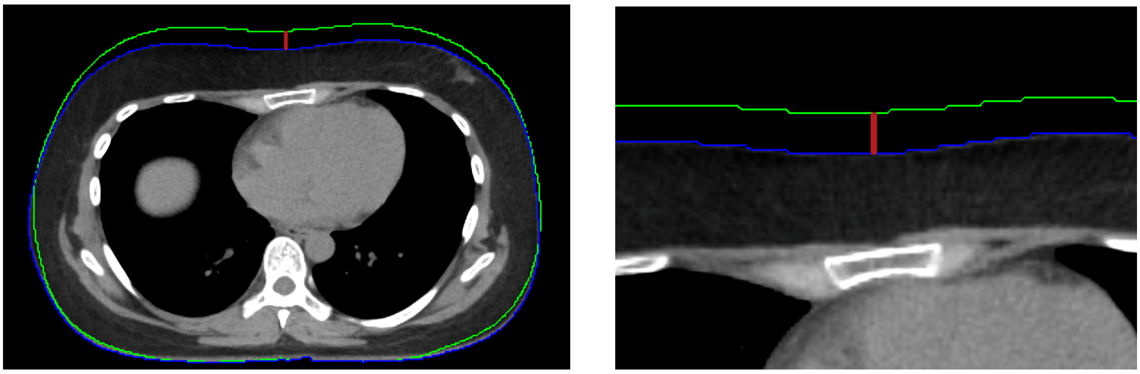

[A] *[B]*

Figure 3.2: Axial CT images showing the primary point elevation on a real patient: [A] full thoracic view and [B] zoomed-in view of the same region.

The comparison between the primary gating point elevation measured by the Sentinel® system, and the primary gating point elevation measured on real CT scans provides a measure of how accurately the Sentinel® system reproduce the true anatomical displacement between the free breathing and breath hold phases.

3.2.3 Procedure for the Primary Point Elevation Measurements on CT Scans

In order to enable the analysis of the vertical elevation between the free breathing (FB) and deep inspiration breath hold (BH) phases, two anatomical reference points and two anatomical reference surfaces were defined for each of the 35 patients using the MIM® software (MIM Software Inc., Cleveland, OH, USA [38]).

These points, labeled “Point FB” and “Point BH”, were manually placed on the external surface of the patient, in particular on the “Body FB” and “Body BH” contours, at a location corresponding to the xiphoid process. This anatomical point was chosen in order to simulate the position of the primary gating point marked by the radiation technologist during the acquisition of the planning CT scan. These points were first identified in the coronal plane and then projected onto the patient’s surface in the axial plane; this procedure was repeated for both the free breath and breath hold CT scans. The “Body FB” and “Body BH” structures represent the external surface of the patient as acquired in the free breathing and breath hold CT scans; these regions of interest were defined with the MIM® software using the “Whole Body” function available in the section “Contours”, which is based on a threshold algorithm that separates the body from the surrounding air.

At the end of this procedure, the complete set of data, including both ROIs and reference points of interest shown in Figure 3.3, was exported in DICOM RTSTRUCT format and used as input for a geometric analysis in Python.

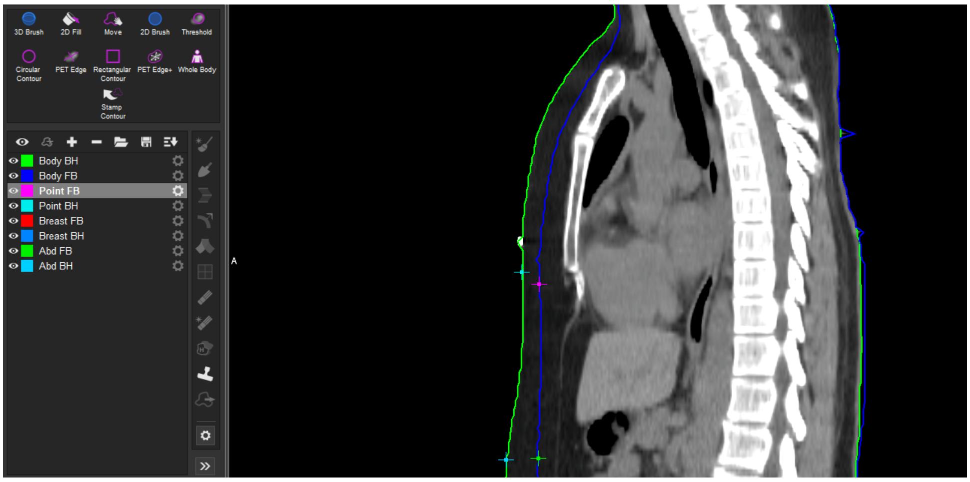

Figure 3.3: MIM® interface and visualization of points and ROIs of interest for patient 1.

3.2.4 Quantification of Surface Elevation

To obtain the estimation of the anatomical elevation of the primary gating point between the free breath and breath hold respiratory configurations, two spherical regions of interest were defined for each patient.

These spheres, with a diameter of 30 mm, were centered respectively on the manually defined “Point FB” and “Point BH”, and used as local sampling areas, in order to reproduce the primary gaiting point positioned by the radiation technologist during the acquisition of the planning CT scan, as shown in Figure 2.4.

A total of 30 equidistant points were placed along the equator of each sphere, lying in the axial plane. Each point was then projected on the patient’s surface by finding the closest vertex on the external mesh of the “Body FB” and “Body BH” contours, as shown in Figure 3.4 and Figure 3.5. Additionally, 15 points were sampled on a concentric sphere of 16 mm diameter, in order to evaluate internal consistency. A mesh is a three-dimensional surface representation made of a set of connected points called vertices. In this case, the mesh, derived from the segmentation of a region of interest, describes the outer contour of the patient’s body in both free breath and breath hold respiratory phases.

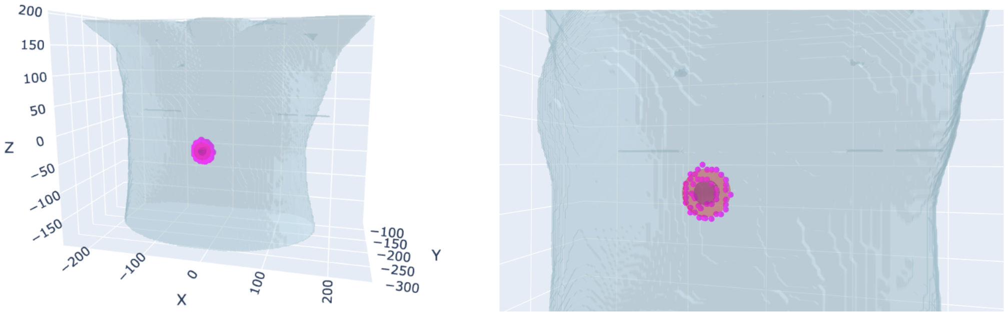

[A] [B]

Figure 3.4: Three-dimensional representation of the “Body FB” mesh with sampled points: [A] frontal view of the full torso and [B] close-up frontal view.

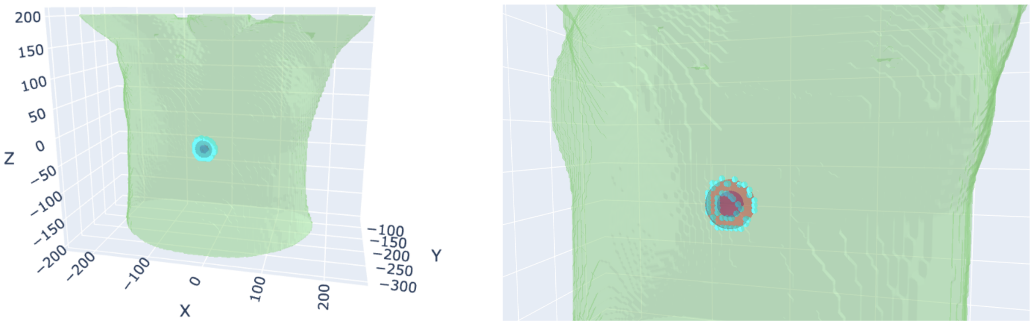

[A] [B]

Figure 3.5: Three-dimensional representation of the “Body BH” mesh with sampled points: [A] frontal view of the full torso and [B] close-up frontal view.

As a result, two sets of surface points were obtained for each breathing phase, and the Euclidean distance between each pair of corresponding points, showed in Figure 3.6 was calculated as:

$$d_i = \left\| \vec{P}_{\mathrm{BH},i} - \vec{P}_{\mathrm{FB},i} \right\|, \quad \text{for } i = 1, \ldots, 30 \tag{3.1}$$

for the 30 mm sphere, and

$$d_j = \left\| \vec{P}_{\mathrm{BH},j} - \vec{P}_{\mathrm{FB},j} \right\|, \quad \text{for } j = 1, \ldots, 15 \tag{3.2}$$

for the 16 mm sphere.

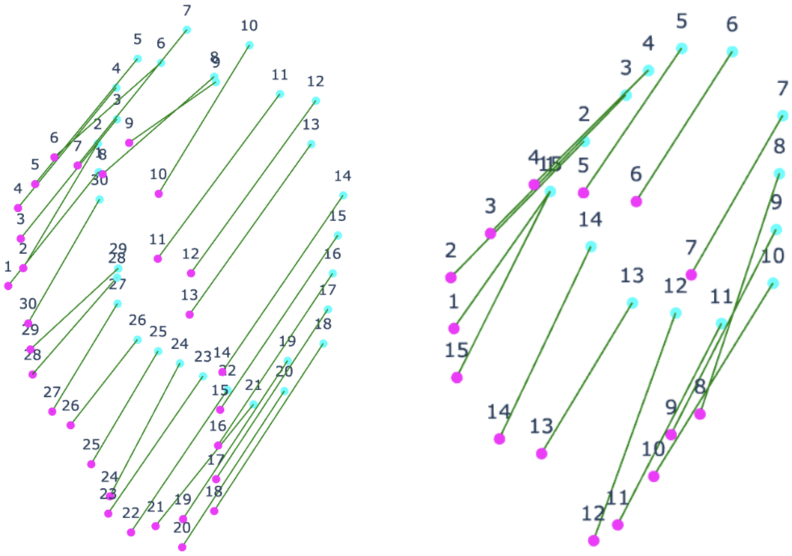

[A] [B]

Figure 3.6: Visualization of surface sampling on the [A] 30 mm sphere and [B] 16 mm sphere.

The mean distances $\overline{d}_{30}$ and $\overline{d}_{16}$ were then computed separately and used to estimate the anatomical displacement of the region of interest.

3.2.5 Vertical Projection and Normalized Comparison

In order to compare the elevation of the primary gating point measured from CT data with the vertical elevation calculated from the motion of the same point acquired by the Sentinel® system, a normalization procedure was required.

In fact, the distance computed using the spheres centered on “Point FB” and “Point BH” represents a three-dimensional anatomical elevation with components along all spatial directions (anterior-posterior, lateral, and cranio-caudal); however, the Sentinel® system records only the vertical elevation of the primary gating point along the z-axis.

To ensure that the two quantities described above could be compared, the spatial distance between the points was projected onto the vertical axis in order to isolate its z-component, as shown in Figure 3.7. This projected component, referred to as the normalized distance, was obtained using the following trigonometric relationship:

$$\text{Normalized distance} = d \cdot \sin(90^\circ - \theta) \tag{3.3}$$

where d is the mean Euclidean distance between the 30 pairs of corresponding surface points projected from the 30 mm spheres centered on “Point FB” and “Point BH”, while θ is the angle formed between the two points in the sagittal plane.

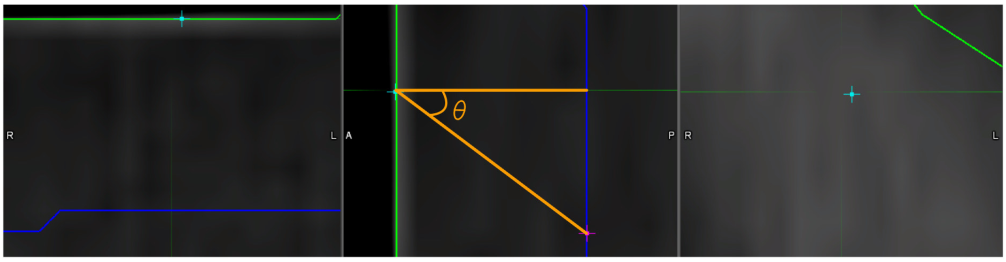

Figure 3.7: Visualization of the angle θ measured in the sagittal plane between Point FB and Point BH, used to compute the vertical component of the spatial displacement.

As shown in Figure 3.7, for each patient the angle θ was measured manually on the sagittal plane of the CT directly with the MIM® software, and reflects the deviation of the elevation vector from the vertical direction. This projection allows the comparison between the vertical elevation observed in CT scans and the elevation measured by tracking the primary gating window with the Sentinel® system.

3.2.6 Results

The elevations calculated using the two different methods are summarized in Table 3.1, while the full set of patient-specific displacement values is reported in Table A.1.
In this thesis, standard deviations were considered as errors associated with the mean, in order to ensure consistency with the methodology reported in the literature.

Measurement Type	**Mean [mm]**	**Standard Deviation [mm]**
CT elevation	13.2	4.0
Sentinel® elevation	12.8	3.5

Table 3.1: Mean and standard deviation of measured displacements.

The mean elevation of the primary gating point measured between the free breathing and breath hold CT scans using a 30 mm sphere was 16.8 mm, with a standard deviation of 6.4 mm. Identical values were obtained using the 16 mm sphere, indicating high consistency between the two spherical sampling regions; in fact, a Welch's t-test was performed to assess potential differences between these two measurements, and the obtained p-value was 0.9961, confirming the absence of a statistically significant difference. Given the similarity between these two measurements, the displacement values obtained from the 30 mm sphere were selected as representative for subsequent normalization, as they are based on a larger and more spatially robust sampling region.
After the projection of the 3D anatomical elevation on the vertical axis, a normalized elevation of the primary gating point of 13.2 ± 4.0 mm was obtained. This value closely matches the vertical elevation of the primary gating point measured directly from the Sentinel® system, which showed a mean of 12.8 mm and a standard deviation of 3.5 mm.

A scatter plot was generated to further evaluate the agreement between vertical elevations measured by the Sentinel® system and those estimated from the CT scans, as shown in Figure 3.8. Most points lie close to the identity line (y = x), and the linear regression (represented by the green line) confirms a strong agreement between the two measures.

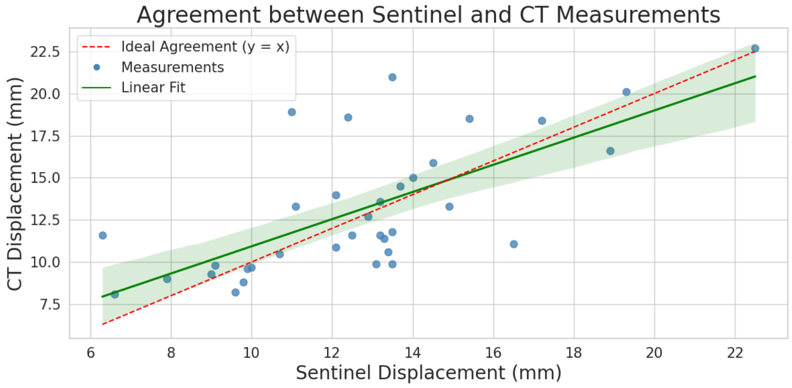

Figure 3.8: Scatter plot showing the agreement between vertical displacements measured by the Sentinel® system and those estimated from CT scans during DIBH.

Error bars and per–point weights are not shown nor used in the linear fits because the measurement uncertainty is approximately uniform across observations. The dominant sources of error are voxel discretization in point placement and small numerical inaccuracies from computing distances or integrals on the Cartesian plane. The same rationale applies to all regression plots reported in this study.

Furthermore, a Wilcoxon signed-rank test, appropriate for paired samples, indicated no statistically significant difference between the two measurement sets (p-value = 0.8398).

Figure 3.9 shows the individual vertical elevations measured by the Sentinel® system and from CT data for each patient. Blue and green dots represent the two respective values, while dashed lines connect paired measurements to illustrate the agreement.

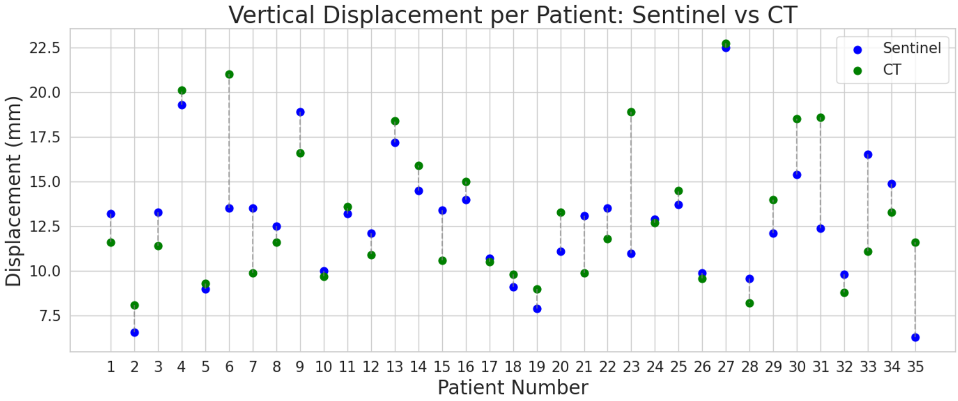

Figure 3.9: Scatter plot showing the correlation between vertical elevations measured by the Sentinel® system and those estimated from CT scans during DIBH.

A subset of patients, in particular patients 6, 23, 31, 33, and 35, showed a discrepancy greater than 5 mm between the two modalities. This threshold was selected based on common clinical tolerances for SGRT setups [39].

3.2.7 Discussion

As shown by Figure 3.8 and the Wilcoxon signed-rank test performed in subsection 3.2.6, the comparison between the elevations of the primary gating point measured by the Sentinel® system and those derived from CT scans during DIBH revealed a strong agreement, both visually and statistically.

These findings confirm that the Sentinel® system accurately reproduces the anatomical elevation occurring between the free breathing and breath hold phases, thus validating its reliability for vertical positioning during SGRT treatments.

Although the overall correlation showed by the Wilcoxon signed-rank test was strong, a moderate dispersion of some data points around the identity line, as shown in Figure 3.8, suggests the presence of inter-patient variability. This could be attributed to differences in patient anatomy or breathing patterns, and highlights the importance of an individualized investigation in SGRT workflows.
For example, one possible source of discrepancy can be the definition of the baseline level in the breathing curve registered from the tracking of the primary gating point by the Sentinel® system. Since the exact anatomical elevation corresponding to the free breathing CT acquisition is not known, the baseline was only estimated from the average signal during the 2 seconds preceding the breath hold. This approximation may introduce an uncertainty in the vertical reference level that affects the comparison with the displacement computed from CT scans.

Moreover, the deviations observed between the vertical elevation of the primary gating point measured by the Sentinel® system and from CT data for patients 6, 23, 31, 33, and 35, may be attributed to errors in the positioning of the primary gating point by the radiation technologist. In particular, if the primary gating point was placed far from the patient's xiphoid process, either too high, near the breast, or too low, toward the abdomen, it could result in an inaccurate estimation of the thoracic elevation occurring during DIBH; as a consequence, the agreement between the Sentinel® and CT measurements can be significantly compromised, leading to apparent discrepancies that do not reflect a true geometric mismatch.

3.3 Analysis of Respiratory Curves

Once it was established that the Sentinel® system accurately reproduces the elevation of the primary gating point between free breathing and breath hold phases, further analyses were performed.
In particular, according to [29], in order to assess the quality and stability of DIBH procedures, the vertical elevation of the primary gating point acquired with the Sentinel® system

was analyzed for each patient during the breath hold phase of the acquisition of the planning CT [40].
Using the procedure developed by [29], the vertical elevation of the primary gating point was fitted using a linear regression model, as shown in Figure 3.10:

$$y(t) = a \cdot t + b \tag{3.4}$$

where a represents the slope, indicative of a potential drift during the breath hold, while b is the intercept.

For each patient was also calculated the coefficient of determination R^2, which indicates how well the breath hold signal follows a linear trend. An R^2 close to 1 and a slope close to zero are indicative of a stable DIBH [29].

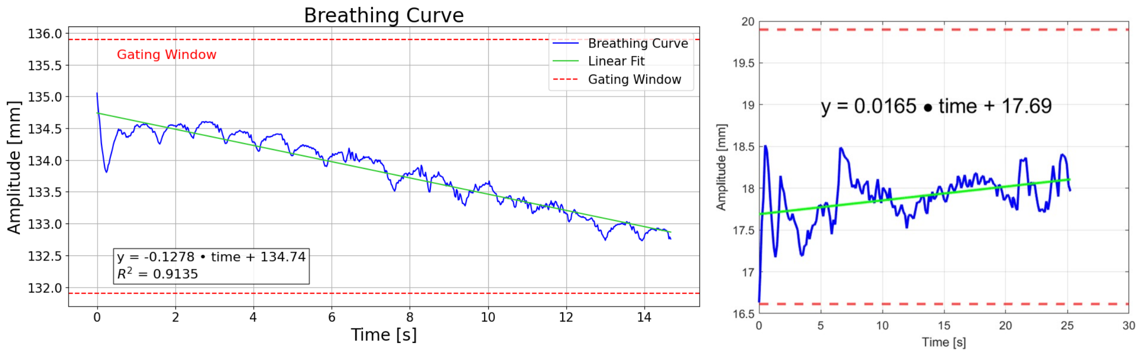

[A] *[B]*

Figure 3.10: Breathing curve [A] of patient 3 of this study and [B] from [29].

The mean results obtained for a, b and R^2 from all the 35 patients in this study are reported in Table 3.2, while, for completeness, the data obtained from the linear fit of the breathing curve of all the patients are reported in Table A.2.

	Minimum	**Maximum**	**Mean**	**Standard Deviation**
a	-0.21	0.09	-0.07	0.07
R^2	0.01	0.94	0.48	-

Table 3.2: Summary statistics (minimum, maximum, mean and standard deviation) for the linear fit parameter a and R^2.

- The slope a has a mean value of -0.07 ± 0.07, which indicates that a slight downward drift is on average observed during DIBH. This behavior may be attributed to the gradual downward movement of the couch during the acquisition of the planning CT, possibly due to the patient's weight, or to a tendency of the chest to fall, suggesting thoracic relaxation or a progressive loss of the breath hold.
- The coefficient of determination R^2 varies between 0.01 and 0.94, with a mean of 0.48, and reflects the variability in the quality of the breath hold among different patients.

3.3.1 Extraction of Heartbeats from the Respiratory Signal

From the raw vertical elevation of the primary gating point acquired by the Sentinel® system, and shown in Figure 3.11, small superimposed oscillations can be observed. These oscillations are not related to the breathing pattern but correspond to the patient's cardiac activity.

To isolate this component, the vertical elevation of the primary gating point was processed in order to estimate the heart rate of each patient during the acquisition of the planning CT, which was used as an indicator of patient agitation or stress during the procedure. A Python script was developed to perform this analysis.

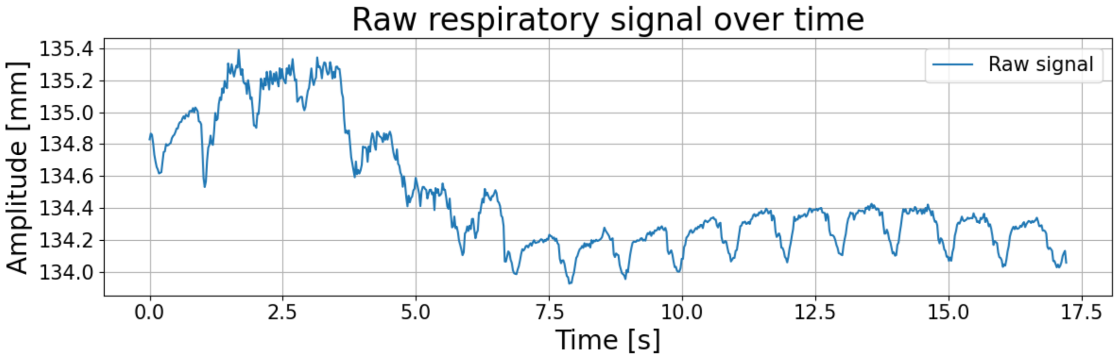

Figure 3.11: Raw respiratory signal over time for patient 24.

To better visualize the heartbeats embedded in the breathing curve, the data was smoothed using a Savitzky–Golay filter, as shown in Figure 3.12.

This filter works by fitting small portions of the signal with a polynomial curve, thus it reduces noise and preserves important features like peaks [41]. In this way, the cardiac

oscillations become more visible, and the estimation of the patient's heart rate during the breath hold phase becomes easier.
Compared with fitting a periodic function, this method avoids imposing strict periodicity on a signal that exhibits slow baseline drift and beat to beat variability.

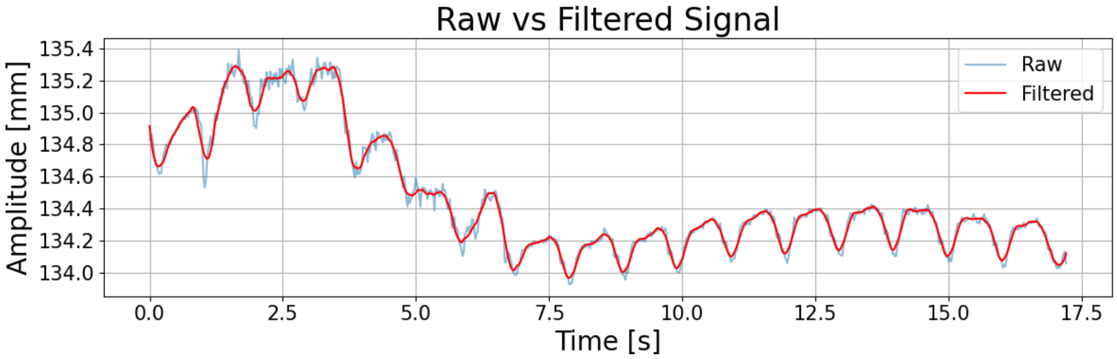

Figure 3.12: Comparison between the raw respiratory signal (blue) and the filtered signal (red) for patient 24.

To identify the patient's heartbeats from the filtered respiratory signal, local minima were detected as shown in Figure 3.13 on the basis of two criteria:

- A minimum distance of 20 samples between consecutive minima was required in order to avoid counting the same cardiac cycle more than once.
- A prominence threshold of 0.01 mm was applied to ensure that only significant deflections, thus associated with heartbeats, were detected.

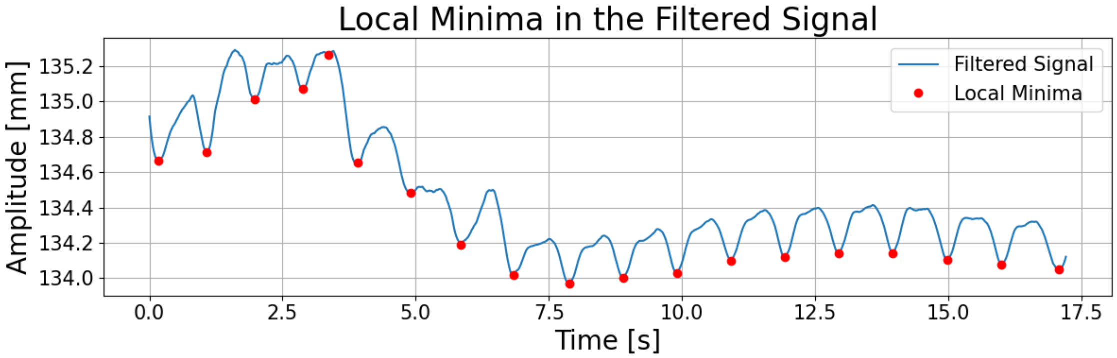

Figure 3.13: Detection of local minima (red dots) in the filtered respiratory signal (blue curve) for patient 24.

The minima identified from the filtered signal define a series of time points t_i, which represent the successive heartbeats [42].
The time intervals between adjacent beats, known as R-R intervals, are calculated as:

$$\text{intervals} = [t_2 - t_1,\ t_3 - t_2,\ t_4 - t_3,\ \ldots] \tag{3.5}$$

The average R-R interval is obtained as the arithmetic mean over all detected intervals:

$$\text{mean R-R interval} = \frac{1}{N}\sum_{i=1}^{N}(t_{i+1} - t_i) \tag{3.6}$$

The heart rate, expressed in beats per minute (bpm), is derived by taking the inverse of the mean R-R interval and multiplying by 60:

$$\text{Heart rate (bpm)} = \frac{60}{\text{mean R-R interval (in seconds)}} \tag{3.7}$$

As said above, the average heart rate during CT acquisition was calculated for all 35 patients based on the detected heartbeat oscillations in the vertical elevation of the primary gating point acquired by the Sentinel® system.
Table 3.3 summarizes the distribution of heart rate values, and reports the minimum, maximum, mean, and standard deviation observed across the cohort, while Table A.2 report the values of the estimated heart rate for each patient.

	Minimum	**Maximum**	**Mean**	**Standard Deviation**
Heart Rate [bpm]	46	108	72	12

Table 3.3: Summary of the heart rate calculated during CT acquisition for the 35 patients.

3.4 Correlation Analysis Between the Elevation of the Primary Gating Point and Anatomical Surrogates

Surface elevation was quantified at four different anatomical sites: the left nipple, the xiphoid process, the abdomen, and the region corresponding to the primary gating point used during the acquisition of the planning CT scan.

- For the breast elevation, the points placed on the left nipple, both in the free breath and breath hold configurations, as shown in Figure 3.14 [B] and Figure 3.14 [C], were used in order to compute the elevation as the Euclidean distance between these two points.

- For the xiphoid elevation, the points placed on the “Body FB” and “Body BH” contours at the level of the xiphoid process, showed in Figure 3.14 [A], were used in order to compute the elevation as the Euclidean distance between these two points.
- For the abdominal elevation, one point was placed on the “Body FB” contour and one on the “Body BH” contour on a location 10 to 20 cm inferior to the xiphoid process, as shown in Figure 3.14 [A]. The abdominal elevation was the computed as the Euclidean distance between these two points.
  For completeness, the results obtained for the breast, xiphoid, and abdominal elevations for all the patients of this cohort are reported in Table A.3.

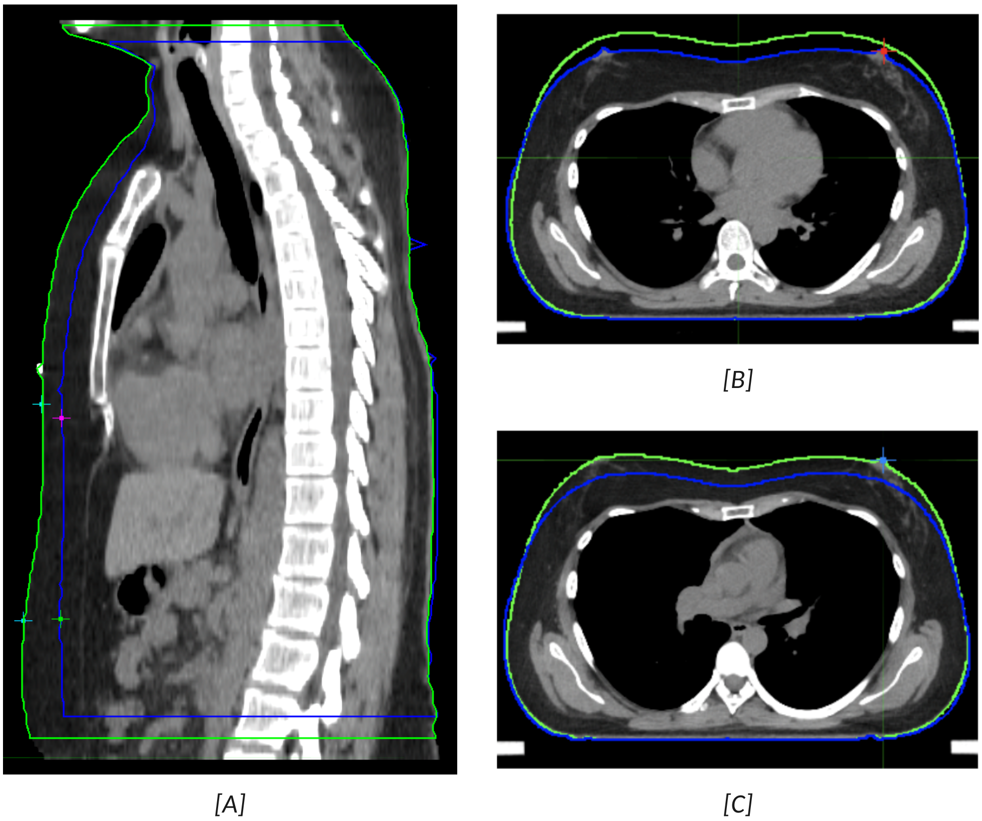

[B]

[A] [C]

Figure 3.14: [A] Coronal CT view of abdominal and xiphoid process points on both the free breathing (“Body FB”, blue contour) and breath hold (“Body BH”, green contour) surfaces.
$[B]$ Axial view of nipple point placed on the “Body FB” surface.
$[C]$ Axial view of nipple point placed on the “Body BH” surface.

- The vertical elevation of the primary gating point measured by the Sentinel® system, and labeled surrogate motion in [43], was calculated as previously discussed in subsection 3.2. This result is reported, for all 35 patient, in Table A.1 and labeled Sentinel® Elevation.

Patients were classified as thoracic breathers if the mean elevation of the thoracic region exceeded that of the abdominal region, while they were classified as abdominal breathers if the mean elevation of the thoracic region was smaller than the one of the abdominal region. Based on this criterion, 21 patients were classified as abdominal breathers, while the remaining 14 were classified as thoracic breathers, as shown in Table A.1.

Moreover, in order to investigate the consistency of motion across different anatomical regions during DIBH, a Pearson correlation analysis was performed between the elevations measured at three specific landmarks: the primary gating point (calculated as the Sentinel® elevation discussed in subsection 3.2), the nipple, and the abdomen.

For each pair of regions the Pearson correlation coefficient r and the corresponding p-value were calculated: the stronger the correlation, the more similarly the two regions move during DIBH. This analysis helps to understand if the movement of one area can be used to represent the movement of another, which is useful when selecting a reference point that is easy to reproduce during treatment.

3.4.1 Results

Table 3.4 summarizes the average values and standard deviations of the surface motion parameters evaluated in this study across all 35 patients.

	Mean [mm]	**Standard Deviation [mm]**
Breast Elevation	17.0	6.3
Xiphoid Elevation	17.8	6.7
Abdomen Elevation	19.2	6.8
Sentinel® elevation	12.8	3.5

Table 3.4: Summary of the average values and standard deviations of surface elevation measurements calculated across all patients.

The mean breast elevation was 17.0 ± 6.3 mm, the xiphoid elevation showed a slightly

higher mean value of 17.8 ± 6.7 mm, while the mean abdomen elevation was 19.2 ± 6.8 mm. The elevation of the primary gating point measured by the Sentinel® system was 12.8 ± 3.5 mm, as previously described in subsection 3.2
The detailed values for each individual patient are reported in Table A.3.

Furthermore, the Pearson correlation results are summarized in Table 3.5.

Comparison	**Pearson** r	p**-value**	**Interpretation**
Primary vs Nipple	0.71	< 0.0001	Significant
Primary vs Abdomen	0.35	0.0427	Significant
Nipple vs Abdomen	0.27	0.1153	Not significant

Table 3.5: Pearson correlation coefficients (r) and p-values for displacement pairs.

Strong correlations were observed between thoracic landmarks, particularly between the primary and nipple elevations ($r = 0.71$, p-value < 0.0001), and a weaker but statistically significant correlation was found between the primary and abdominal elevations ($r = 0.35$, p-value $= 0.0427$). However, no statistically significant correlation was observed between the nipple and abdominal elevations ($r = 0.27$, p-value $= 0.1153$), suggesting a lower consistency between thoracic and abdominal motion patterns during DIBH.

The scatter plots in Figure 3.15 illustrate the correlation between the displacement of the primary point and the two anatomical landmarks analyzed in subsection 3.4: the nipple [A] and the abdomen [B].

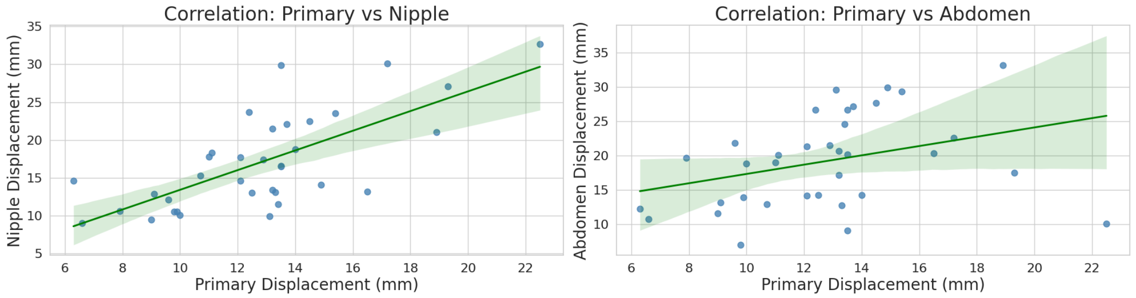

[A]

[B]

Figure 3.15: Correlation between the displacement of the primary point and three anatomical surrogates: [A] nipple, and [B] abdomen.

Panel [A] shows a strong linear correlation between the vertical elevation of the primary gating point and the elevation of the nipple, with a tight clustering of data points around the regression line; while panel [B], which represents the relationship between the vertical elevation of the primary gating point and the abdomen elevation, shows a weaker and more dispersed correlation.

3.4.2 Discussion

The surface displacement measurements obtained in this study were compared with values reported in recent literature. In [43] the cohort was made of 40 breast cancer patients treated with SGRT. The goal of this comparison was to understand if the anatomical displacements observed in our cohort are in line with previously published trends.

In [43], breast surface motion was quantified by placing a reference point at the isocenter of the treated breast, both in the free breathing and breath hold conditions. However, in our study, the treatment plan was only available for the breath hold CT scan, thus the position of the isocenter could not be identified for the free breathing phase.
For this reason, the surrogate chosen for breast elevation was the nipple, since it is a reproducible and visually accessible reference point.
Despite the different methodology, the values obtained are comparable; in fact, in [43] the majority of the reported displacements are between 6 mm and 22 mm, while in our cohort, nipple elevation ranged predominantly between 8 mm and 24 mm, as shown in Figure 3.16.

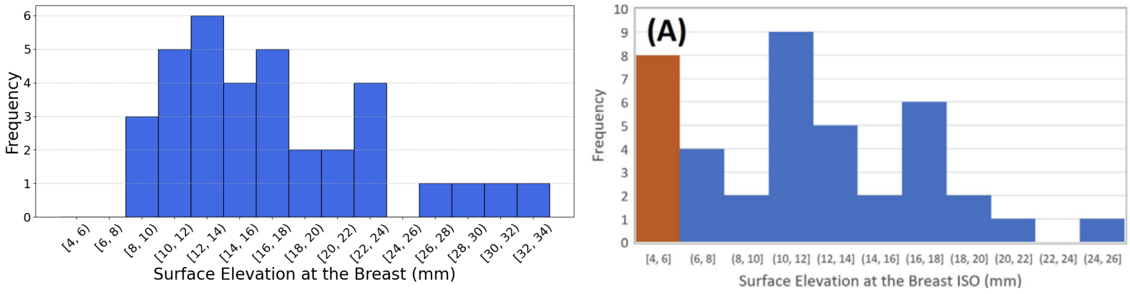

[A] *[B]*

Figure 3.16: Breast surface elevation during DIBH: [A] data from this study measured at the left nipple and [B] distribution from [43] at the breast isocenter.

In [43], the elevation at the xiphoid process during DIBH reports values that mostly range

between 4 mm and 18 mm. Although the exact method used to define this point is not specified, these values describe the motion in the lower thoracic area.
The values obtained in this study are in line with those found by [43]; in fact they mostly range between 10 mm and 24 mm, as shown in Figure 3.17.

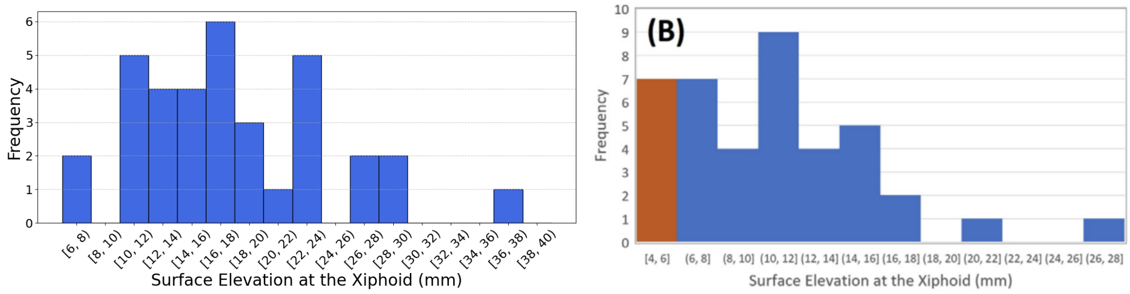

[A] *[B]*

Figure 3.17: Xiphoid surface elevation during DIBH: [A] data from this study and [B] distribution from [43].

Regarding the vertical elevation of the primary gating point derived from the Sentinel® system, the range of values observed in this cohort was narrower than the one reported in [43]. In particular, most patients in this study had a surrogate displacements between 8 mm and 20 mm, while a broader distributions that extends up to 26 mm was observed in [43], as shown in Figure 3.18. This difference may be due to variations in breath hold coaching protocols or differences in the gating strategy adopted during the CT acquisition phase; for example, in [43] the gating window had a width of 5 mm, while in this study it was only 4 mm.

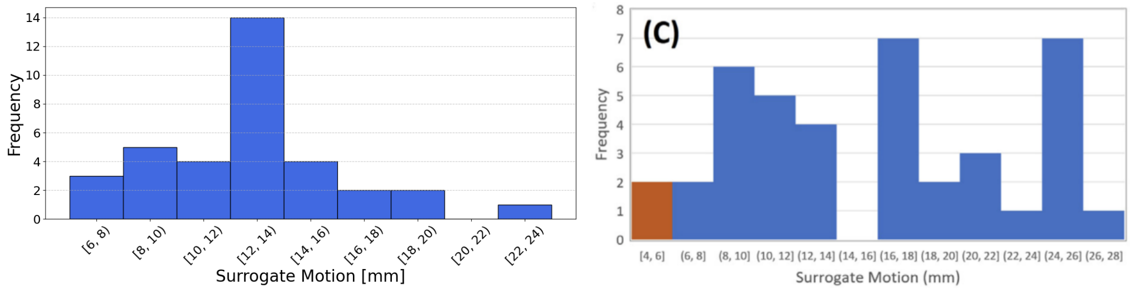

[A] *[B]*

Figure 3.18: Surrogate motion during DIBH: [A] data from this study and [B] distribution from [43].

To quantitatively compare the results obtained in this study with those reported in [43], a Welch's t-test was performed on the breast elevation and xiphoid elevation, while a Mann Witney U test was performed on the Sentinel® elevation, and the results are summarized in Table 3.6.

Parameter	**This Study** Mean ± SD [mm]	**[43]** Mean ± SD [mm]	***p*-value**
Breast Elevation	17.0 ± 6.3	11.6 ± 5.0	0.0001
Xiphoid Elevation	17.8 ± 6.7	10.6 ± 4.9	< 0.0001
Sentinel® Elevation	12.8 ± 3.5	15.9 ± 6.7	0.0744

Table 3.6: Comparison of elevation parameters between this study and [43].

For the Sentinel® elevation, the Mann–Whitney U test was performed since the raw data from [43] were fully available, allowing for a non-parametric comparison of the distributions, and this test did not show a statistically significant difference between the two groups. Anyway, these results highlight that it is important to consider patient-specific and demographic factors when comparing surface guided breath hold performance across different clinical centers.

One possible explanation for this finding may be the anatomical or physiological differences between populations; in fact, the patients in [43] were all Asian, which may be associated to a lower thoracic expansion capacity during deep inspiration breath hold.

For the Pearson correlations, the obtained results indicate that the nipple tend to move together with the primary gating point during breath hold, while abdominal motion shows weaker correlation or no correlation with thoracic structures, like the primary point and the nipple. This finding confirms that patients exhibit different breathing patterns; in fact, in our cohort 14 patients showed predominantly thoracic breathing, while 21 showed abdominal breathing.

Among the analyzed landmarks, the vertical elevation of the primary gating point showed a good correlation with both thoracic and abdominal elevation. This demonstrates that the primary gating point can be used as a reliable reference point for tracking the vertical elevation experienced by a patient during DIBH, regardless of it's breathing pattern.

However, due to patient anatomy or camera occlusions, if the primary gating point is not clearly visible on the Sentinel® interface when placed by the radiation technologists, it is sometimes shifted towards the abdomen. In such cases, the correlation with thoracic structures may weaken, and the tracking may no longer reflect the intended motion, as happens for patients 6, 23, 31, 33 and 35 of this study.
The scatter plots illustrated in Figure 3.15 are consistent with the previous observations reported in Table 3.5, where abdominal displacement exhibited a lower Pearson correlation coefficient with thoracic landmarks.

Overall, these results support the idea that thoracic landmarks tend to move in a similar way during DIBH and are generally more reliable for elevation tracking than abdominal landmarks.

4 Analysis of Residual Errors Post Cone Beam Computed Tomography

This chapter analyses the residual setup errors following surface-guided radiotherapy (SGRT) positioning, based on translational and rotational corrections applied after cone beam computed tomography (CBCT).
The first part presents quantitative metrics such as mean displacements, standard deviations, and 3D shifts, calculated across 35 patients in order to assess positioning accuracy. Both inter-patient and intra-patient variability are considered, with a comparison between patients receiving 15 fractions (30 patients) and those receiving 5 fractions (5 patients), in order to identify potential trends in setup consistency related to treatment schedule.

The second part of the chapter focuses on a geometric analysis of the breast surface. Using DICOM RTSTRUCT contours, a 3D mesh of the breast region is reconstructed, and through simulated rigid rotations, the positional variation of selected surface points is evaluated. This allows for the assessment of how rotational misalignments may amplify setup discrepancies in larger breast volumes.

4.1 Quantitative Analysis of Translational and Rotational Residual Errors

The translational and rotational corrections applied after the acquisition of the CBCT were extracted from the MOSAIQ® system [34].

This analysis focuses on the 35 patients introduced in subsection 3.1, and for each fraction, six degrees of freedom were recorded: vertical, longitudinal, and lateral translations (in mm), and pitch, roll, and yaw rotations (in degrees). In order to evaluate the effectiveness and consistency of the SGRT workflow, several parameters were calculated:

- the mean and standard deviation of each translational and rotational component for every patient, as reported in Table B.1 and Table B.2;
- the percentage of fractions exceeding clinical thresholds (5 mm for translations, 3°

for rotations [24]);

- the 3D shift for each fraction and the corresponding average per patient, reported in Table B.1.

In this context, a total of 475 fractions across 35 patients were analyzed.

All displacements reported on MOSAIQ® and in this study lie in a patient-based Cartesian reference system shown in Figure 4.1 and defined as follows:

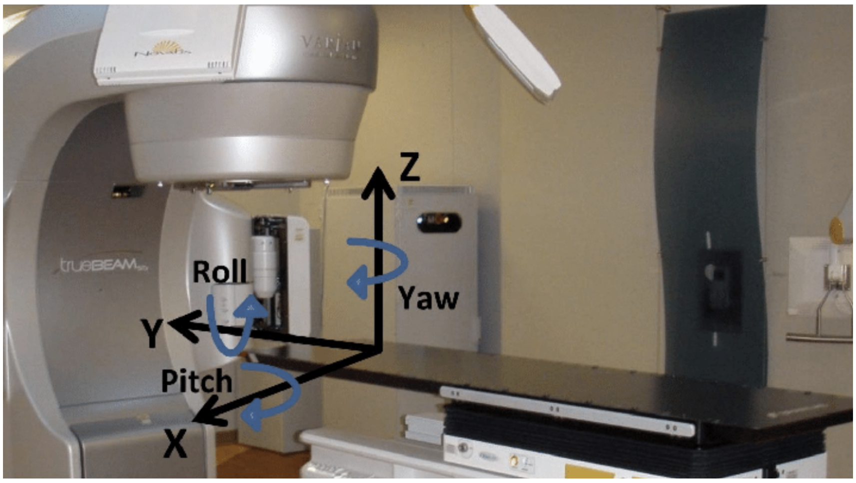

Figure 4.1: Patient-based coordinate system: lateral (X), vertical (Y), longitudinal (Z) axes, and the corresponding rotational axes (pitch, roll, yaw) [44].

Translational displacements (in mm):

- **X** (LAT): lateral axis, where positive values indicate a shift toward the patient's left side.
- **Y** (LNG): longitudinal axis, with positive values indicating a shift toward the patient's head.
- **Z** (VRT): vertical axis, with positive values indicating a displacement upward, away from the couch.

Rotational displacements (in degrees):

- **Pitch** (rotation around X): corresponds to a chin-up or chin-down movement. Positive pitch indicates the patient's chin rotating upward.

- **Roll** (rotation around Y): indicates a lateral tilt of the torso. Positive values represent a clockwise rotation when viewed from the patient's feet.
- **Yaw** (rotation around Z): axial rotation around the vertical axis. A positive yaw corresponds to the patient turning toward their left.

It is important to note that rotational corrections greater than 3° are generally not physically applied during treatment. This limitation is due to the fact that the treatment couch is not designed to safely accommodate large angular displacements, as excessive pitch, roll, or yaw could result in patient discomfort or the sensation of falling.
Furthermore, all rotational corrections are performed with respect to the isocenter defined by the medical physicists in the treatment planning system.

For each patient who received 15 fractions of radiotherapy, the data were structured as shown in Table 4.1, to enable the computation of intra-patient statistical measures.

Fraction	X [mm]	Y [mm]	Z [mm]	X [°]	Y [°]	Z [°]
1	3	-2	1	-2.2	1.0	1.0
2	1	3	8	-0.6	1.6	0.8
3	1	1	2	-0.1	-0.3	-0.1
4	-5	3	0	-0.3	0.1	2.6
5	0	2	-4	-0.6	0.6	2.4
6	-1	0	0	-1.3	1.1	0.7
7	0	1	1	-0.2	-0.1	1.2
8	0	2	-2	-2.3	0.0	1.1
9	-4	2	1	-0.8	1.9	1.2
10	1	1	0	-0.4	1.1	0.5
11	-1	3	4	0.8	1.2	0.6
12	-3	1	0	-1.6	0.0	1.0
13	-2	1	1	0.9	0.9	1.4
14	2	0	0	0.0	1.2	1.3
15	-2	3	1	0.7	1.2	0.6

Table 4.1: Translational and rotational displacements recorded for patient 1 of this study across 15 treatment fractions.

The same procedure was also computed for each patient that received 5 fractions of radiotherapy, as shown in Table 4.2.

Fraction	**X [mm]**	**Y [mm]**	**Z [mm]**	**X [°]**	**Y [°]**	**Z [°]**
1	-4	-3	1	-1.4	-0.6	1.8
2	0	-5	0	1.0	-0.9	1.6
3	-3	-3	2	-0.9	-0.2	0.5
4	-4	-6	1	0.0	-0.2	0.6
5	-1	-3	2	-1.0	-1.5	1.5

Table 4.2: Translational and rotational displacements recorded for patient 8 of this study across 5 fractions.

In addition to the calculation of mean and standard deviation for each translational and rotational axis, the 3D displacement magnitude (or total setup error) was computed for each treatment fraction. Moreover, for every patient, the average 3D shift across all fractions was then calculated to provide a single summary value representative of their residual positioning errors.

The 3D shift for each fraction was computed using the Euclidean norm of the translational components:

$$\text{3D shift} = \sqrt{x^2 + y^2 + z^2} \tag{4.1}$$

This metric captures only translational displacement. Rotations produce point dependent shifts about the isocenter and their geometric effect is quantified in subsection 4.2.

The systematic error Σ was defined as the standard deviation of the patient-specific mean displacements across the population, while the random error σ was computed for each translational and rotational axis as the mean of the intra-patient standard deviations across all patients, providing a single value per axis representative of the overall random variability [15]. These values quantify the fraction-to-fraction variability and were used to assess the overall consistency of the SGRT setup.

These metrics help to assess how accurate and reliable the SGRT setup was across the entire cohort. The 3D shift indicates how far the patient's position deviated from the planned one at each fraction, while the random and systematic errors reveal whether such deviations were occasional or consistently repeated. Taken together, they allow an evaluation of the precision and reproducibility of SGRT through the treatment course.

As an example, the results for all the explained quantities for patient 1 and patient 8 of this study are reported in Table 4.3.

Parameter	**Patient 1**	**Patient 8**
Mean ± SD – X (Lateral) [mm]	−0.7 ± 2.2	−2.4 ± 1.8
Mean ± SD – Y (Longitudinal) [mm]	1.4 ±1.4	−4.0 ± 1.4
Mean ± SD – Z (Vertical) [mm]	0.9 ± 2.6	1.2 ± 0.8
Mean ± SD – Pitch [°]	−0.6 ± 0.9	−0.5 ± 1.0
Mean ± SD – Roll [°]	0.8 ± 0.7	−0.7 ± 0.5
Mean ± SD – Yaw [°]	1.1 ± 0.7	1.2 ± 0.6
3D shift (mean ± SD) [mm]	3.5 ± 2.0	5.2 ± 1.3

Table 4.3: Patient-specific summary of residual setup errors for two representative patients: patient 1 (15 fractions) and patient 8 (5 fractions).

4.1.1 Results

The results obtained among all the 30 patients of this study treated with 15 fractions of radiotherapy are reported in Table 4.4.

Parameter	**X – Lateral**	**Y – Longitudinal**	**Z – Vertical**
Translational displacements [mm]			
Mean ± SD	0.4 ± 3.2	0.4 ± 4.7	1.9 ± 4.0
Systematic error Σ	2.6	3.9	3.3
Random error σ	2.0	2.5	2.3
% fractions $> \pm 5mm$	8%	23%	19%
3D shift [mm]	6.3 ± 3.6		
% fractions with 3D shift $> 5mm$	56%		
Rotational displacements [°]			
Mean ± SD	−1.1 ± 1.2	−0.6 ± 1.1	0.1 ± 1.4
Systematic error Σ	0.8	0.8	0.9
Random error σ	0.8	0.8	1.1

Table 4.4: Summary of residual translational and rotational setup errors for the 30 patients treated with 15 fractions each (450 total fractions).

While the results obtained among all the 5 patients of this study treated with 5 fractions of radiotherapy are reported in Table 4.5.

Parameter	**X – Lateral**	**Y – Longitudinal**	**Z – Vertical**
Translational displacements [mm]			
Mean ± SD	−0.1 ± 2.4	−0.4 ± 5.2	2.9 ± 5.0
Systematic error Σ	2.3	4.7	4.5
Random error σ	1.3	3.0	2.8
% fractions $> \pm 5mm$	8%	23%	19%
3D shift [mm]	6.5 ± 4.9		
% fractions with 3D shift $> 5mm$	48%		
Rotational displacements [°]			
Mean ± SD	−0.7 ± 1.0	−0.1 ± 1.2	0.5 ± 1.3
Systematic error Σ	0.8	1.0	1.0
Random error σ	0.8	0.8	1.0

Table 4.5: Summary of residual translational and rotational setup errors for the 5 patients treated with 5 fractions each (25 total fractions).

A comparison between the two treatment groups shows that patients undergoing hypofractionated schedules (5 fractions) exhibited slightly larger translational displacements, particularly along the vertical axis (mean 2.9 ± 5.0 mm vs 1.9 ± 4.0 mm) and in terms of overall 3D shift (6.5 ± 4.9 mm vs 6.3 ± 3.6 mm).

Moreover, the 5-fraction group showed higher systematic and random errors along the lateral and vertical directions, and a slightly higer rotational deviations in yaw (0.5° vs 0.1°). However, the percentage of fractions exceeding clinical thresholds remained comparable between the two groups. It should be noted that, due to the substantial difference in sample size between the two groups (450 vs 25 fractions), no statistically significant comparison can be established.

As shown in Figure 4.2, a boxplot of residual translational displacements along the three anatomical axes was generated.

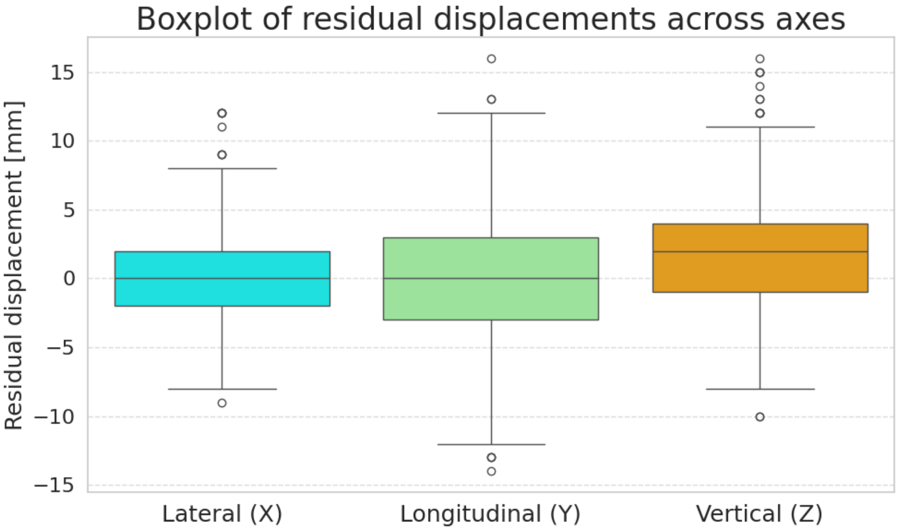

Figure 4.2: Boxplot of residual translational displacements across the three anatomical axes (Lateral – X, Longitudinal – Y, Vertical – Z).

- The lateral (X) direction shows a relatively symmetric distribution centered near zero, with fewer extreme outliers.
- The longitudinal (Y) axis exhibits the largest spread, with a wider interquartile range and more extreme deviations, including displacements beyond ±10 mm.
- The vertical (Z) axis shows a clear positive skew, with most displacements being upward, consistent with the positive mean observed in Table 4.4 and Table 4.5.

To further characterize the behavior of residual setup errors after CBCT-based correction [45], histograms of translational displacements were plotted along the three main anatomical directions (lateral, longitudinal, and vertical) across the full dataset of 475 fractions. A Gaussian fit was applied to each distribution to extract the mean value μ and standard deviation σ, as shown in Figure 4.3, Figure 4.4, and Figure 4.5.

In the lateral direction (X-axis), for which the histogram is reported in Figure 4.3, the distribution is relatively symmetric, in fact, it is centered around $\mu = 0.4$ mm, with a standard deviation SD $= 3.2$ mm, and approximately 8% of the treatmjent fractions exceded ±5 mm.

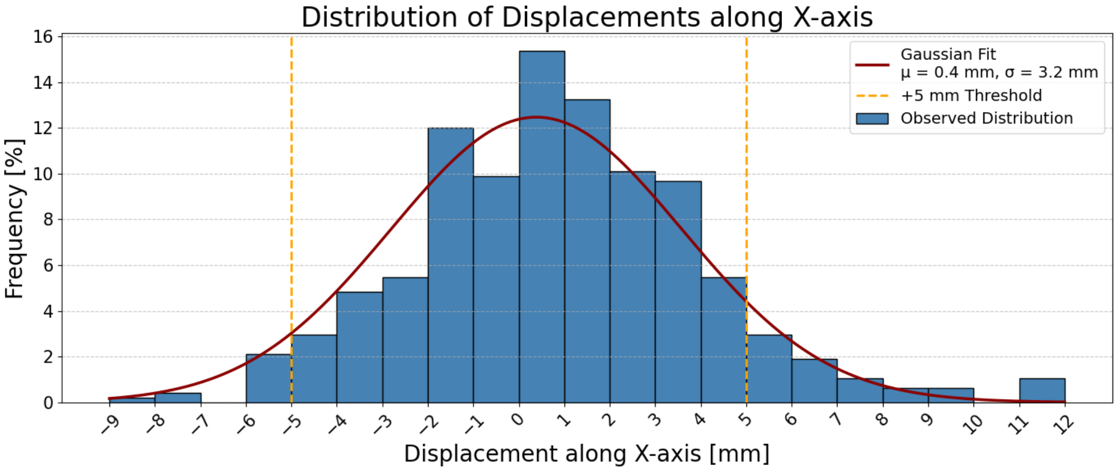

Figure 4.3: Distribution of translational displacements along the lateral (X) axis across all 475 fractions.

The longitudinal direction (Y-axis), as illustrated in Figure 4.4, shows greater variability; in fact, the mean value is $\mu = 0.5$ mm, but the standard deviation is higher (SD = 4.7 mm). Approximately 23% of the fractions exceed ±5 mm, indicating that lateral alignment is the most critical direction in this cohort.

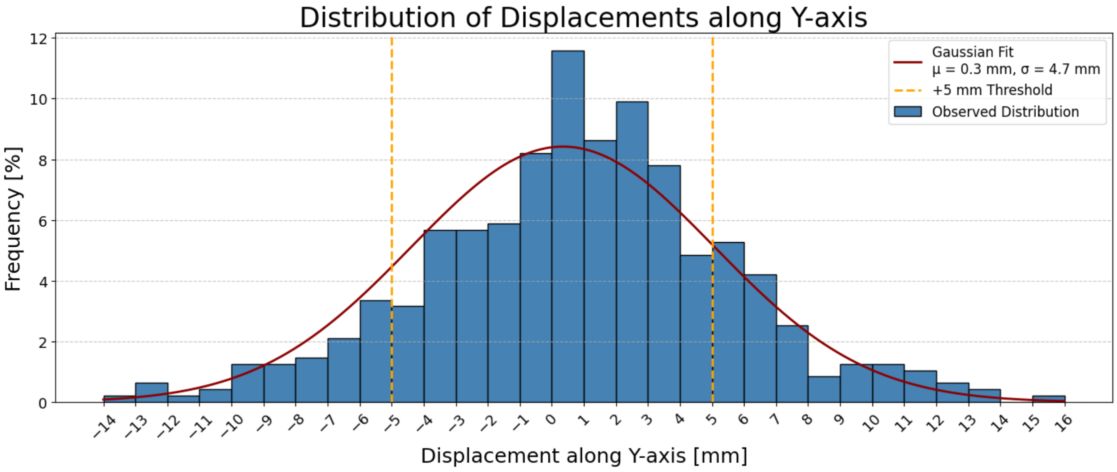

Figure 4.4: Distribution of translational displacements along the longitudinal (Y) axis across all 475 fractions.

In the vertical direction (Z-axis), for which the histogram is reported in Figure 4.5, the distribution is centered around $\mu = 1.9$ mm with a standard deviation SD = 4.1 mm. This positive mean suggests that vertical displacements often required correction upward. The proportion of fractions exceeding ±5 mm was 19%; thus the vertical axis is a secondary but still relevant source of misalignment.

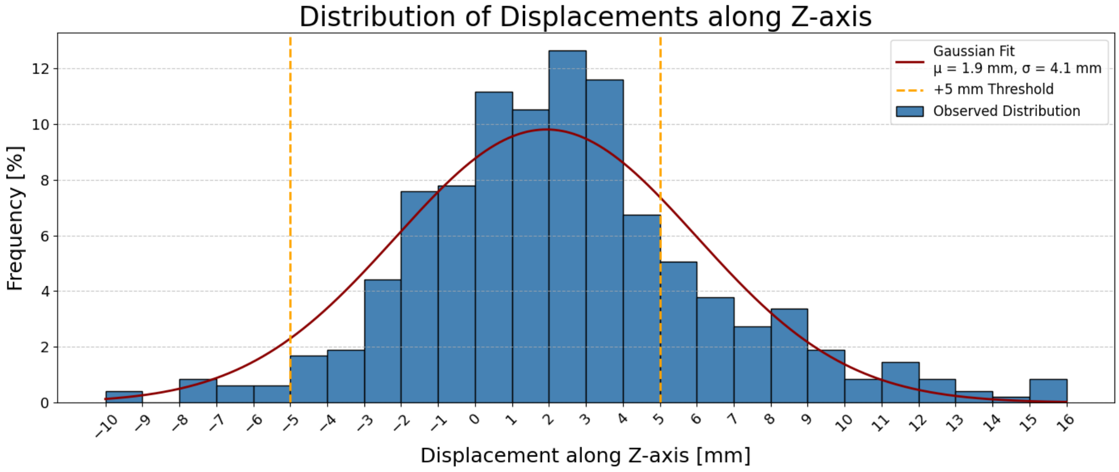

Figure 4.5: Distribution of translational displacements along the vertical (Z) axis across all 475 fractions.

However, in all three directions, the histograms approximate a bell-shaped distribution centered near the origin, suggesting that the SGRT initial alignment was generally effective in minimizing systematic setup errors.

4.1.2 Discussion

In comparison to conventional alignment methods that rely on skin tattoos and room lasers, SGRT has demonstrated superior accuracy [15] [46] and faster patient alignment [47] in multiple studies, especially in breast cancer treatments where external anatomy is directly observable.

To evaluate the consistency of the results of this study with previously published data, the residual translational and rotational errors observed in this cohort were statistically compared to those reported in [48]. In particular, the mean and standard deviation of setup errors along each anatomical axis were extracted from [48], which analyzed 245 fractions of radiotherapy collected from 49 breast cancer patients treated with SGRT. Since raw data from [48] were not available, a Welch's t-test was employed to compare the means and standard deviations of [48] with the ones of the 15 fraction group of this study, and the results are summarized in Table 4.6.

Direction	**This study**	**[48]**	***T*-statistic**	***p*-value**
Translational errors [mm]				
Lateral (X)	0.4 ± 3.2	0.9 ± 2.7	−2.2	0.0295
Longitudinal (Y)	0.4 ± 4.7	1.6 ± 3.1	−4.0	0.0001
Vertical (Z)	1.9 ± 4.0	1.2 ± 2.6	2.8	0.0055
Rotational errors [°]				
Pitch	−1.1 ± 1.2	0.3 ± 0.9	−17.4	< 0.0001
Roll	−0.6 ± 1.1	0.3 ± 1.0	−10.9	< 0.0001
Yaw	0.1 ± 1.4	0.0 ± 0.8	1.2	0.2313

Table 4.6: Comparison of residual setup errors between this study (450 fractions) and [48] (245 fractions), using Welch's t-test.

In order to evaluate the agreement between this study and previously published data, the systematic (Σ) and random (σ) setup errors were analyzed with respect to the values reported in [48]. An F-test was applied, and the results are summarized in Table 4.7.

Direction	**Error Type**	**This Study**	**[48]**	***F*-value**	***p*-value**
Translational errors [mm]					
Lateral (X)	Systematic (Σ) [mm]	2.6	1.7	2.3	0.0089
	Random (σ) [mm]	2.0	1.3	2.4	0.0080
Longitudinal (Y)	Systematic (Σ) [mm]	3.9	1.9	4.2	< 0.0001
	Random (σ) [mm]	2.5	1.7	2.2	0.0174
Vertical (Z)	Systematic (Σ) [mm]	3.3	1.6	4.3	< 0.0001
	Random (σ) [mm]	2.3	2.0	1.3	0.3840
Rotational errors [°]					
Pitch	Systematic (Σ) [°]	0.8	0.8	1.0	0.9781
	Random (σ) [°]	0.8	0.6	1.8	0.0758
Roll	Systematic (Σ) [°]	0.8	0.6	1.8	0.0758
	Random (σ) [°]	0.8	0.8	1.0	0.9781
Yaw	Systematic (Σ) [°]	0.9	0.5	3.2	0.0003
	Random (σ) [°]	1.1	0.7	2.5	0.0054

Table 4.7: Comparison of systematic and random setup errors between this study (30 patients) and [48] (49 patients), using F-test.

It should be noted that, as expected, the standard deviations observed in this study are higher than the mean residual shifts because displacements can be either positive or negative and tend to cancel each other out when averaged, while their variability remains.

The values of residual setup errors and their variability observed in this study show both similarities and differences when compared to the results published in [48]. Statistically significant differences emerged in particular for the longitudinal and vertical directions, and for the rotational components of pitch and roll; similarly, significant differences were also observed in systematic and random errors, particularly in the longitudinal and vertical directions, and in the yaw rotation.
In the interpretation of these differences, several methodological factors must be considered: first of all, in [48] the analyzed data come from patients treated in free breathing, while this study includes only patients treated in DIBH, and an increased variability in setup accuracy under breath-hold conditions is expected. Secondly, patient selection criteria are not clearly defined in [48], which may suggest a filtered cohort. In contrast, the data analyzed in this study include all patients treated with SGRT for left-sided breast cancer between October 2024 and May 2025, without any form of selection.
Despite these differences, the overall performance of SGRT remains within clinically acceptable limits; thus, the reliability of this system is confirmed even in the context of DIBH within a real clinical workflow.

Finally, the findings observed along the vertical (Z) axis are consistent with those previously discussed in section 3, where the geometric accuracy of the Sentinel® system was evaluated. In that analysis, it was shown that the Sentinel® system tends to slightly underestimate the true vertical displacement of the chest wall, as confirmed by the discrepancy between the surface tracking system and the distance estimated from the CT between the two breathing configurations. This underestimation contributes to the residual positive displacement observed post-CBCT along the Z direction.

4.2 Geometric Impact of Rotational Errors

Although SGRT has been widely validated for translational accuracy, its performance regarding rotational errors has been less explored. In fact, only a limited number of studies, such as [49], have investigated the clinical relevance of residual rotations, or have quantified their geometric implications. Despite this, the overall impact of uncorrected rotations is often underestimated in clinical practice, mainly because angular deviations below 3° are commonly accepted and not corrected due to couch limitations.

Thus, this part of the chapter aims to provide an evaluation of the geometric distortions introduced by small but potentially meaningful rotational errors, especially when dealing with large or irregular breast volumes. To further investigate the implications of rotational corrections, a Python script was developed in order to simulate the geometric effect of angular displacements on the breast. The aim of this analysis was to assess how much a controlled rotation around the isocenter of the treatment could alter the geometry of the patient's surface, especially in regions located far from the rotation origin.

The first step of this analysis consisted in the extraction of the "Breast" ROI contours, manually delineated by the radiation oncologists, and the isocenter of treatment point, defined by the medical physicists, in DICOM RTSTRUCT format, using the MIM® software, as shown in Figure 4.6. Moreover, the software MIM® also allowed the extraction of the volume data for the "Breast" ROI for each patient. These values were collected across the entire cohort and are reported in Table B.2.

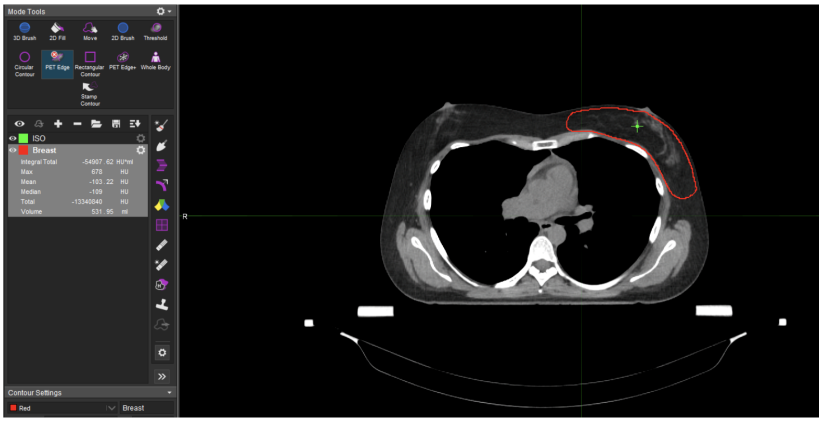

ISO
Breast

```
Integral Total   -54907.62  HU*ml
Max                    678  HU
Mean               -103.22  HU
Median                -109  HU
Total            -13340840  HU
Volume              531.95  ml
```

Figure 4.6: Axial CT slice visualized in MIM® showing the "Breast" ROI (in red) and the isocenter point (green cross).

After exporting the "Breast" contour, a 3D surface mesh of the breast was reconstructed using a convex hull algorithm, a method that encloses the outermost points of a structure to generate a closed and continuous surface, as shown in Figure 4.7 [A]. Moreover, among all surface points, the one located farthest from the isocenter was automatically identified, as it is the most sensitive to angular displacements, as shown in Figure 4.7 [B].

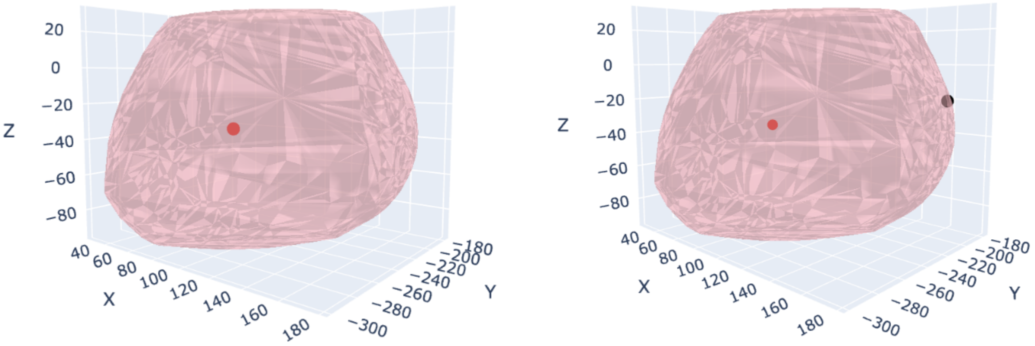

[A] [B]

Figure 4.7: 3D reconstruction of the breast mesh of patient 21 highlighting [A] the isocenter (red) and [B] the farthest point from the isocenter (black).

Before the application of the simulated rotations, the reference system was translated so that it's origin coincided with the isocenter defined in the RTSTRUCT file.

The position of the point farthest from the isocenter (black point in Figure 4.7 [B]) was then tracked before and after rotation around the three anatomical axes: pitch (X), roll (Y), and yaw (Z). The resulting 3D shift, calculated as the Euclidean distance between the pre-rotation and post-rotation positions of the black point, was used in order to estimate the maximum deviation induced by rotational misalignment.

Finally, the coordinate displacements (ΔX, ΔY, ΔZ) of all mesh points were computed and visualized in order to illustrate the overall surface deformation caused by the applied rotation, as shown in Figure 4.8.

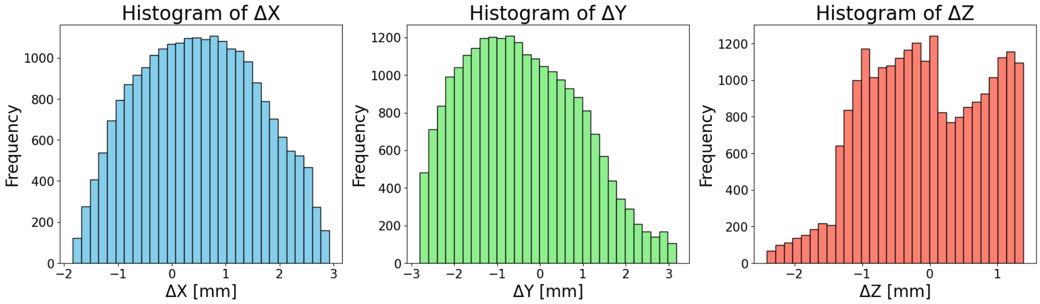

[A] [B] [C]

Figure 4.8: Histograms of coordinate displacements [A] ΔX, [B] ΔY, and [C] ΔZ for patient 21, obtained by applying the mean rotational values calculated across the 15 fractions.

4.2.1 Results

In order to evaluate how rotational errors may affect different anatomical configurations, a series of simulations was conducted on three representative patients: patient 13, patient 21 and patient 34. These patients were selected because they reflect a range of breast volumes: a small volume (176 mL, for patient 13), a medium volume (540 mL, for patient 21), and a large volume (1330 mL, for patient 34).

For each case, two scenarios were analyzed: a positive rotation of $+3^\circ$ and a negative rotation of -3° simultaneously applied around the pitch, roll, and yaw axes.These simulated rotations were chosen to represent the maximum angular deviations that are typically tolerated in clinical practice.
For each patient, the analysis focused on quantifying:

- the 3D shift of the point farthest from the isocenter, which is the indicator of the maximal surface deviation resulting from rotation;
- the range of coordinate displacements (ΔX, ΔY, ΔZ) across the entire breast surface.

The results obtained for patient 13, characterized by a small breast volume, are summarized in Table 4.8. Panel [A] reports the displacements induced by a $+3^\circ$ rotation around the pitch, roll, and yaw axes, while panel [B] shows the corresponding values resulting from a -3° rotation.

	ΔX [mm]	**ΔY [mm]**	**ΔZ [mm]**
Minimum	-4.7	-5.2	-1.6
Maximum	2.4	4.3	3.5
3D shift	6.5		

[A]

	ΔX [mm]	**ΔY [mm]**	**ΔZ [mm]**
Minimum	-1.8	-4.8	-3.3
Maximum	4.4	5.4	1.6
3D shift	6.6		

[B]

Table 4.8: Simulated rotational displacements for patient 13 (low breast volume)

The results obtained for patient 21, characterized by a medium breast volume, are summarized in Table 4.9. Panel [A] reports the displacements induced by a $+3^\circ$ rotation around the pitch, roll, and yaw axes, while panel [B] shows the corresponding values resulting from a -3° rotation.

	ΔX [mm]	**ΔY [mm]**	**ΔZ [mm]**
Minimum	-5.9	-6.2	-2.2
Maximum	3.4	5.4	3.9
3D shift	7.7		

[A]

	ΔX [mm]	**ΔY [mm]**	**ΔZ [mm]**
Minimum	-2.9	-5.9	-4.1
Maximum	5.7	6.5	2.3
3D shift	7.9		

[B]

Table 4.9: Simulated rotational displacements for Patient 21 (medium breast volume).

The results obtained for patient 34, characterized by a large breast volume, are summarized in Table 4.10. Panel [A] reports the displacements induced by a $+3^\circ$ rotation around the pitch, roll, and yaw axes, while panel [B] shows the corresponding values resulting from a -3° rotation.

	ΔX [mm]	**ΔY [mm]**	**ΔZ [mm]**
Minimum	-8.9	-6.8	-4.4
Maximum	3.3	7.4	4.9
3D shift	11.0		

[A]

	ΔX [mm]	**ΔY [mm]**	**ΔZ [mm]**
Minimum	-2.7	-7.9	-5.2
Maximum	8.9	7.1	4.5
3D shift	11.4		

[B]

Table 4.10: Simulated rotational displacements for Patient 34 (high breast volume).

The 3D shift value refers to the Euclidean displacement of the single surface point located farthest from the isocenter, before and after the simulated rotation; and due to the rigid nature of the transformation, this point always experiences the overall largest spatial deviation.

The 3D shift ranged from 6.5 mm in the small volume breast (patient 13) to over 11 mm in the large volume breast (patient 34); in this specific case displacements of nearly 9 mm were observed, confirming that the way rotational errors affect the surface depend on the breast size and shape of the patient.

Furthermore, it is important to note that the minimum and maximum values of ΔX, ΔY, and ΔZ refer to the range of coordinate displacements computed across all mesh points for each anatomical axis individually; for this reason, these extrema may originate from different surface points and do not necessarily correspond to the same location on the mesh.

A Pearson correlation analysis revealed a strong positive relationship between breast volume and the 3D shift induced by +3° rotational errors ($r = 0.84$, p-value < 0.0001). This finding confirms that larger breast volumes are associated with greater geometric deviations under rigid angular displacements.
This relationship is graphically illustrated in Figure 4.9, where the 3D shift caused by simulated +3° rotations is plotted against the corresponding breast volume for each patient. In this scatter plot each dot represents a single patient, and the green band indicates the 95% confidence interval for the linear regression.

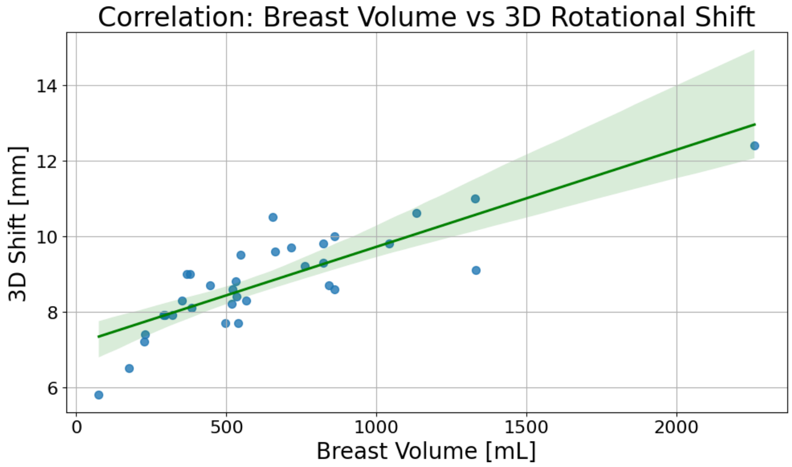

Figure 4.9: Scatterplot showing the correlation between breast volume and 3D displacement induced by simulated +3° rotational errors.

4.2.2 Discussion

Overall, the simulations showed that as the breast volume increased, both the 3D shift of the point farthest from the isocenter and the range of surface displacements (ΔX, ΔY, ΔZ) became larger. These geometric changes were seen for both +3° and −3° rotations, and their magnitude varied across the three patients.

These findings confirm that even residual rotations within the commonly accepted threshold of $\pm 3^\circ$ can cause significant surface deviations, particularly in patients with large or irregular breast anatomy; for example, in patient 34 (the one with the largest breast volume), the 3D shift exceeded 10 mm despite the angular displacements remaining within the clinically acceptable tolerance. Furthermore, the displacements observed, especially in medium and large breasts, were spatially heterogeneous, with great asymmetries in coordinate shifts along the three axes.

It is important to note that the simulations reported in this chapter were based on rigid-body assumptions, but, in clinical practice, breast tissue may undergo deformations rather than behaving as a perfect solid; anyway, since the observed geometric deviations are significant, even small rotational inaccuracies should be considered.
For example, in techniques such as VMAT, where steep dose gradients are used to spare surrounding healthy tissue, even small misalignments can result in suboptimal target coverage or unintended exposure of near organs.

Taken together, these results suggest that angular corrections falling between -3° and $+3^\circ$ can't be ignored since they may not provide sufficient accuracy in specific anatomical configurations. While standard couches still have technical limitations that prevent automatic rotational corrections, these findings highlight the potential benefits of using couches that allow rotational adjustments.

The results obtained indicate that both rotational and translational setup errors can have a considerable impact on the treatment geometry and on the delivered dose. In section 5, the dosimetric implications of positioning inaccuracies will be investigated by simulating the potential dose coverage degradation that could occur in the absence of CBCT based corrections.

5 Dosimetric Effect of Residual Errors in DIBH Treatments

In this chapter the dosimetric consequences of uncorrected setup errors evaluated through CBCT in breast cancer patients treated in DIBH are investigated.

In the first part of the chapter, treatment plans were recalculated for every patient by introducing the average isocenter displacements observed in clinical practice, and the resulting dose-volume histograms (DVHs) were compared to the original plans.
Moreover, rotational uncertainties were also simulated in order to assess their influence on target coverage and dose to organs at risk (OARs).

In the end, a gamma analysis was performed to quantify the overall agreement between planned and perturbed dose distributions.

5.1 Dosimetric impact of translational residual errors

As previously described in section 1 and section 2, the radiotherapy workflow for breast cancer patients begins with the acquisition of a planning CT scan. Based on this CT, radiation oncologists first define the clinical contours of the target volume and the surrounding organs at risk, then medical physicists create an individualized treatment plan using one of the radiotherapy planning techniques introduced in section 1.

After the approval of the treatment plan, the actual radiotherapy sessions begin, consisting of either 15 or 5 fractions delivered at a rate of one fraction per day, according to the clinical protocol. During these treatment sessions, as explained in section 2, patient positioning is first performed with the room lasers, then it is carefully monitored and corrected by the Catalist®, and finally a CBCT is performed to ensure accurate dose delivery. However, in scenarios where cone beam computed tomography (CBCT) verification is not performed, small residual positioning errors may remain uncorrected.

The dosimetric impact of such uncorrected setup errors is investigated by focusing on translational displacements of the isocenter; in fact, for each patient, the average residual shifts along the lateral (X), longitudinal (Y), and vertical (Z) axes reported in Table B.1, were applied to the isocenter of the original plan, and the dose distribution was recalculated and compared with the original one.

5.1.1 Treatment Plan Recalculation Using Pinnacle® Software

The clinical treatment plans were recalculated using the Pinnacle® treatment planning system [50]; the approved plan, corresponding to the one actually delivered, was modified by applying the average isocenter displacements along the lateral (X), longitudinal (Y), and vertical (Z) axes, as shown in Figure 5.1.

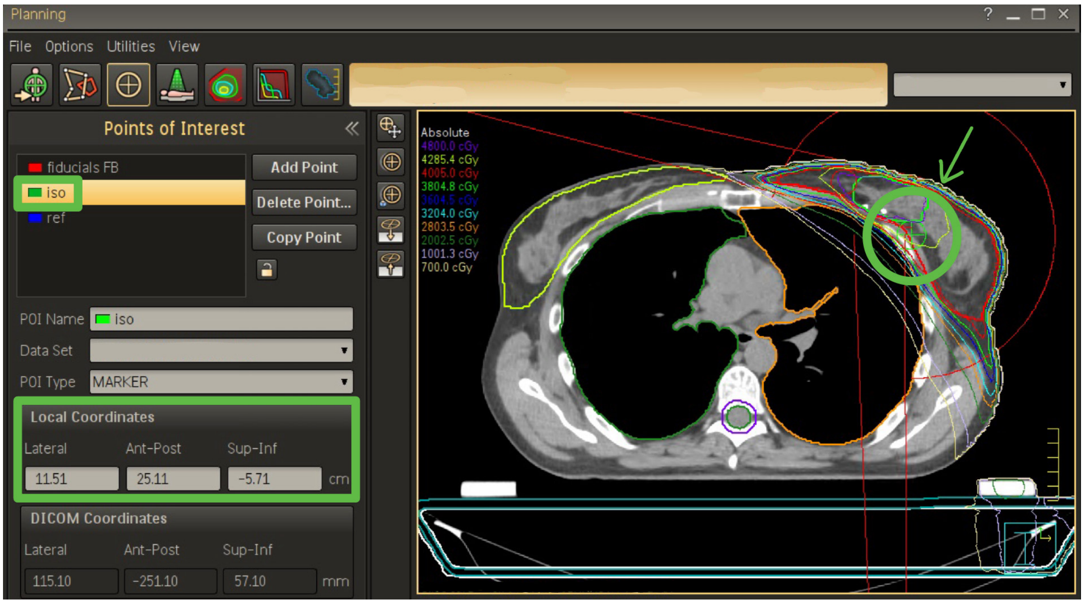

POI Name: iso

Data Set:

POI Type: MARKER

Local Coordinates

Lateral	Ant-Post	Sup-Inf	
11.51	25.11	-5.71	cm

DICOM Coordinates

Lateral	Ant-Post	Sup-Inf	
115.10	-251.10	57.10	mm

Figure 5.1: Visualization of the treatment isocenter (green circle) within the Pinnacle® treatment planning system. Its local coordinates are highlighted in green in the left panel, and were modified to simulate the average isocenter shifts applied for the dosimetric recalculation.

The choice to use average translational values was made to reflect the average effect on the treatment plan. During this analysis, the breast was considered as a rigid structure, which means that the same translational shift was assumed to affect the entire volume uniformly. This simplification allows a direct estimation of how isocenter translations could influence the dose distribution in the absence of rotational correction or anatomical deformation.

Rotational components were not included in this recalculation because Pinnacle® does not allow the application of rotational offsets to the isocenter within the clinical plan.

After the recalculation, the corresponding RTDOSE files were exported for further analysis in Python. Additionally, the original RTSTRUCT files, already described in section 4, that contain the breast region of interest and the isocenter point, were used to extract the relevant dosimetric parameters from both the original and modified dose distributions. In addition to evaluating changes in target coverage, the analysis also considered the dose received by the main organs at risk in left-sided breast cancer treatments: the heart, the left anterior descending coronary artery (LAD), and the contralateral breast.

5.1.2 DVH Analysis of Target and Organs at Risk

The analysis was performed on the 30 patients of the cohort described in subsection 3.1 treated with the 15 fractions regimens; while patients treated with the 5 fractions regimens were excluded from this evaluation due to their distinct hypofractionated protocol and shorter treatment course.
Among the included patients, seven were planned using the butterfly VMAT technique, sixteen with standard VMAT, three with 3D-CRT, and four with a combined 3D-CRT and VMAT approach.

As an initial quality criterion, the D_{90}, defined as the minimum dose received by 90% of the target volume, was required to be at least 90% of the prescription dose, corresponding to 36 Gy in this cohort.
Then, a more stringent condition was applied: the D_{95}, which is the dose received by 95% of the target, had to reach at least 90% of the prescribed value [51] [52].
In addition, a minimum absolute dose of 25 Gy was required for the ipsilateral breast to ensure adequate coverage and prevent underdosage in peripheral regions; the minimum dose is a pointwise (single-voxel) metric.

Dose constraints for the main organs at risk in left-sided breast cancer radiotherapy were considered according to current literature:

- For the heart, both the mean and maximum dose were evaluated, with typical recommended limits of $D_{mean} < 2.5$ Gy and $D_{max} < 30$ Gy [53].
- For the contralateral breast, in Istituto Oncologico per lo studio dei tumori IRST (IR-

CCS) ”Dino Amadori” a mean dose below 1.5 Gy and a maximum dose not exceeding 6 Gy are considered acceptable.

- For the left anterior descending (LAD) coronary artery, only the maximum dose was assessed, and reference values suggest a maximum dose below 18 Gy [54].

The values of the dosimetric parameters discussed in this section, calculated for the original plan, the modified plan with isocenter shift, and their percentage differences are namely reported, for all the patients of this cohort, in Table C.1, Table C.2 and Table C.3.

5.1.3 Results of the Comparison Between Original and Shifted Plans

Out of the initial cohort of 30 patients treated with the 15 fractions regimen, 8 were excluded from this analysis because the minimum dose delivered to the ipsilateral breast in the original approved treatment plan was found to be below 25 Gy. Although these plans had been clinically accepted, the suboptimal coverage was likely due to specific technical and anatomical considerations, such as breast shape, respiratory motion, or positioning constraints, which fall outside the scope of this analysis.

When comparing the distribution of techniques between included and excluded cases, it was observed that patients whose original plans delivered less than 25 Gy to the breast were predominantly treated with 3D-CRT or standard VMAT. Specifically, three out of seven butterfly VMAT patients and four out of sixteen standard VMAT patients were excluded due to insufficient minimum dose coverage. In contrast, two out of three patients planned with 3D-CRT and all four planned with the hybrid 3D + VMAT technique were included in the analysis.

Among the remaining 22 patients included in the dosimetric evaluation, 18% was treated with the butterfly VMAT technique, 55% with standard VMAT, 9% with 3D conformal radiotherapy (3D-CRT), and 18% with a hybrid 3D + VMAT technique.

The following results were observed when comparing the original plans with those recalculated using the average isocenter shifts:

- For all 22 patients included in the analysis, the D_{90} remained above 90% of the prescription dose (36 Gy) in the recalculated plans; thus no loss of target coverage below this threshold was observed following the application of the average isocenter shifts.

- The D_{95} was above 36 Gy (90% of the prescribed dose) in 21 out of 22 patients after the isocenter shifts. The only patient falling below this threshold was treated with the standard VMAT technique.
- Regarding the minimum dose to the ipsilateral breast, 7 out of the 22 patients showed a value below 25 Gy in the recalculated plan. Among these, two were treated with the hybrid 3D + VMAT technique, four with standard VMAT, and one with 3D-CRT.
  Notably, 3 of these 7 patients, namely patient 6, 31 and 33, also exhibited large 3D isocenter shifts, as shown in Table B.1, and were among the cases that presented inconsistencies between the elevation of the primary gating point measured by the Sentinel® system, and the elevation of the primary gating point evaluated from the planning CT scan in section 3.
- For the heart, the maximum dose remained below 30 Gy in all 22 patients, and the highest observed value was 19 Gy in a patient treated with the hybrid 3D + VMAT technique. Also the mean heart dose remained within acceptable limits, with no patient exceeding 2.5 Gy.
- Regarding the contralateral breast, 5 out of 22 patients exhibited a maximum dose exceeding 6 Gy in the recalculated plans. Among these, 3 were treated with standard VMAT, 1 with butterfly VMAT, and 1 with the hybrid 3D + VMAT technique. However, the mean dose to the contralateral breast remained below 1.5 Gy in all cases.
- For the left anterior descending (LAD) artery, only 2 out of 22 patients exhibited a maximum dose exceeding 18 Gy in the recalculated plans; both were treated with standard VMAT, but in one of these cases (patient 25), the LAD dose already exceeded 18 Gy in the original clinically accepted plan.

A summary of the patients who failed to meet one or more dosimetric constraints in the recalculated plans is shown in Table 5.1. For each case, the treatment technique and the specific parameters exceeding clinical thresholds are reported; in fact, a cross (✗) indicates that the corresponding constraint was violated.

Patient	Technique	D95	Ipsilateral min	LAD max	Controlateral max
4	3D+VMAT				✗
5	VMAT			✗	✗
6	VMAT		✗		
7	Butterfly				✗
14	Butterfly	✗			
18	VMAT		✗		✗
20	3D+VMAT		✗		
25	VMAT			✗	
27	VMAT		✗		✗
29	VMAT	✗	✗		
31	3D+VMAT		✗		
33	3D-CRT		✗		

Table 5.1: Summary of the 12 patients who violated at least one dosimetric constraint after the application of the average isocenter shift.

Figure 5.2 provides a boxplot representation of the percentual changes observed in key dosimetric endpoints after applying the average isocenter shifts. These include target-related parameters (D_{95}, ipsilateral breast minimum dose) and organ-at-risk metrics (LAD maximum dose, contralateral breast maximum dose, and heart mean dose).

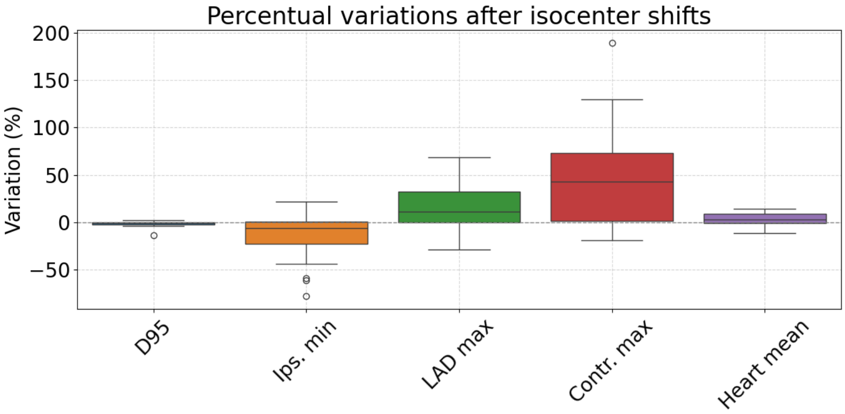

Figure 5.2: Boxplot of the percentual variations of key dosimetric parameters after applying average isocenter shifts.

To better visualize the impact of isocenter shifts on the minimum dose coverage of the ipsilateral breast, the relative percentage variation for each patient is reported in Figure 5.3. Since adequate target coverage is the most critical parameter in radiotherapy, particular attention was given to this metric. Patients whose recalculated minimum dose was below the clinical threshold of 25 Gy are highlighted in red.

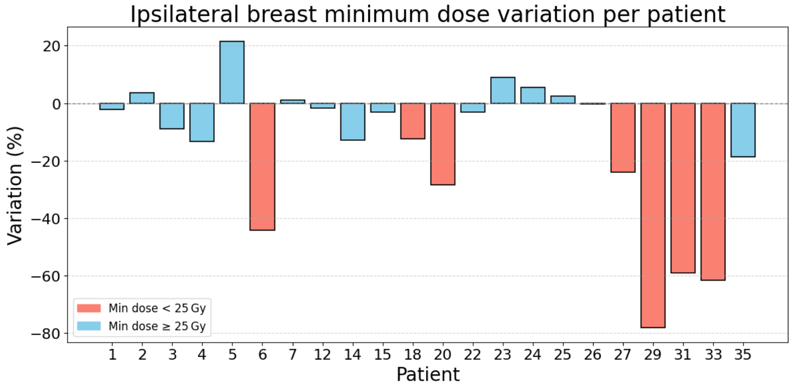

Figure 5.3: Percentage variation in the minimum dose delivered to the ipsilateral breast for each patient after the application of the average isocenter shift.

For clarity, these results come from thee dose recalculation of the approved plans after applying the average isocenter shifts; thus the perturbed doses were not delivered to patients. Moreover, the “minimum dose” is a pointwise metric (the lowest voxel within the contoured breast), not a dose level representative of the whole breast volume.

The scatter plot shown in Figure 5.4 was generated comparing the original D_{95} values with those obtained after the isocenter shift. This parameter is particularly relevant in clinical practice because it is commonly used to assess coverage quality. A linear regression was applied to visualize the overall trend and potential correlation.

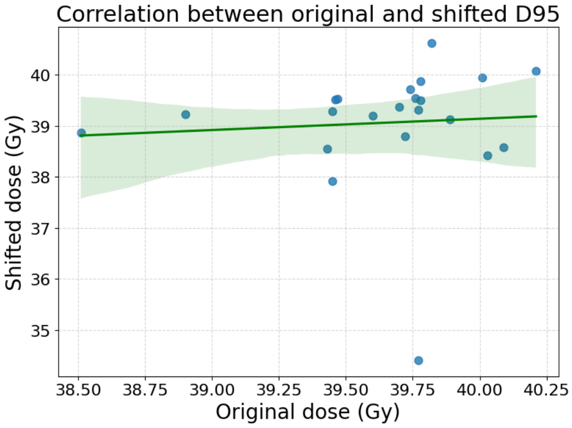

Figure 5.4: Correlation between the original and recalculated D_{95} values across the cohort.

In Figure 5.4, each point represents one patient, while the green line indicates the linear regression fit, with the shaded area corresponding to the 95% confidence interval.

To investigate the relationship between the original and post-shift D_{95} values, both Pearson and Spearman correlation analyses were performed. The Pearson correlation coefficient was found to be $r = 0.07$ (p-value $= 0.7643$), indicating a negligible linear correlation between the two sets of values. Similarly, the Spearman rank correlation yielded a coefficient of $\rho = 0.29$ (p-value $= 0.2001$), suggesting only a weak monotonic association.

To assess whether the observed dosimetric variations after isocenter shifts were statistically significant, a non-parametric Wilcoxon signed-rank test was performed for each parameter of interest; and the obtained results are summarized in Table 5.2. The choice of this test was motivated by the non-normal distribution of the data.

Metric	**Pre-shift (Mean ± SD) [Gy]**	**Post-shift (Mean ± SD) [Gy]**	**p-value**	**Interpretation**	**Effect Size (r)**
D_{90}	40.2 ± 0.3	39.9 ± 0.6	0.0213	Significant	0.49
D_{95}	39.7 ± 0.4	39.1 ± 1.2	0.0089	Significant	0.68
Ipsilateral min	31.8 ± 2.8	27.0 ± 7.9	0.0093	Significant	0.61
Heart max	7.4 ± 5.5	8.5 ± 6.2	0.0134	Significant	0.39
Heart mean	0.9 ± 0.4	0.9 ± 0.4	0.0513	Not Significant	0.28
Controlateral max	3.0 ± 1.4	4.5 ± 2.4	0.0009	Significant	0.75
Controlateral mean	0.7 ± 0.3	0.7 ± 0.3	0.0064	Significant	0.69
LAD max	6.1 ± 5.1	6.8 ± 5.0	0.0091	Significant	0.54

Table 5.2: Summary of dosimetric parameters before and after isocenter shifts.

All the considered dosimetric parameters were tested for statistically significant variations following isocenter displacements. As reported in Table 5.2, the Wilcoxon signed-rank test revealed statistically significant differences (p-value < 0.05) for the majority of metrics, including D_{90}, D_{95}, ipsilateral minimum dose, LAD maximum dose, and contralateral breast metrics.

In order to understand if these findings were influenced by the presence of clinical threshold violations, a subset analysis was performed considering only the 10 patients who did not exhibit any exceedance of the clinical thresholds in any of the evaluated metrics (see Table 5.1). For this subset of patients, namely patients 1, 2, 3, 12, 15, 22, 23, 24, 26 and 35, a Wilcoxon signed-rank test was repeated on the key dosimetric parameters. The results obtained are summarized in Table 5.3

Metric	**Pre-shift (Mean ± SD) [Gy]**	**Post-shift (Mean ± SD) [Gy]**	***p*-value**	**Interpretation**
D_{90}	40.2 ± 0.4	40.0 ± 0.4	0.1311	Not Significant
D_{95}	39.7 ± 0.5	39.4 ± 0.4	0.1313	Not Significant
Ipsilateral min	32.5 ± 2.4	31.7 ± 2.0	0.8462	Not Significant
Heart max	7.8 ± 4.6	9.1 ± 5.9	0.2324	Not Significant
Heart mean	0.9 ± 0.4	0.9 ± 0.3	0.2131	Not Significant
Controlateral max	2.9 ± 1.1	3.7 ± 1.5	0.0911	Not Significant
Controlateral mean	0.6 ± 0.2	0.7 ± 0.2	0.6483	Not Significant
LAD max	5.5 ± 3.1	6.1 ± 3.0	0.1932	Not Significant

Table 5.3: Wilcoxon signed-rank test results for the subset of 10 patients who did not violate any clinical dose constraints in the recalculated plans.

As shown in Table 5.3, none of the evaluated parameters demonstrated statistically significant variations (p-value > 0.05).
In particular, the parameters with the lowest p-values were D_{90} and D_{95} (both around 0.13), showing a tendency toward a slight reduction after the isocenter shifts. In contrast, the metrics for organs at risk, including heart mean, heart max, contralateral max, and

LAD max doses, displayed higher *p*-values (all above 0.19), indicating that these structures were less affected by the applied shifts in this subgroup of patients.

5.1.4 Discussion

The dosimetric analysis performed in this study highlights how small residual translational setup errors, even when averaged across treatment fractions, can significantly affect both target coverage and organs at risk (OARs) sparing in left-sided breast radiotherapy. Despite the apparent simplicity of a rigid isocenter displacement, the clinical consequences can be neither uniform nor negligible.

The observed decrease in D_{90} and D_{95} following the application of average isocenter shifts was found to be statistically significant, even if clinically moderate.
In all cases, the D_{90} remained above 90% of the prescribed dose (36 Gy), which is typically considered the minimum acceptable threshold for adequate target coverage. This suggests that, despite minor positional uncertainties, the robustness of the treatment plans was sufficient to ensure clinically acceptable dose delivery to at least 90% of the target volume.
Although the reduction in D_{95} was more pronounced than that of D_{90}, it did not significantly compromise treatment quality for most patients. In fact, only one case fell below the stricter threshold of 38 Gy, and even then, the value was just slightly under the limit. This outcome is clinically reassuring, especially considering that D_{95} is known to be more sensitive to small underdosages in peripheral regions, particularly in patients with non standard anatomy or larger isocenter displacements.
Furthermore, when looking at the correlation between the original and post-shift D_{95} values, the results confirmed the unpredictable nature of these changes. The Pearson correlation was low ($r = 0.07$), and Spearman's rank correlation was only slightly higher ($\rho = 0.29$), indicating that patients with good initial coverage did not necessarily maintain it after the isocenter shift. A possible explanation lies in the fact that the applied isocenter shifts were not the same for all patients, but specific to each case. Therefore, even when two patients had similar baseline D_{95} values, the effect of the shift on their dose distribution could vary greatly, depending on the direction and magnitude of their individual residual errors.

The minimum dose to the ipsilateral breast exhibited the most substantial variation after shift application, with 7 out of 22 patients falling below the 25 Gy threshold in the recalculated plans. This parameter is particularly sensitive to geometric inaccuracies, because shifts in isocenter can lead to either an increase or a redistribution of peripheral dose, depending on their direction and magnitude [55]. Nevertheless, it is important to note that this metric often reflects low-dose regions in the breast contour and may not correspond to clinically significant underdosage if the central portion of the target remains well covered. Moreover, among the affected patients, several were characterized by large residual displacements and inconsistencies in respiratory surrogate elevation, as highlighted earlier in section 3.

While the mean and the maximum heart dose remained well below recommended limits for all patients, the maximum doses to LAD showed a modest but statistically significant increase after the isocenter shift. These changes were generally within acceptable clinical thresholds, with only a few patients exceeding the recommended maximum dose for the LAD. Although the Wilcoxon test confirmed the significance of these differences, the effect size for the heart was relatively small, suggesting a limited clinical impact. For the LAD, the effect was slightly more pronounced, yet still remained within tolerance for the majority of the cohort. These findings highlight the importance of monitoring dose distribution near critical structures, especially in VMAT plans where steep dose gradients can make the maximum dose more sensitive to small positional variations.

Moreover, the contralateral breast showed some of the most significant changes after the isocenter shift, particularly in terms of maximum dose. This may be due to small changes in beam angles caused by the applied shifts, which can result in unintended low-dose exposure to the opposite breast. Although the mean dose remained low for all patients, five cases exceeded the recommended maximum dose of 6 Gy. This suggests that even small inaccuracies in patient positioning can have an effect on areas far from the treatment target.

The fact that patients treated with butterfly VMAT or hybrid techniques showed more sensitivity to shifts suggests that the choice of planning technique has a direct impact on the robustness of the treatment plan. It’s important to notice that the decision to exclude 8 patients with originally low minimum breast doses from the statistical analysis was reasonable from both a methodological and clinical perspective; in fact, even if those plans were approved, they likely reflected special clinical choices or constraints. Including them could have added variability that wasn't really due to the isocenter shifts.

The secondary analysis focused on the subset of patients who did not show any violations of clinical dose constraints in the recalculated plans, to assess whether dosimetric variations were still present under the most stable conditions. As reported in Table 5.3, the Wilcoxon signed-rank test confirmed that none of the evaluated parameters exhibited statistically significant differences. The D_{90} and D_{95} metrics showed the lowest p-values, higlighting a potential sensitivity of target coverage to geometric variations even when overall clinical thresholds are respected. On the other hand, heart and contralateral breast doses, including the maximum LAD dose, remained more stable, with higher p-values consistently above 0.1932. These findings suggest that, while critical structures are less affected under optimal conditions, small shifts in target coverage may still occur, thus requiring careful monitoring especially in the early treatment fractions.

From a clinical workflow perspective, these results support the adoption of a personalized verification strategy. In particular, performing CBCT scans during the first few treatment fractions, followed by a recalculation of the treatment plan using the observed average shifts, as done in this study, could help determine whether key dose constraints are respected. If the new plan remains in accordance with the approved one, CBCTs could be reduced or discontinued; conversely, persistent deviations could justify daily imaging for improved accuracy.

5.2 3D Global and Local Gamma Analysis in Representative Cases

In order to better understand the clinical impact of uncorrected isocenter shifts on the full 3D dose distribution, both local and global gamma index analyses were performed. This evaluation was conducted on two representative patients: one with excellent agreement (patient 1) and one showing major discrepancies between the original and shifted treatment plans (patient 29).

For each voxel, the gamma index was calculated using the standard 3D formula:

$$\gamma = \min_j \sqrt{\left(\frac{\Delta D_j}{\Delta D_{\text{crit}}}\right)^2 + \left(\frac{\Delta r_j}{\Delta r_{\text{crit}}}\right)^2} \tag{5.1}$$

where ΔD_j is the dose difference between the reference (original) and evaluation (shifted) plans, Δr_j is the spatial distance between the evaluated voxel and a neighboring voxel, ΔD_{crit} is the dose difference tolerance, and Δr_{crit} is the spatial distance tolerance [56].

The gamma index was computed in three dimensions using two different criteria:

- Local gamma: 5% dose difference (relative to each voxel's dose) and 3 mm distance to agreement, to test the robustness of the planning technique.
- Global gamma: 3% dose difference (relative to the maximum dose in the volume) and 2 mm distance to agreement, as used in clinical practice for patient quality assurance (QA) verification.

Voxels with a gamma index $\gamma \leq 1$ were considered in agreement with the reference dose distribution, indicating that both spatial and dosimetric tolerances were satisfied.

5.2.1 3D Gamma Evaluation Procedure

The gamma analysis was performed using a Python script developed specifically for this study. For each patient, the DICOM RTSTRUCT file already discussed in section 4, which contains the ROI of the ipsilatera breast and point of the isocenter of the treatment, was used to convert the contour of the breast into a 3D binary mask.
In order to ensure a sufficient margin for dose interpolation and gamma evaluation, the mask was isotropically dilated by 10 mm.

The dose matrices from the original and shifted treatment plans (RTDOSE) were interpolated on a high-resolution voxel grid, obtained by doubling the resolution of the original dose grid in all spatial directions. Dose values were computed at each voxel using trilinear interpolation. Only the voxels located inside the breast mask and receiving at least 10% of the maximum dose in the original plan were retained for gamma evaluation.
Then, to focus the analysis on the clinical target volume (CTV) rather than the full planning target volume (PTV), the outermost 3 mm shell of the original breast ROI was excluded using an Euclidean distance transform.
At this point, both local and global 3D gamma indices were computed. In the local formulation, the dose difference was normalized to the dose at each reference voxel (5% tolerance), whereas in the global formulation, it was normalized to the maximum dose

in the volume (3% tolerance). The spatial distance criteria were 3 mm and 2 mm for the local and global analyses, respectively. For each voxel, the gamma value was computed according to Equation 5.1, by comparing the reference dose with all neighboring voxels within the spatial tolerance, and retaining the minimum γ value. Voxels with $\gamma \leq 1$ were considered in agreement with the reference distribution.

For each of the two cases in this analysis, the results were visualized through interactive 3D scatter plots, showing the spatial distribution of passing and failing voxels before and after the exclusion of the external shell. Gamma value histograms were also generated, and the percentage of passing voxels was computed for both gamma types.

In the end, in addition to the gamma analysis, dose-volume histograms (DVHs) were extracted from both dose distributions of the original and recalculated plans, and the following dosimetric parameters were calculated: D_{95}, D_{90}, and D_{min} (approximated as $D_{99.9}$ to reduce sensitivity to outliers).

5.2.2 Results

Figure 5.5 shows the 3D rendering of the ipsilateral breast region used for the local gamma analysis of patient 1. The RTSTRUCT contour was converted into a point cloud by resampling the volume on an isotropic grid. Each point is coloured by its local gamma value comparing the original and shifted dose distributions: green for $\gamma \leq 1$ and red for $\gamma > 1$.

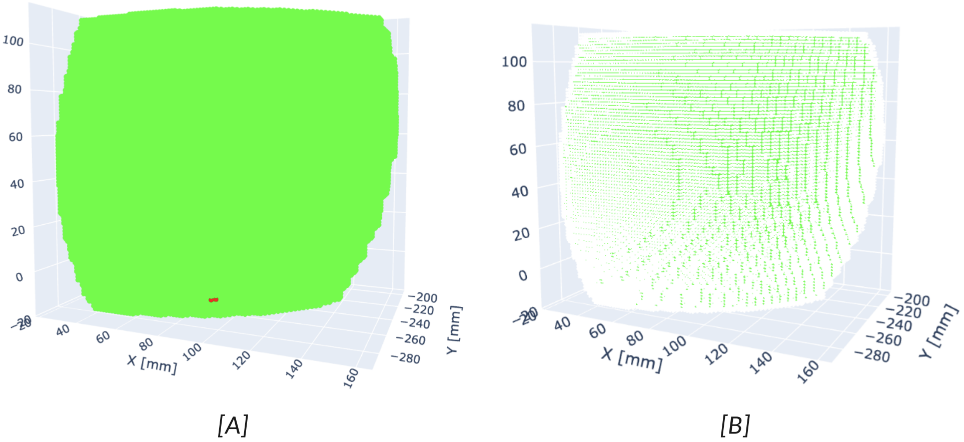

Figure 5.5: 3D spatial distribution of gamma index values for Patient 1: [A] full voxel cloud, and [B] remaining volume after exclusion of the outer 3 mm shell.

Figure 5.6 show the histograms of the local gamma index distribution before and after shell removal for patient 1 of this study.

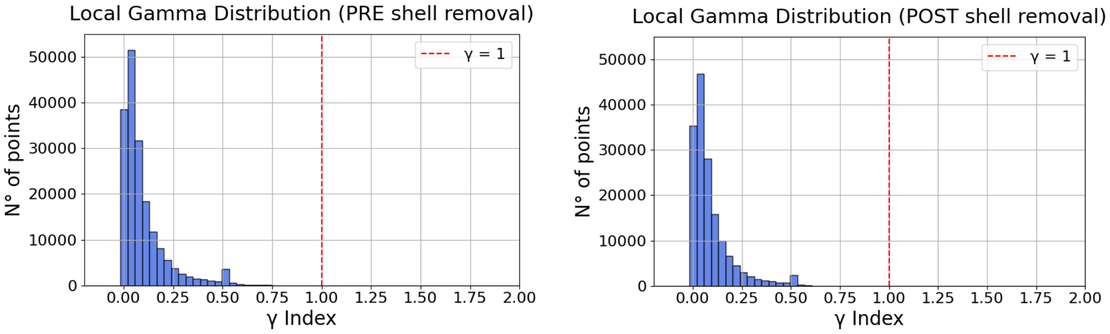

[A] *[B]*

Figure 5.6: Histograms of the local gamma index distribution for patient 1: [A] distribution for the full volume before shell exclusion, and [B] distribution after the exclusion of the outer 3 mm shell.

For patient 1, selected as a representative case with excellent agreement between the original and shifted dose distributions, 99.9% of the voxels passed the local gamma test ($\gamma \leq 1$), while after the exclusion of the outer 3 mm shell, the pass rate became 100%.

Figure 5.7 shows the 3D spatial distribution of global gamma values for patient 1 of this study.

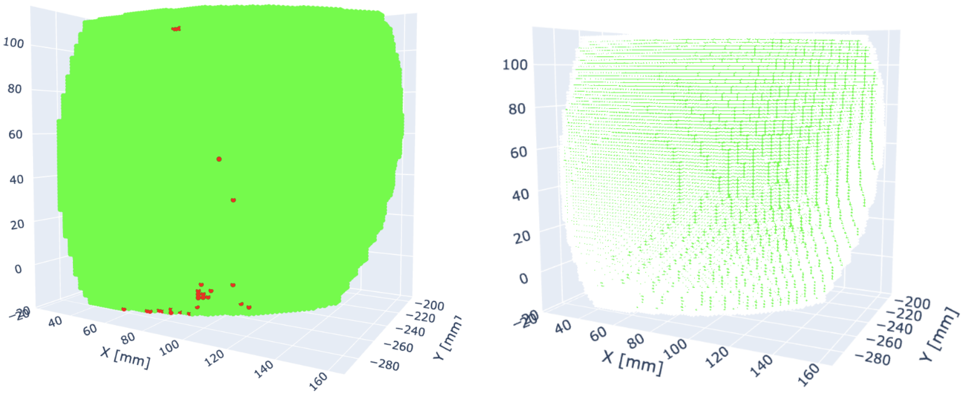

[A] *[B]*

Figure 5.7: 3D spatial distribution of global gamma index values for patient 1: [A] full voxel cloud, and [B] remaining volume after exclusion of the outer 3 mm shell.

Figure 5.8 show the histograms of the local gamma index distribution before and after shell removal for patient 1 of this study.

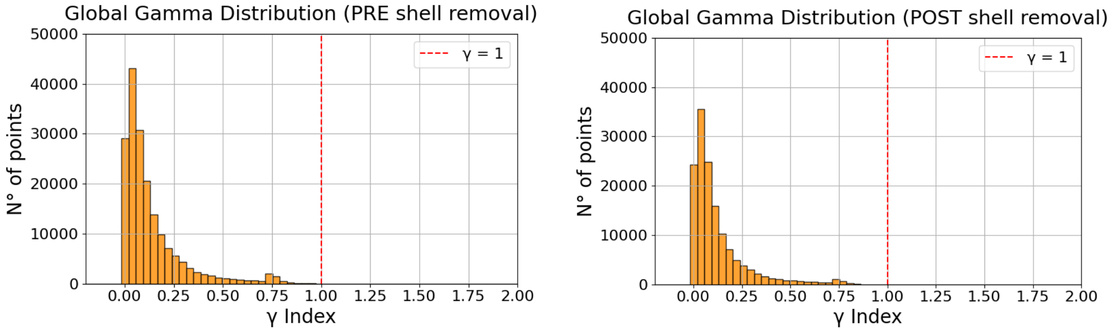

[A] *[B]*

Figure 5.8: Histograms of the global gamma index distribution for patient 1: [A] distribution for the full volume before shell exclusion, and [B] distribution after the exclusion of the 3 mm shell.

Before shell exclusion, the pass rate was 99.9%, while after the exclusion of the outer 3 mm shell, all of the evaluated voxels passed the gamma test, yielding a post-exclusion pass rate of 100%.

Figure 5.9 reports the dose–volume histograms (DVHs) for patient 1, comparing the original and shifted treatment plans within the breast ROI.
The curves illustrate the cumulative dose distribution, while the vertical dashed lines mark the corresponding D_{90}, D_{95}, and D_{min} values used for quantitative assessment.

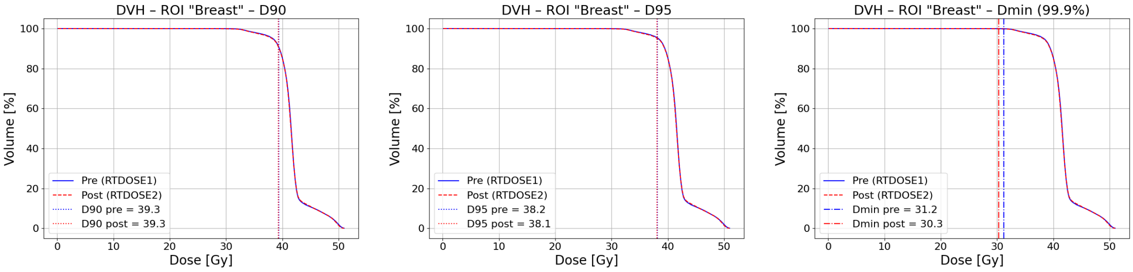

(A) D_{90} *(B) D_{95}* *(C) D_{min} ($D_{99.9}$)*

Figure 5.9: DVH comparison between original and shifted plans for the breast ROI in patient 1. The vertical dashed lines indicate the [A] D_{90}, [B] D_{95}, and [C] D_{min} values respectively.

The DVH analysis for the breast ROI in patient 1 showed a slight reduction in D_{90}, from 39.4 Gy in the original plan to 39.3 Gy in the shifted plan, corresponding to a variation of

−0.1%. The D_{95} also exhibited a minimal decrease, from 38.2 Gy to 38.1 Gy (−0.3%). A more noticeable difference was observed in the D_{min} ($D_{99.9\%}$), which decreased from 31.2 Gy to 30.3 Gy, reflecting a variation of −2.8%.

The same analysis was repeated also for patient 29; in fact, Figure 5.10 shows the spatial distribution of local gamma values for patient 29 of this study.

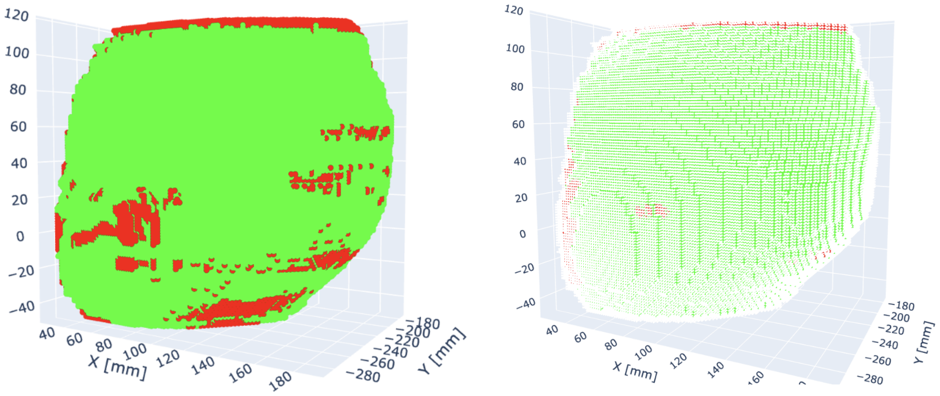

[A]

[B]

Figure 5.10: 3D spatial distribution of global gamma index values for patient 29: [A] full voxel cloud, and [B] remaining volume after exclusion of the outer 3 mm shell.

Figure 5.11 show the histograms of the local gamma index distribution before and after shell removal for patient 29 of this study.

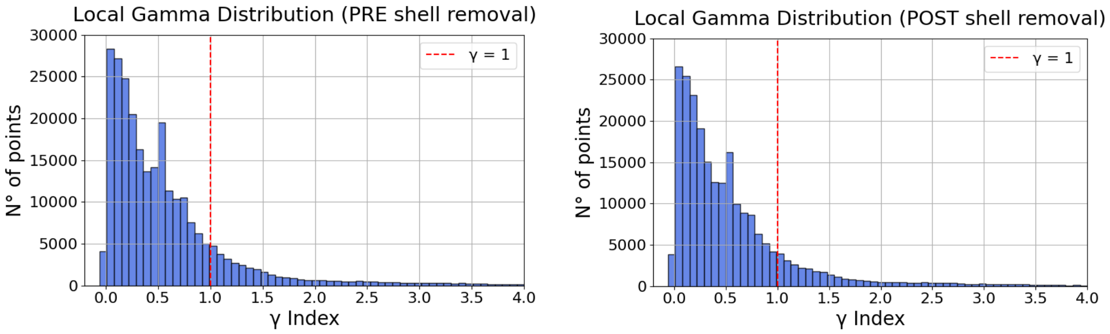

[A]

[B]

Figure 5.11: Histograms of the local gamma index distribution for patient 29: [A] distribution for the full volume before shell exclusion, and [B] distribution after the exclusion of the 3 mm shell.

Figure 5.12 shows the 3D spatial distribution of global gamma values for patient 29 of this study.

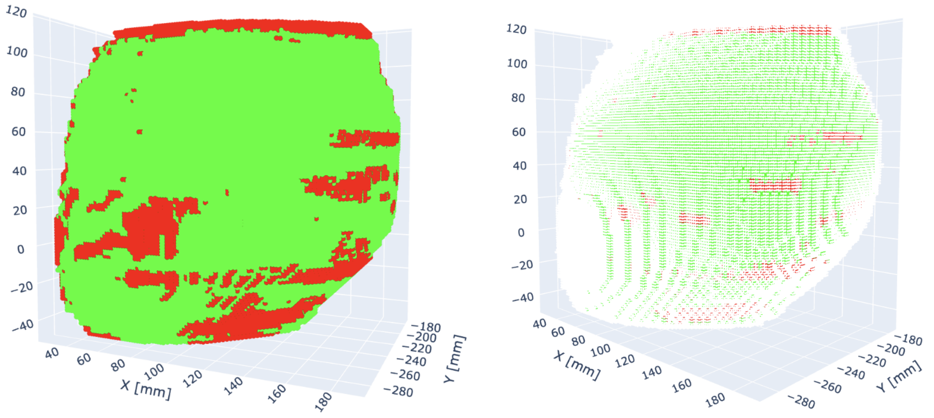

[A] *[B]*

Figure 5.12: 3D spatial distribution of global gamma index values for patient 29: [A] full voxel cloud, and [B] remaining volume after exclusion of the outer 3 mm shell.

Figure 5.13 show the histograms of the local gamma index distribution before and after shell removal for patient 29 of this study.

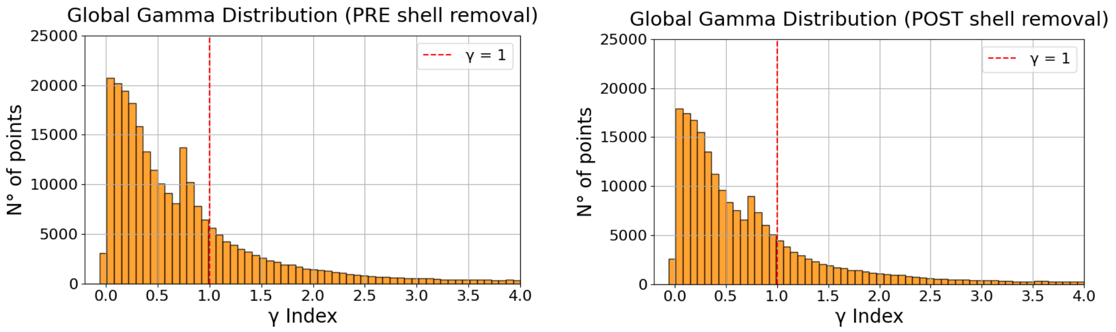

[A] *[B]*

Figure 5.13: Histograms of the global gamma index distribution for patient 29: [A] distribution for the full volume before shell exclusion, and [B] distribution after the exclusion of the 3 mm shell.

For patient 29, who was selected due to the larger isocenter shifts applied to her treatment plan, a lower degree of agreement between the original and shifted dose distributions was observed. In fact, for local gamma analysis, before the exclusion the gamma pass rate was 84.1%, while after removing the peripheral region, the pass rate ($\gamma \leq 1$) increased slightly to 86.4%.

The global gamma analysis for patient 29 further confirmed the reduced agreement caused by the larger isocenter displacements. Before excluding the 3 mm shell, the gamma pass rate was 71.9%, and after the remotion of the peripheral shell, the pass rate improved slightly to 75.0%.

Figure 5.14 reports the dose–volume histograms (DVHs) for patient 29, comparing the original and shifted treatment plans within the breast ROI.
The curves illustrate the cumulative dose distribution, while the vertical dashed lines mark the corresponding D_{90}, D_{95}, and D_{min} values used for quantitative assessment.

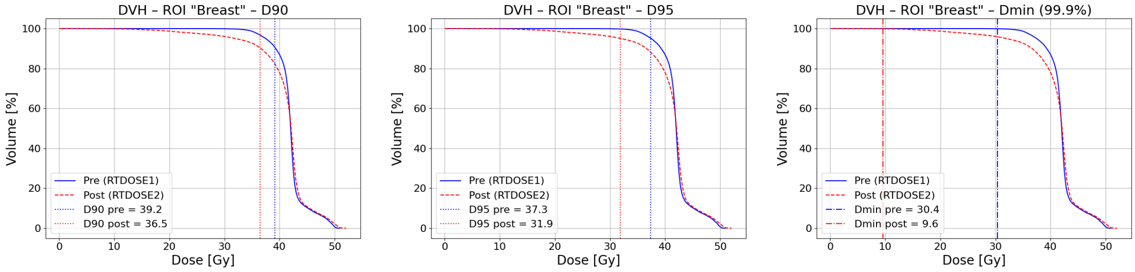

(A) D_{90} (B) D_{95} (C) D_{min} ($D_{99.9}$)

Figure 5.14: DVH comparison between original and shifted plans for the breast ROI in patient 29. The vertical dashed lines indicate the [A] D_{90}, [B] D_{95}, and [C] D_{min} values respectively.

The DVH analysis of the breast ROI for Patient 29 revealed substantial dosimetric differences between the original and shifted dose distributions. The D_{90} decreased from 39.2 Gy to 36.5 Gy, corresponding to a variation of -6.9%. An even larger drop was observed for D_{95}, which decreased from 37.3 Gy to 31.9 Gy (-14.6%). The most pronounced discrepancy was seen in the minimum dose (D_{min}), which fell from 30.4 Gy to 9.6 Gy, resulting in a variation of -68.4%.

5.2.3 Discussion

The results obtained in this analysis highlight a substantial variability in the dosimetric impact of isocenter shifts among different patients. The comparison between patient 1 and patient 29 illustrates two extreme scenarios; in fact, while patient 1 showed almost perfect agreement between original and shifted dose distributions, patient 29 exhibited pronounced discrepancies.

In particular, patient 1 reached a 100% gamma pass rate after shell exclusion, for both local and global analyses. Such excellent agreement, even with stringent criteria (3%/2mm for global, 5%/3mm for local), supports the feasibility of reducing daily CBCT imaging in selected patients.
For this subgroup of patients, as proposed above, a possible strategy could involve performing both SGRT-based positioning and CBCT verification in the initial treatment fractions; then, if the dosimetric consistency is confirmed by the gamma analysis, subsequent treatments could rely on surface guidance alone, thus reducing the frequency of daily CBCT imaging.

Conversely, for patients like patient 29, who exhibited significant isocenter shifts and poor dosimetric agreement, daily CBCT remains indispensable to ensure accurate target coverage and to avoid potential overdosing of organs at risk like the hearth, LAD or controlateral breast.

Overall, these findings suggest that a more personalized imaging protocol could be implemented; in fact, while some patients clearly benefit from daily image guidance, others could be safely treated with less frequent imaging. This procedure is feasible as long as reliable verification methods, such as 3D gamma analysis performed with dedicated tools like the Python script developed in this study, are employed during the validation of the treatment plan.

5.3 Dosimetric impact of rotational residual errors

To evaluate the effect of rigid rotations of the target volume on the dose distribution, a small modification was introduced to the code described in subsection 5.2.
In particular, rotations around the three main anatomical axes (pitch, roll, and yaw) were applied, using the isocenter embedded in the RTSTRUCT file as the center of rotation.
This implementation enabled the simulation of angular misalignments that cannot be directly implemented within the Pinnacle® treatment planning system. By applying the rotation before the dose interpolation step, it was possible to assess the dosimetric impact of these rotations using gamma index analysis. The same gamma criteria used in subsection 5.2 were adopted: 5% / 3 mm for the local gamma index and 3% / 2mm for the global gamma index.

The gamma analysis was performed on the same two patients previously discussed subsection 5.2, namely patient 1 and patient 29, and for each patient, two different rotation scenarios were simulated: firstly, rigid rotations of +3° were applied simultaneously around all three anatomical axes. This scenario represents the maximum rotational correction that can be applied during a radiotherapy session.
Then, the average rotation values measured over the 15 treatment fractions, reported in Table B.2 and based on daily CBCT setup corrections, were applied to both patients. The goal of this second scenario was to estimate the dosimetric impact of realistic rotational errors that occurred during the actual treatment.

Furthermore, as in the previous analysis, the 3 mm outer shell was excluded. This choice was made to restrict the evaluation to the internal part of the target, in order to simulate dose variations within the gross tumor volume (GTV) and the clinical target volume (CTV), while excluding the outermost margins included in the planning target volume (PTV).

5.3.1 Results

For patient 1, a rigid rotation of +3° around all three anatomical axes was applied. The resulting local gamma distributions are showed in Figure 5.15.

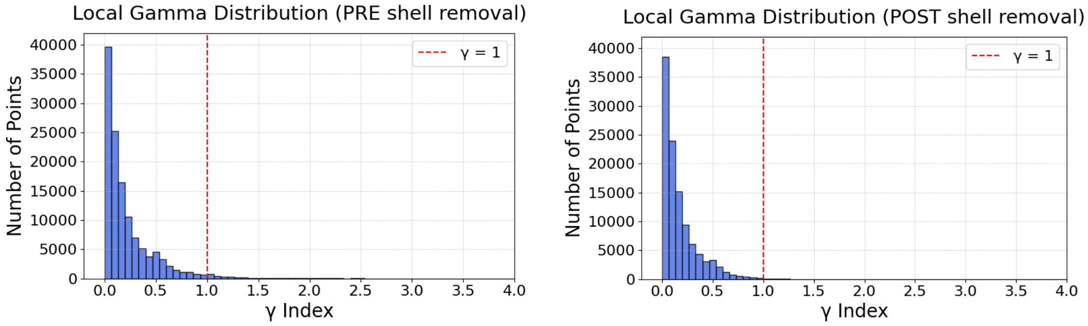

[A] *[B]*

Figure 5.15: Local gamma index distribution for patient 1, after +3° rotation: [A] before shell exclusion and [B] after shell exclusion.

When considering the full breast volume, including peripheral regions, the local gamma pass rate was 96.1%, while after the exclusion of the 3 mm outer shell, which corresponds to the outer margins of the PTV, the pass rate improved to 98.3%.

Moreover, the resulting global gamma distributions for a rigid rotation of +3° around all three anatomical axes are showed in Figure 5.16.

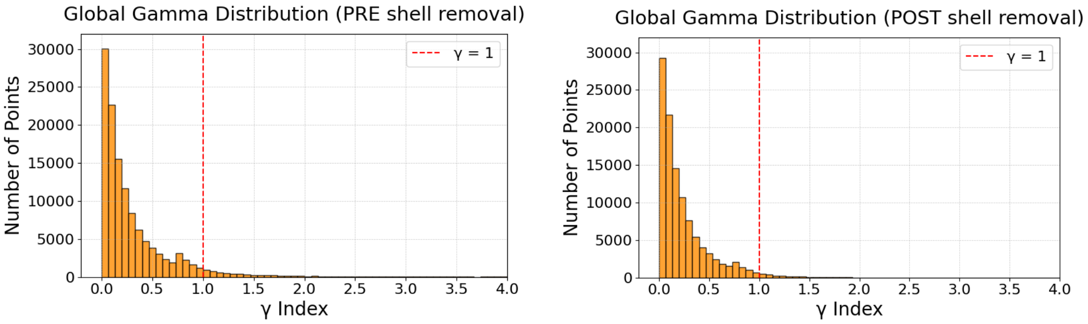

[A] *[B]*

Figure 5.16: Global gamma index distribution for patient 1, after +3° rotation: [A] before shell exclusion and [B] after shell exclusion.

The global gamma pass rate was 91.7% when the entire target volume was included in the analysis, while after removing the outer 3 mm shell the pass rate increased to 95.1%.

The average rotational values reported in Table B.2 were then applied to patient 1 to simulate realistic setup deviations. The corresponding local gamma results are shown in Figure 5.17.

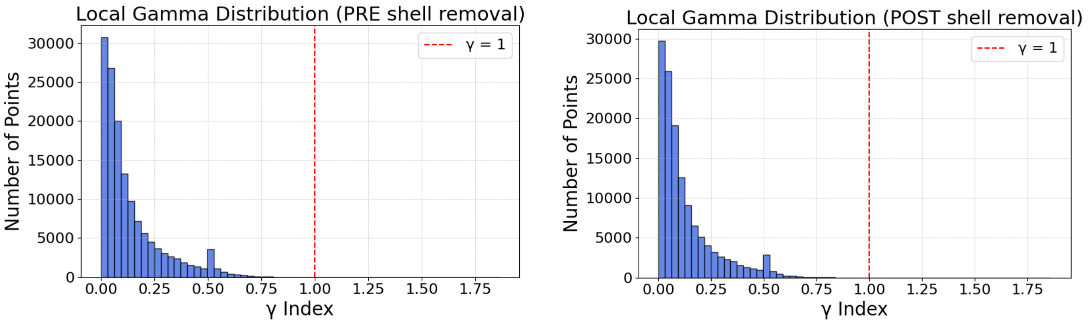

[A] *[B]*

Figure 5.17: Local gamma index distribution for patient 1, after average rotations: [A] before shell exclusion and [B] after shell exclusion.

When applying the average rotational values to patient 1, the local gamma test yielded a pass rate of 99.9%, both before and after the exclusion of the 3 mm outer shell.

Furthermore, the resulting global gamma distributions for the average rigid rotation reported in Table B.2 are shown in Figure 5.18.

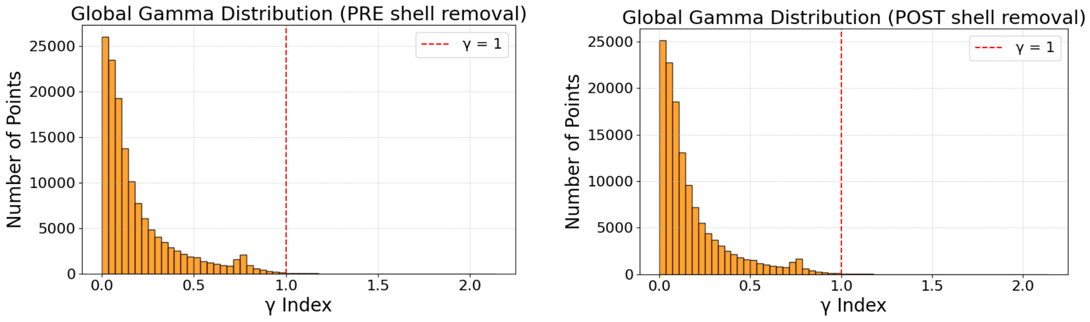

[A] *[B]*

Figure 5.18: Global gamma index distribution for patient 1, after average rotations: [A] before shell exclusion and [B] after shell exclusion.

The global gamma analysis produced a pass rate of 99.8% when considering the full target volume, which slightly increased to 99.9% after excluding the 3 mm outer shell.

The same analysis was repeated also for patient 29; in fact, also in this case a rigid rotation of +3° around all three anatomical axes was applied. The resulting local gamma distributions are showed in Figure 5.19.

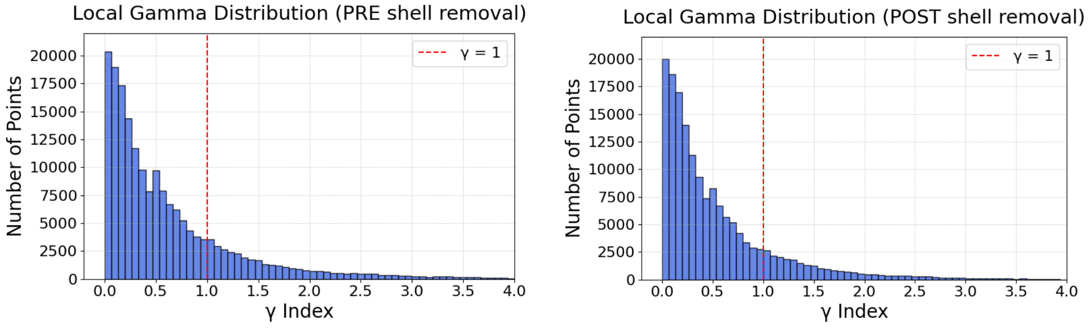

[A] *[B]*

Figure 5.19: Local gamma index distribution for patient 29, after +3° rotation: [A] before shell exclusion and [B] after shell exclusion.

In this case, when considering the full breast volume, including peripheral regions, the local gamma pass rate was 77.1%, while after the exclusion of the 3 mm outer shell, which corresponds to the outer margins of the PTV, the pass rate improved to 81.3%.

Moreover, the resulting global gamma distributions for a rigid rotation of +3° around all three anatomical axes are showed in Figure 5.20.

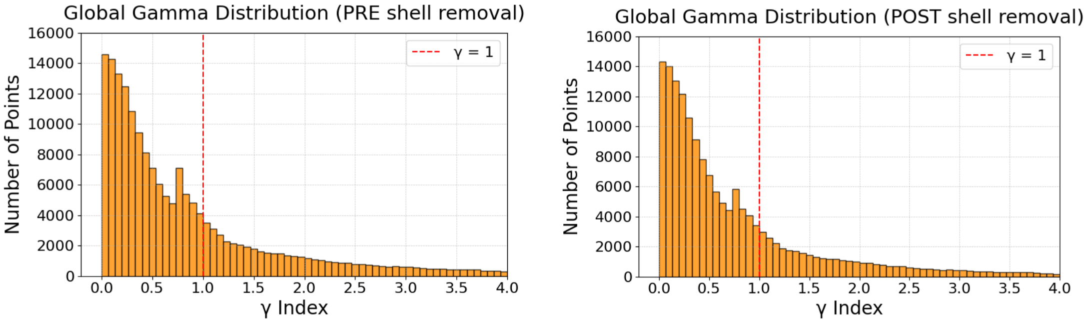

[A] [B]

Figure 5.20: Global gamma index distribution for patient 29, after +3° rotation: [A] before shell exclusion and [B] after shell exclusion.

The global gamma pass rate was 66.0% when the entire target volume was included in the analysis, while after removing the outer 3 mm shell the pass rate increased to 70.3%.

The average rotational values reported in Table B.2 were then applied to patient 29 in order to simulate realistic setup deviations. The corresponding local gamma results are shown in Figure 5.21.

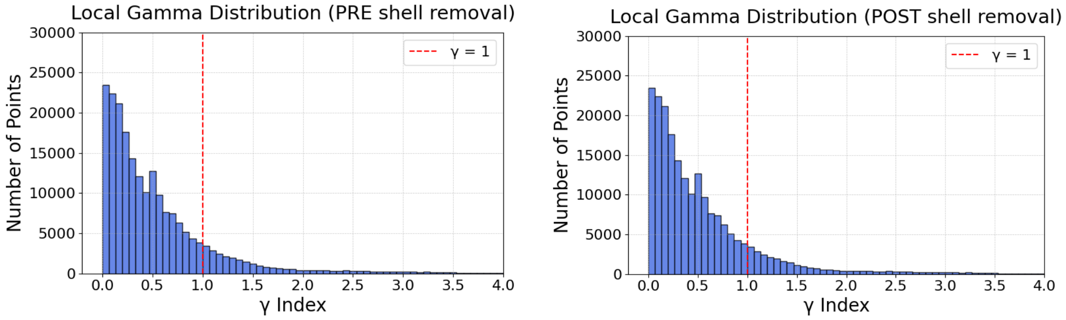

[A] [B]

Figure 5.21: Local gamma index distribution for patient 29, after average rotations: [A] before shell exclusion and [B] after shell exclusion.

When applying the average rotational values to patient 29, the local gamma test yielded a pass rate of 83.9%, which increased to 86.0% after the exclusion of the 3 mm outer shell.

Furthermore, the resulting global gamma distributions for the average rigid rotation reported in Table B.2 are shown in Figure 5.22.

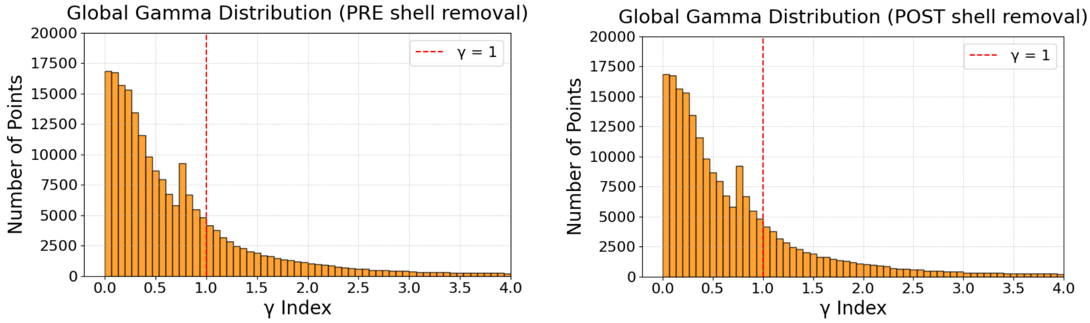

[A] *[B]*

Figure 5.22: Global gamma index distribution for patient 29, after average rotations: [A] before shell exclusion and [B] after shell exclusion.

The global gamma analysis produced a pass rate of 70.6% when considering the full target volume, which slightly increased to 74.7% after excluding the 3 mm outer shell.

5.3.2 Discussion

The results obtained in this analysis for the rotational gamma analysis reveal that even small rigid angular misalignments of the breast volume can introduce non-negligible discrepancies in the delivered dose distribution.

For patient 1, who was previously identified as a case with excellent dosimetric robustness, the application of a rigid +3° rotation around all three anatomical axes produced only modest deviations.

The local gamma pass rate remained above 96% in the full volume and exceeded 98% after excluding the outer 3 mm shell, which corresponds to the margins of the PTV. Similarly, the global gamma analysis showed high agreement, with pass rates above 91% in the entire volume and over 95% within the central target region.

These values confirm that, for selected patients, small angular uncertainties which fall within clinically acceptable thresholds are unlikely to compromise treatment quality; in fact, even when the applied rotation exceeded the typical daily setup deviations, the ob-

served dosimetric variation remained clinically tolerable.
Furthermore, when applying the average CBCT-derived rotations to the same patient, the local and global gamma pass rates were both close to 100%, confirming the negligible impact of such deviations on dose delivery in stable patients.

By contrast, patient 29 displayed a markedly different behavior; in fact, when applying a rigid rotation of +3°, the gamma pass rates dropped significantly: only 77.1% of voxels passed the local gamma test in the full target volume, and 66.0% passed the global gamma test. Even after excluding the outer shell, the pass rates remained well below the commonly accepted 90% threshold (81.3% for local gamma and 70.3% for global gamma) [57]. These results suggest that, in patients with larger anatomical shifts, angular misalignments can lead to clinically relevant deviations in dose distribution.
Moreover, when applying the average CBCT-measured rotations, which represent the realistic setup deviations observed during treatment, the gamma pass rates remained suboptimal for patient 29, with only 83.9% and 70.6% of voxels passing the local and global gamma tests, respectively, before shell exclusion. Thus, even moderate and frequent rotational residual errors can accumulate over time and degrade plan quality in sensitive cases.

In both rotation scenarios, the exclusion of the 3 mm shell consistently improved gamma pass rates, reinforcing the notion that peripheral voxels, often subject to steep dose gradients and setup uncertainties, are more susceptible to deviations.
However, while the inner target region (CTV) was relatively more stable, patient 29 still exhibited gamma pass rates below clinical acceptability even after shell removal. These results suggests that rotational errors affect not only the PTV margin, but also the core of the target volume.

To better quantify the additional dosimetric impact of residual rotational errors, Table 5.4 reports the gamma pass rates obtained from plans recalculated using the average translational shifts alone, as already discussed in subsection 5.2, and those recalculated with both translational *plus* rotational displacements derived from CBCT data. This comparison allows for the estimation of the potential dosimetric degradation that would have occurred if only surface-guided positioning had been used, without CBCT verification and correction of angular misalignments.

Patient	**Gamma Type**	**Shift Type**	**Full Volume (%)**	**No Shell (%)**
1	Local	Translation only	99.9	100
	Local	Translation + Rotation	99.9	99.9
	Global	Translation only	99.9	100
	Global	Translation + Rotation	99.8	99.9
29	Local	Translation only	84.1	86.4
	Local	Translation + Rotation	83.9	86.0
	Global	Translation only	71.9	75.0
	Global	Translation + Rotation	70.6	74.7

Table 5.4: Comparison of gamma pass rates for plans recalculated with translational shifts only versus translational plus rotational shifts.

It is important to note that the most reliable metric in Table 5.4 is the gamma pass rate obtained after exclusion of the 3 mm outer shell; in fact, this margin is removed to avoid artefactual gamma failures that occur when the rotated anatomy projects into areas that, in the original planning CT, corresponded to non-irradiated space, like the surrounding air. Since dose calculation relies on CT-defined attenuation, these regions may receive falsely high or low dose estimates in the recalculated plan, despite being clinically irradiated in the rotated configuration. Excluding the peripheral shell minimizes this artefact and allows for a more accurate dosimetric comparison.

The results in Table 5.4 confirm that the introduction of average rotational displacements leads to a measurable, though generally limited, reduction in gamma agreement compared to translational corrections alone.
In Patient 1, pass rates remained essentially unchanged, indicating a high degree of robustness to angular deviations. In contrast, Patient 29 exhibited lower baseline gamma agreement and a more marked sensitivity to rotational errors, particularly in the global gamma evaluation, which, being based on stricter criteria (3% of the maximum dose and 2 mm), was more sensitive to misalignments.
This inter-patient variability highlights the need for individualized assessment of positional robustness, as patients with complex anatomy or dose distributions near steep gradients may be more vulnerable to even small angular misalignments.
From a clinical point of view, these findings suggest that while some patients can tolerate

small angular deviations without compromising target coverage or OAR sparing, others exhibit high sensitivity, and therefore require strict geometric control.
In this context, the use of SGRT systems alone, without CBCT verification, may not always guarantee sufficient geometric accuracy. In particular, pitch and roll errors, poorly detectable by surface-only guidance, can go uncorrected and cause dose degradation [58].

5.4 Future Directions: Moving Towards Robust Treatment Planning

The findings of this work show that even small residual setup errors, both translational and rotational, can have a measurable impact on the delivered dose distribution.
While in some patients the effect is minimal, in others the degradation in target coverage and OAR sparing is clinically relevant. This variability suggests that the traditional PTV-based approach, where uncertainties are handled by adding uniform margins, may not always provide the most efficient or safest solution.

A promising approach is the adoption of robust treatment planning, as implemented in RayStation® [59]. In this framework, the treatment plan is not optimised for a single geometry, but across a set of scenarios that simulate realistic uncertainties such as small setup translational shifts, so that clinical goals are preserved even in non ideal situations.

In the context of DIBH breast treatments, robust optimisation could be used to generate scenarios that reflect the variability detected through CBCT. The optimisation across these scenarios is expected to result in more stable target volume coverage and reduced sensitivity of OAR doses to daily variations in patient positioning. The robust evaluation tools available in RayStation, which include scenario-based DVHs and voxel-wise dose maps, allow for the quantification and visualisation of this stability before the delivery of the first fraction.
From a clinical perspective, this approach may enable the development of a personalised imaging strategy. For cases where robust plan evaluation demonstrates high stability, the frequency of CBCT acquisitions could be reduced without compromising treatment quality. On the other hand, for cases showing sensitivity to geometric uncertainties, such as patient 29 in this study, robust planning could provide an additional safeguard, potentially reducing the need for daily CBCT verification, as the plan itself would be designed to maintain dose delivery within clinical limits even in the presence of larger deviations.

In the end, the transition to robust planning represents not only a technical refinement, but a change in approach, from reacting to errors after they occur to proactively designing treatments that are intrinsically resilient to anticipated uncertainties. The variability observed among patients in this study highlights the importance of implementing such a strategy.

Conclusions

This thesis investigated the clinical reliability of surface guided radiotherapy, an optical surface tracking system that reconstructs the three-dimensional surface of the patient in real time using optical imaging without the need for external markers such as tattoos or the use of ionizing radiations, for left-sided breast cancer treated in deep inspiration breath hold. The focus was on the geometric accuracy of Sentinel® system, which is a surface imaging device designed to be used in the radiotherapy workflows, in particular during the phase of the planning computed tomography scan. Moreover, residual positioning errors after surface guided radiotherapy were quantified from cone beam computed tomography based corrections, and the dosimetric impact of realistic translational and rotational uncertainties was assessed using dose–volume histograms and a comprehensive 3D gamma analysis.

In particular, the vertical elevation measured by tracking the primary gating point with the Sentinel® system, and the anatomical elevation occurring between the free breathing and breath hold conditions visualized on computed tomography scans, were compared. The term “elevation of the primary gating point”, stands for the difference in the elevation of the thoracic area of the patient between the free breathing and breath hold respiratory conditions. The computed tomography elevation (13.2 ±4.0 mm) closely matched the one registered by the Sentinel® system (12.8 ±3.5 mm), with no significant difference (Wilcoxon signed-rank test, p-value $= 0.8398$). This finding validates the Sentinel® system as a reliable surrogate for vertical chest–wall motion during deep inspiration breath hold when the primary gating point, which is a surface tracking point, is placed correctly. Moreover, when Pearson’s correlations were computed for the differences in elevation between free breathing and breath hold phases, a strong coupling was observed between the primary gating point and the left nipple (p-value < 0.0001), a weaker yet significant association with the abdomen (p-value $= 0.0427$), and no significant nipple–abdomen correlation (p-value = 0.1153). Overall, thoracic landmarks are the most reliable motion surrogates for surface guided radiotherapy, thus it is necessary to place the primary gating point, at a reproducible thoracic site, ideally near the xiphoid process, which is the cartilaginous section at the lower end of the sternum not attached to any ribs. The primary gating point is a tracking point selected by the radiation technologist on the surface of the anterior thoracic wall of the patient in order to evaluate the vertical elevation of the location at which it is placed during the breathing cycle.

Residual positioning errors were assessed from 475 post cone beam computed tomography couch corrections (six degrees of freedom) recorded after the initial surface guided radiotherapy alignment. Translational residuals were centered near zero, with the largest spread along the longitudinal (Y) axis and a positive skew in the vertical (Z) axis, indicating frequent upward corrections. The resulting 3D shift typically clustered around 6-7 mm. The systematic error (Σ) and random error (σ) were within clinically manageable ranges but were not negligible (for the 15 treatment fractions group: $\Sigma_{\text{X,Y,Z}} \approx (2.6,\ 3.9,\ 3.3)$ mm and $\sigma_{\text{X,Y,Z}} \approx (2.0,\ 2.5,\ 2.3)$ mm).
Furthermore, rigid simulations of ±3° rotations around the isocenter of the treatment demonstrated geometry amplification with breast size; in fact the farthest surface point of the ROI of the left breast was shifted by $\sim$6.5mm in the small breast volume, and up to $\sim$11mm in the large breast volume. Pearson correlation demonstrated that the 3D shift correlated strongly with breast volume (p-value < 0.0001). Even small rotations within common clinical tolerances can therefore produce relevant positional deviations in large or irregular breasts, particularly away from isocenter.

On 22 evaluable treatment plans of patients treated with the 15 fractions regimen, the recalculation performed with patient–specific average isocenter shifts preserved D_{90} ($\geq$90% of the prescribed dose) for all patients and D_{95} for 21 out of 22 patients. D_{90} and D_{95} refer to the the minimum dose received by the 90% and 95% of the target volume.
However, the minimum ipsilateral dose, which is a pointwise (single-voxel) metric, dropped below 25Gy in 7 out of 22 patients, and contralateral breast and LAD maxima exceeded local limits in a subset of patients. Wilcoxon tests showed significant changes for most metrics (D_{90}, D_{95}, ipsilateral minimum dose, contralateral maximum and LAD maximum dose), while heart mean dose remained statistically unchanged between the original and the recalculated treatment plan. It is important to note that, in a subset of 10 patients with no threshold violations, none of the evaluated dosimetric parameters changed significantly, indicating that plan robustness is highly patient-dependent.

A 3D gamma evaluation of the recalculated treatment plan was performed using stringent criteria (local 5%/3 mm and global 3%/2 mm) within the target breast, both including and excluding a 3 mm peripheral shell in order to focus the analysis on the clinical target volume rather than the full planning target volume.

Two representative patient cases, one selected due to its excellent agreement between the original and recalculated dose distributions, and the other chosen because of the large isocenter shift applied to her treatment plan, illustrate the spectrum of responses. Patient 1, characterized by small isocenter shifts, showed near-perfect agreement: after shell exclusion, local and global pass rates were 100%, and dose volume histograms differed only marginally from the original plan. By contrast, patient 29, with larger shifts, exhibited lower agreement, and clinically relevant dose-volume histogram degradations (D_{95}, one of the most important metrics to quantify target coverage, decreased by 14.6%). When average rotations were added to the translational offsets, the gamma pass rate of patient 1 changed negligibly, while the one of patient 29 showed a small additional reduction, reinforcing the non negligible role of rotations in less robust geometries.

Overall, the results support surface guided radiotherapy as an accurate and efficient workflow for left–sided breast radiotherapy in deep inspiration breath hold.
However, the geometric accuracy of the Sentinel® system depends strongly on correct primary gating-point placement and consistent coaching. Translational residuals of a few millimetres are common and usually tolerable, but their dosimetric impact is heterogeneous across patients and planning techniques, and even small rotations can cause large peripheral shifts in large breasts. In this context, a subset of patients cannot be safely managed with surface guided radiotherapy alone, and cone beam computed tomography verification remains necessary to ensure optimal target coverage, while for other patients, after early verification, routine cone beam computed tomography may no longer be required.

A practical way forward is to combine surface guided radiotherapy with cone beam computed tomography in the first treatment fractions, quantify the average translational and rotational corrections, and re-assess plan robustness with dose–volume histograms and three-dimensional gamma analysis as done in this work.
Patients at higher geometric risk, such as those with large breast volume, steep dose gradients, or larger three-dimensional shifts, should continue with daily cone beam computed tomography. In the future, a robust approach in which the plan is optimised across

scenarios built from the translational and rotational variations measured with cone beam imaging can be added, so that target coverage and the dose to organs at risk stay stable even when the patient's setup shows small variations compared with the planning scan. In this way, the focus moves from correcting problems after they appear to designing treatments that are resilient from the beginning.

In summary, surface guided radiotherapy, along with Sentinel® and Catalyst® systems enable accurate and non–ionising positioning for deep inspiration breath hold breast treatments. However, clinically relevant geometric and dosimetric variability persist between patients; a patient–specific strategy that combines early cone beam computed tomography verification, quantitative robustness checks with dose–volume histograms and three-dimensional gamma analysis, and robust optimisation provides a path to safer and more personalised breast radiotherapy.

Appendix A

Table A.1: Measured vertical displacements and respiratory parameters derived from CT and Sentinel® system across all patients.

Patient	30 mm Sphere [mm]	16 mm Sphere [mm]	Baseline (pre-CT) [mm]	Mean Ampl. during CT [mm]	Sentinel Elevation [mm]	CT Elevation [mm]
1	14.1	12.2	100.2	113.4	13.2	11.6
2	9.2	10.3	109.3	115.9	6.6	8.1
3	13.5	13.3	120.5	133.8	13.3	11.4
4	26.2	24.2	124.5	143.8	19.3	20.1
5	9.7	9.6	118.1	127.1	9.0	9.3
6	30.0	29.2	128.0	141.5	13.5	21.0
7	16.5	17.1	134.5	148.0	13.5	9.9
8	13.0	13.2	105.0	117.5	12.5	11.6
9	21.3	21.2	139.4	158.3	18.9	16.6
10	9.9	9.8	132.4	142.4	10.0	9.7
11	20.3	20.8	125.8	139.0	13.2	13.6
12	15.3	13.8	106.4	118.5	12.1	10.9
13	29.4	29.9	114.7	131.9	17.2	18.4
14	21.1	21.5	132.6	147.1	14.5	15.9
15	11.5	10.0	127.0	140.4	13.4	10.6
16	18.7	17.9	110.5	124.5	14.0	15.0
17	15.6	8.5	144.0	154.7	10.7	10.5
18	13.4	14.5	125.5	134.6	9.1	9.8
19	10.6	10.7	127.5	135.4	7.9	9.0
20	17.9	19.2	115.8	126.9	11.1	13.3
21	10.2	9.5	159.6	172.7	13.1	9.9
22	16.3	17.0	117.6	131.1	13.5	11.8
23	8.6	18.7	150.6	161.6	11.0	18.9
24	17.5	17.8	121.6	134.5	12.9	12.7

Continued on next page

Patient	30 mm Sphere [mm]	16 mm Sphere [mm]	Baseline (pre-CT) [mm]	Mean Ampl. during CT [mm]	Sentinel Elevation [mm]	CT Elevation [mm]
25	23.8	22.9	136.5	150.2	13.7	14.5
26	10.3	10.4	93.4	103.3	9.9	9.6
27	32.5	33.4	188.2	210.7	22.5	22.7
28	13.0	13.0	179.6	189.2	9.6	8.2
29	17.5	18.2	112.3	124.4	12.1	14.0
30	24.3	23.6	121.7	137.1	15.4	18.5
31	24.3	24.9	107.2	119.6	12.4	18.6
32	10.4	10.5	86.4	96.2	9.8	8.8
33	13.0	12.5	201.5	218.0	16.5	11.1
34	15.1	14.3	158.2	173.1	14.9	13.3
35	13.9	14.6	159.9	166.2	6.3	11.6

Table A.2: Number of fractions, age, regression parameters and estimated physiological heartbeat for each patient.

Patient	Fractions	Age	Slope of Fit	Intercept [mm]	R^2	Heartbeat
1	15	34	-0.14	114.0	0.77	64
2	15	63	-0.03	116.2	0.36	70
3	15	37	-0.13	134.7	0.91	61
4	15	45	0.01	143.7	0.03	69
5	15	47	-0.08	127.8	0.68	69
6	15	67	-0.02	141.8	0.14	59
7	15	52	-0.13	148.8	0.54	82
8	5	62	0.09	116.9	0.57	67
9	15	67	-0.11	159.2	0.73	73
10	15	56	-0.14	143.4	0.71	72

Continued on next page

Patient	Fractions	Age	Slope of Fit	Intercept [mm]	R^2	Heartbeat
11	15	57	-0.11	139.7	0.54	97
12	15	48	-0.08	119.2	0.59	73
13	15	50	-0.08	132.6	0.60	79
14	15	55	-0.03	147.4	0.41	108
15	15	47	-0.06	140.9	0.25	69
16	5	65	-0.19	126.4	0.68	66
17	15	54	-0.21	156.1	0.87	78
18	15	51	-0.04	134.9	0.55	71
19	5	63	-0.10	136.2	0.64	77
20	15	51	-0.11	127.9	0.70	74
21	15	55	-0.02	172.9	0.03	54
22	15	50	-0.01	131.1	0.01	46
23	15	61	-0.07	162.3	0.58	64
24	15	45	-0.05	134.9	0.51	64
25	15	65	-0.18	151.3	0.89	71
26	15	59	-0.04	103.6	0.27	92
27	15	59	0.06	210.3	0.09	76
28	5	77	0.04	189.0	0.31	68
29	15	44	-0.18	125.7	0.94	60
30	15	50	-0.05	137.6	0.52	68
31	15	49	-0.05	120.1	0.27	73
32	5	62	-0.04	96.5	0.30	76
33	15	72	-0.05	218.5	0.10	86
34	15	46	-0.05	173.5	0.32	67
35	15	65	0.07	165.8	0.24	74

Table A.3: Individual patient values for breast, xiphoid, and abdominal elevation, and assigned breathing type. A = abdominal, T = thoracic.

Patient	**Breast Elevation [mm]**	**Xiphoid Elevation [mm]**	**Abdomen Elevation [mm]**	**Breathing Type**
1	13.4	14.2	20.7	A
2	9.0	12.3	10.8	T
3	13.1	17.6	12.8	T
4	27.1	26.5	17.5	T
5	9.5	11.2	11.6	A
6	29.9	29.0	26.7	T
7	16.5	15.5	20.2	A
8	13.0	11.3	14.3	A
9	21.0	23.6	33.2	A
10	10.1	7.5	18.8	A
11	21.5	17.4	17.2	T
12	14.6	15.5	21.3	A
13	30.1	23.1	22.6	T
14	22.5	28.2	27.7	A
15	11.5	17.0	24.6	A
16	18.8	16.2	14.3	T
17	15.3	14.9	12.9	T
18	12.9	13.2	13.2	A
19	10.6	11.2	19.7	A
20	18.3	18.7	20.1	A
21	9.9	11.3	29.6	A
22	16.6	22.6	9.1	T
23	17.8	13.3	19.0	A
24	17.4	19.8	21.5	A
25	22.1	16.0	27.2	A
26	10.5	18.3	13.9	T
27	32.7	37.5	10.1	T
28	12.1	7.3	21.8	A

Continued on next page

Patient	Breast Elevation [mm]	Xiphoid Elevation [mm]	Abdomen Elevation [mm]	Breathing Type
29	17.7	10.5	14.2	T
30	23.5	27.4	29.3	A
31	23.7	22.7	26.7	A
32	10.5	12.6	7.0	T
33	13.2	23.6	20.3	A
34	14.1	20.2	29.9	A
35	14.6	16.2	12.3	T

Appendix B

Table B.1: Mean and standard deviation of residual setup errors per patient, expressed along the lateral (X), longitudinal (Y), and vertical (Z) axes. The 3D shift is calculated as the Euclidean distance from the ideal isocenter position.

Patient	**X - Lateral Mean ± SD [mm]**	**Y - Longitudinal Mean ± SD [mm]**	**Z - Vertical Mean ± SD [mm]**	**3D Shift Mean ± SD [mm]**
1	−0.7 ± 2.2	1.4 ± 1.4	0.9 ± 2.6	3.5 ± 2.0
2	−1.3 ± 1.7	−1.4 ± 1.6	1.6 ± 2.8	3.9 ± 1.8
3	3.7 ± 1.5	−4.7 ± 2.5	−1.1 ± 1.6	6.6 ± 2.2
4	1.3 ± 1.4	−4.0 ± 5.9	−0.2 ± 4.5	7.1 ± 4.5
5	0.1 ± 1.6	−0.7 ± 1.7	2.9 ± 2.6	3.5 ± 2.9
6	−0.1 ± 3.2	6.5 ± 2.3	10.3 ± 2.4	12.7 ± 2.8
7	1.7 ± 1.9	0.4 ± 3.7	2.3 ± 3.0	4.7 ± 3.3
8	−2.4 ± 1.8	−4.0 ± 1.4	1.2 ± 0.8	5.2 ± 1.3
9	−1.7 ± 1.5	5.7 ± 1.9	0.4 ± 1.2	6.2 ± 2.1
10	−1.7 ± 1.8	2.1 ± 2.1	−1.3 ± 1.9	4.0 ± 2.0
11	−0.6 ± 2.0	5.3 ± 2.7	3.1 ± 2.3	6.8 ± 2.7
12	2.8 ± 1.3	−4.3 ± 1.6	−0.3 ± 2.0	5.6 ± 1.6
13	0.1 ± 1.3	5.4 ± 1.6	3.9 ± 2.0	7.1 ± 1.7
14	1.9 ± 2.1	−0.1 ± 3.3	5.1 ± 2.4	6.5 ± 2.5
15	4.9 ± 1.9	2.6 ± 3.3	−2.1 ± 3.9	7.4 ± 3.1
16	3.0 ± 1.0	7.6 ± 5.6	10.6 ± 5.5	14.0 ± 6.4
17	−4.7 ± 2.9	0.8 ± 1.7	5.6 ± 1.7	8.0 ± 2.1
18	1.3 ± 2.0	3.5 ± 2.6	1.7 ± 2.0	5.1 ± 2.0
19	1.6 ± 1.7	−2.0 ± 2.6	2.6 ± 2.3	4.6 ± 2.2
20	0.5 ± 1.3	−6.8 ± 2.2	−1.4 ± 1.8	7.3 ± 2.2
21	−1.7 ± 2.3	1.4 ± 2.5	3.5 ± 2.2	5.4 ± 2.2
22	−0.2 ± 2.5	−1.4 ± 2.7	−0.9 ± 2.1	4.2 ± 1.3
23	0.3 ± 2.3	−0.7 ± 2.0	0.7 ± 1.5	2.9 ± 1.8

Continued on next page

Patient	X - Lateral Mean ± SD [mm]	Y - Longitudinal Mean ± SD [mm]	Z - Vertical Mean ± SD [mm]	3D Shift Mean ± SD [mm]
24	−3.8 ± 1.9	0.1 ± 3.9	5.9 ± 3.5	8.3 ± 3.0
25	−1.5 ± 2.0	2.8 ± 1.2	2.4 ± 0.8	4.5 ± 1.2
26	1.7 ± 1.4	1.0 ± 1.3	2.6 ± 1.3	3.7 ± 1.4
27	0.5 ± 2.8	1.5 ± 2.0	4.1 ± 1.5	5.5 ± 1.4
28	−1.8 ± 0.8	−3.2 ± 3.1	−0.4 ± 2.1	4.8 ± 1.6
29	0.0 ± 3.0	−9.1 ± 2.6	−5.7 ± 2.5	11.5 ± 2.3
30	0.3 ± 1.4	−0.4 ± 2.0	4.9 ± 1.8	5.5 ± 1.7
31	3.4 ± 2.0	8.5 ± 3.1	8.1 ± 2.7	12.6 ± 3.6
32	−0.6 ± 1.1	−0.4 ± 2.4	0.4 ± 1.5	3.8 ± 1.3
33	7.9 ± 4.0	−4.3 ± 6.7	−1.7 ± 4.5	11.9 ± 4.2
34	1.1 ± 1.3	−0.7 ± 1.2	1.5 ± 1.5	2.8 ± 1.0
35	−3.2 ± 1.6	1.3 ± 1.4	−0.2 ± 1.4	4.0 ± 1.4

Table B.2: Mean and standard deviation of residual rotational errors (Pitch, Roll, Yaw) and breast volume for each patient. Rotational values are expressed in degrees [°], volume in milliliters [mL].

Patient	Pitch Mean ± SD [°]	Roll Mean ± SD [°]	Yaw Mean ± SD [°]	Breast Volume [mL]
1	−0.6 ± 0.9	0.8 ± 0.7	1.1 ± 0.7	532
2	−1.6 ± 0.7	0.1 ± 0.6	1.0 ± 1.0	297
3	0.3 ± 0.9	−1.9 ± 0.6	1.0 ± 1.0	379
4	−2.1 ± 0.9	−0.4 ± 0.7	−0.1 ± 0.8	75
5	−1.7 ± 0.7	−0.6 ± 1.1	0.9 ± 0.9	546
6	−0.4 ± 0.7	−0.1 ± 0.8	0.3 ± 1.0	518
7	−1.8 ± 0.6	−1.2 ± 0.6	−1.6 ± 0.7	841
8	−0.5 ± 1.0	−0.7 ± 0.5	1.2 ± 0.6	566

Continued on next page

Patient	**Pitch** **Mean ± SD [°]**	**Roll** **Mean ± SD [°]**	**Yaw** **Mean ± SD [°]**	**Breast Volume** **[mL]**
9	0.1 ± 0.8	−0.4 ± 0.7	−1.5 ± 0.7	859
10	−2.0 ± 0.6	−1.3 ± 0.8	0.1 ± 1.1	496
11	−2.0 ± 0.8	−0.5 ± 0.9	0.5 ± 0.9	822
12	−0.1 ± 0.6	0.3 ± 0.5	−0.1 ± 0.9	294
13	0.5 ± 1.0	−0.5 ± 0.8	0.4 ± 0.8	176
14	−2.5 ± 0.3	−0.8 ± 0.9	0.5 ± 1.0	368
15	0.4 ± 1.0	0.9 ± 1.1	−2.1 ± 0.8	859
16	−2.0 ± 0.6	1.1 ± 1.3	1.0 ± 0.7	446
17	−1.6 ± 0.8	−1.7 ± 0.6	−1.3 ± 0.9	2260
18	−0.8 ± 0.7	−0.6 ± 0.6	−1.8 ± 0.7	654
19	−0.6 ± 1.1	−0.6 ± 0.4	−1.2 ± 1.4	1331
20	−2.4 ± 0.6	−1.6 ± 0.9	1.0 ± 0.8	321
21	−1.6 ± 0.7	−1.8 ± 0.6	−1.3 ± 0.7	540
22	0.1 ± 1.2	−0.3 ± 0.8	−1.1 ± 1.2	385
23	−1.6 ± 0.8	−1.2 ± 1.0	1.8 ± 0.6	1132
24	−1.6 ± 1.0	−0.6 ± 0.7	0.0 ± 1.4	226
25	−1.2 ± 1.0	−1.2 ± 0.6	−0.9 ± 0.7	823
26	−1.0 ± 0.5	−0.6 ± 0.5	−1.7 ± 0.9	290
27	−0.3 ± 1.0	0.0 ± 1.0	1.5 ± 0.7	520
28	0.1 ± 0.6	−0.7 ± 1.3	0.4 ± 1.2	717
29	−0.6 ± 1.0	0.8 ± 0.8	1.0 ± 0.9	760
30	−0.9 ± 0.7	−0.1 ± 0.6	0.9 ± 1.0	661
31	−1.1 ± 1.4	−1.3 ± 0.8	−0.1 ± 1.4	228
32	−0.5 ± 0.8	1.0 ± 0.3	1.2 ± 1.2	534
33	−1.6 ± 0.9	−1.7 ± 0.6	1.5 ± 1.2	1042
34	−1.3 ± 0.8	−0.6 ± 0.9	1.0 ± 1.1	1329
35	−1.7 ± 0.7	−0.6 ± 1.1	0.9 ± 0.9	351

Appendix C

Table C.1: Dosimetric values (in Gy) from the original approved treatment plan for each patient included in the analysis, selected based on criterion of a minimum dose to the contralateral breast greater than 25 Gy.

Patient	**D90 [Gy]**	**D95 [Gy]**	**Dmin Ipsilateral [Gy]**	**Heart D_{max} [Gy]**	**Contralateral Breast D_{max} [Gy]**	**LAD D_{max} [Gy]**
1	40.1	39.5	33.1	13.1	2.8	11.5
2	40.5	40.2	33.3	15.9	2.4	5.5
3	40.3	39.9	34.3	4.8	3.2	4.1
4	40.1	39.7	34.0	2.4	3.6	2.3
5	40.4	40.0	29.4	13.8	4.2	11.3
6	40.6	40.0	32.0	5.0	2.0	3.4
7	40.0	39.5	31.4	2.4	4.7	2.4
12	40.5	39.8	34.1	2.8	3.3	2.6
14	40.1	39.5	33.4	2.1	3.1	1.9
15	40.3	39.7	28.8	2.1	1.7	1.9
18	40.2	39.6	25.1	3.0	7.0	2.4
20	40.4	39.8	34.3	9.2	1.8	9.0
22	40.4	39.7	31.5	5.9	3.8	4.0
23	40.1	39.5	29.3	7.6	5.1	6.3
24	40.6	40.1	30.4	5.0	1.6	4.1
25	40.3	39.8	28.6	18.6	2.4	18.6
26	39.3	38.5	33.9	8.8	3.0	5.2
27	40.0	39.4	30.8	5.5	3.7	4.4
29	40.6	39.8	27.8	18.0	2.5	18.4
31	40.2	39.8	35.6	3.9	2.4	3.6
33	39.4	38.9	32.5	0.9	0.5	0.4
35	40.0	39.8	36.4	11.7	1.8	10.1

Table C.2: Dosimetric values (in Gy) obtained from recalculated plans in which the average translational errors, derived from CBCT acquisitions, were applied to the isocenter. These values allow the evaluation of the potential dosimetric impact of uncorrected setup errors in the absence of daily volumetric imaging.

Patient	**D90 [Gy]**	**D95 [Gy]**	**Dmin Ipsilateral [Gy]**	**Heart D_{max} [Gy]**	**Contralateral Breast D_{max} [Gy]**	**LAD D_{max} [Gy]**
1	40.1	39.5	32.4	12.8	2.8	11.4
2	40.5	40.1	34.5	18.7	3.2	6.1
3	38.9	39.1	31.2	5.0	5.7	4.4
4	39.8	38.8	29.5	2.6	6.1	2.6
5	40.3	39.9	35.8	20.9	7.3	18.4
6	39.9	38.4	17.9	6.1	5.7	5.7
7	39.9	39.3	31.8	2.8	9.7	2.7
12	40.1	39.3	33.5	3.6	5.8	3.0
14	38.9	37.9	29.1	2.9	4.3	2.7
15	40.1	39.4	27.9	2.1	1.6	1.9
18	40.0	39.2	21.9	3.3	8.3	2.6
20	40.2	39.5	24.5	11.4	2.7	11.0
22	40.3	39.7	30.6	5.5	3.0	3.9
23	40.1	39.5	31.9	8.0	5.3	6.8
24	40.3	38.6	32.1	6.7	3.7	5.6
25	40.3	39.9	29.3	19.0	3.2	18.6
26	39.8	38.9	33.8	18.5	4.6	8.7
27	39.5	38.6	23.4	7.8	7.2	6.1
29	38.5	34.4	6.1	13.2	2.0	13.0
31	40.9	40.6	14.5	4.6	3.4	4.1
33	39.8	39.2	12.4	0.8	0.5	0.4
35	39.9	39.5	29.6	9.9	1.7	9.2

Table C.3: Percentage differences between the original treatment plans and the recalculated plans with average translational shifts applied to the isocenter.
Values are expressed as relative changes (%) in key dosimetric parameters. Positive values indicate an increase in the recalculated plan.

Patient	**D90 [%]**	**D95 [%]**	**Dmin Ipsilateral [%]**	**Heart D_{max} [%]**	**Contralateral Breast D_{max} [%]**	**LAD D_{max} [%]**
1	0	0.1	-2.2	-2.4	0	-1.2
2	-0.2	-0.4	3.5	17.6	33.2	9.8
3	-3.6	-1.9	-9.0	5.2	75.3	7.1
4	-0.9	-2.3	-13.2	11.9	70.5	13.2
5	-0.4	-0.2	21.5	51.7	72.2	62.8
6	-1.7	-4.0	-44.1	22.5	189.3	68.5
7	-0.3	-0.4	1.2	18.2	106.6	14.9
12	-1.1	-1.2	-1.7	31.2	73.1	16.9
14	-2.8	-3.9	-12.8	41.6	41.0	39.1
15	-0.5	-0.8	-3.1	2.4	-6.9	-0.5
18	-0.6	-1.0	-12.4	10.0	19.9	7.5
20	-0.3	-0.7	-28.5	23.8	56.0	22.3
22	-0.1	-0.1	-3.1	-6.1	-19.4	-2.7
23	0.1	0.1	9.0	6.4	4.5	7.1
24	-0.6	-3.8	5.6	32.9	129.8	35.6
25	0.1	0.2	2.4	2.1	29.9	0.4
26	1.1	0.9	-0.3	111.2	56.6	67.8
27	-1.2	-2.2	-24.0	42.3	92.7	39.7
29	-5.4	-13.5	-78.1	-26.9	-18.6	-29.1
31	1.9	2.0	-59.1	19.0	45.1	15.5
33	0.9	0.8	-61.7	-9.4	-8.2	-2.4
35	-0.4	-0.6	-18.6	-15.6	-8.3	-8.7

Acknowledgement

I would like to thank the Istituto Scientifico Romagnolo per lo Studio e la Cura dei Tumori “Dino Amadori” – IRCCS (IRST) in Meldola, and in particular Dr. Anna Sarnelli, for the opportunity to carry out my thesis work at their institute. This experience has greatly contributed to both my academic growth and personal development, and I am sincerely grateful for their support.

I am sincerely grateful to Dr. Roberto Spighi for his valuable advice and guidance during the writing of this thesis. Beyond his scientific support, I truly appreciated his kindness and availability, and I feel fortunate to have had him as my supervisor both during my bachelor’s and master’s degree.

Finally, I would like to thank Dr. Giacomo Feliciani for accompanying me through every step of my journey at the Istituto Scientifico Romagnolo per lo Studio e la Cura dei Tumori “Dino Amadori” – IRCCS (IRST), from the very first day to the last. His guidance and constant support have been invaluable, and I am truly grateful for his presence throughout this experience.

References

[1] Dominik Soliman. “Augmented microscopy: Development and application of high-resolution optoacoustic and multimodal imaging techniques for label-free biological observation”. PhD thesis. Oct. 2016. DOI: `10.13140/RG.2.2.24410.03525`.

[2] Maria Pia Morigi. *Lecture Notes for Health Physics*. Course material. Università di Bologna. 2023.

[3] O. Klein and Y. Nishina. *Über die Streuung von Strahlung durch freie Elektronen nach der neuen relativistischen Quantendynamik von Dirac*. In: *Zeitschrift für Physik* 52 (1929), pp. 853–868. DOI: `10.1007/BF01366453`.

[4] Istituto Nazionale di Fisica Nucleare. *Radiation Detection — INFN Ferrara Educational*. 2024. URL: `https://www.fe.infn.it/radioactivity/educational/detection.html`.

[5] Bongile Mzenda, M. E. Hosseini-Ashrafi, and A. Palmert. *Determination of target volumes in radiotherapy and the implications of technological advances: a literature review*. In: *Journal of Radiotherapy in Practice* 8.1 (2009), pp. 41–51.

[6] Council of the European Union. *Council Directive 2013/59/Euratom of 5 December 2013 laying down basic safety standards for protection against the dangers arising from exposure to ionising radiation*. Official Journal of the European Union, L13, 17 January 2014. 2014. URL: `http://www.ac.infn.it/sicurezza/DirEur_GU170114.pdf`.

[7] L. Pray. *Discovery of DNA structure and function: Watson and Crick*. In: *Nature Education* 1.1 (2008), p. 100. URL: `https://www.nature.com/scitable/topicpage/discovery-of-dna-structure-and-function-watson-397`.

[8] Roberto Spighi. *Lecture Notes for Applications of Nuclear Physics*. Course material. Università di Bologna. 2023.

[9] Kathy L. Baglan et al. *Accelerated partial breast irradiation using 3D conformal radiation therapy (3D-CRT)*. In: *International Journal of Radiation Oncology* 55.2 (2003), pp. 302–311. DOI: `10.1016/S0360-3016(02)03811-7`.

[10] C. X. Yu et al. *Clinical implementation of intensity-modulated arc therapy*. In: *International Journal of Radiation Oncology, Biology, Physics* 53.2 (2002), pp. 453–463.

[11] J.J. Qiu et al. *Impact of volumetric modulated arc therapy technique on treatment with partial breast irradiation*. In: *International Journal of Radiation Oncology, Biology, Physics* 78 (2010), pp. 288–296. DOI: `10.1016/j.ijrobp.2009.07.1702`.

[12] M. Teoh et al. *Volumetric modulated arc therapy: a review of current literature and clinical use in practice*. In: *British Journal of Radiology* 84.1007 (2011), pp. 967–996. DOI: `10.1259/bjr/22373346`.

[13] Cyril Voyant et al. *Hybrid VMAT-3DCRT as breast cancer treatment improvement tool*. In: *Scientific Reports* 13 (2023), p. 23110. DOI: `10.1038/s41598-023-50538-x`.

[14] Associazione Italiana di Oncologia Medica (AIOM), Associazione Italiana Registri Tumori (AIRTUM), and Società Italiana di Anatomia Patologica e Citologia Diagnostica (SIAPEC-IAP). *I numeri del cancro in Italia 2024*. Available at: `https://www.aiom.it/wp-content/uploads/2024/06/2024_NDC_web-def.pdf`. Milano, Roma, Brescia: AIOM, AIRTUM, SIAPEC-IAP, PASSI, Ministero della Salute, 2024.

[15] Wesley Naidoo and Michelle Leech. *Feasibility of surface guided radiotherapy for patient positioning in breast radiotherapy versus conventional tattoo-based setups: a systematic review*. In: *Technical Innovations & Patient Support in Radiation Oncology* 22 (2022), pp. 39–49. DOI: `10.1016/j.tipsro.2022.03.001`.

[16] Aaron M. Laine et al. *The Role of Hypofractionated Radiation Therapy with Photons, Protons, and Heavy Ions for Treating Extracranial Lesions*. In: *Frontiers in Oncology* 5 (2016), p. 302. DOI: `10.3389/fonc.2015.00302`.

[17] Corinne Townend et al. *A review of permanent marking for radiotherapy in the UK*. In: *Radiography* 26.1 (2020), pp. 9–14. DOI: `10.1016/j.radi.2019.08.003`.

[18] Malin Kügele et al. *Surface guided radiotherapy (SGRT) improves breast cancer patient setup accuracy*. In: *Journal of Applied Clinical Medical Physics* 20.9 (2019), pp. 61–68. DOI: `10.1002/acm2.12700`.

[19] Heidi Probst et al. *A systematic review of methods to immobilise breast tissue during adjuvant breast irradiation*. In: *Radiography* 20.1 (2014), pp. 70–81. DOI: `10.1016/j.radi.2013.10.002`.

[20] Carmen Bergom et al. *Deep Inspiration Breath Hold: Techniques and Advantages for Cardiac Sparing During Breast Cancer Irradiation*. In: *Frontiers in Oncology* Volume 8 - 2018 (2018). DOI: `10.3389/fonc.2018.00087`.

[21] G. R. Borst et al. *Clinical results of image-guided deep inspiration breath hold breast irradiation*. In: *International Journal of Radiation Oncology* 78 (2010), pp. 1345–1351. DOI: `10.1016/j.ijrobp.2009.10.006`.

[22] H. Y. Lee et al. *The deep inspiration breath hold technique using Abches reduces cardiac dose in patients undergoing left-sided breast irradiation*. In: *Radiation Oncology Journal* 31 (2013), pp. 239–246. DOI: `10.3857/roj.2013.31.4.239`.

[23] N. Rochet et al. *Deep inspiration breath-hold technique in left-sided breast cancer radiation therapy: evaluating cardiac contact distance as a predictor of cardiac exposure for patient selection*. In: *Practical Radiation Oncology* 5 (2015), e127–e134. DOI: `10.1016/j.prro.2014.08.003`.

[24] Hania A. Al-Hallaq et al. *AAPM Task Group Report 302: Surface-Guided Radiotherapy*. In: *Medical Physics* 49.4 (2022), e82–e112. DOI: `10.1002/mp.15532`.

[25] Philipp Freislederer et al. *ESTRO-ACROP guideline on surface guided radiation therapy*. In: *Radiotherapy and Oncology* 173 (2022), pp. 188–196. DOI: `10.1016/j.radonc.2022.05.026`.

[26] Michalis Mazonakis and John Damilakis. *Computed tomography: What and how does it measure?* In: *European Journal of Radiology* 85.8 (2016), pp. 1499–1504. ISSN: 0720-048X. DOI: `https://doi.org/10.1016/j.ejrad.2016.03.002`.

[27] Stephanie Schönecker et al. *Treatment planning and evaluation of gated radiotherapy in left-sided breast cancer patients using the Catalyst™/Sentinel™ system for deep inspiration breath-hold (DIBH)*. In: *Radiation Oncology* 11.1 (2016). Published 26 October 2016, p. 143. DOI: `10.1186/s13014-016-0716-5`.

[28] Christian Heinz et al. *Technical evaluation of different respiratory monitoring systems used for 4D CT acquisition under free breathing*. In: *Journal of Applied Clinical Medical Physics* 16 (Mar. 2015), pp. 334–349. DOI: `10.1120/jacmp.v16i2.4917`.

[29] Daniel Reitz et al. *Stability and reproducibility of 6013 deep inspiration breath-holds in left-sided breast cancer*. In: *Radiation Oncology* 15.1 (2020). Published May 24, 2020, p. 121. DOI: `10.1186/s13014-020-01572-w`.

[30] C-RAD Positioning AB. *Manuale dell'utente: Sentinel CT Room*. Document ID: SP-001-130627-010-16-IT-01. Uppsala, Sweden, May 2024.

[31] C-RAD Positioning AB. *System Manual: Sentinel*. Document ID: SP-001-070625-003-42. Uppsala, Sweden, 2023.

[32] Seonghee Kang et al. *Evaluation of initial patient setup methods for breast cancer between surface-guided radiation therapy and laser alignment based on skin marking in the Halcyon system*. In: *Radiation Oncology* 18 (2023), p. 60. DOI: `10.1186/s13014-023-02250-3`.

[33] C-RAD Positioning AB. *User's Guide: Catalyst®*. Document ID: SP-002-110916-001-28. Uppsala, Sweden, 2023.

[34] Elekta AB. *Elekta ONE – Medical Oncology*. 2025. URL: `https://www.elekta.com/products/oncology-informatics/elekta-one/oncology-care/medical-oncology/`.

[35] C-RAD Positioning AB. *System Manual: Catalyst®*. Document ID: SP-002-110918-001-30. Uppsala, Sweden, 2023.

[36] Avice M. O'Connell, David L. Conover, and Chuen-Fu Linda Lin. *Cone-Beam Computed Tomography for Breast Imaging*. In: *Journal of Radiology Nursing* 28.1 (2009), pp. 3–11. ISSN: 1546-0843. DOI: `https://doi.org/10.1016/j.jradnu.2008.12.003`.

[37] Susan G. Komen. *Age and Breast Cancer*. 2024. URL: `https://www.komen.org/breast-cancer/risk-factor/age/`.

[38] MIM Software Inc. *Mim Software Platform*. Cleveland, OH, USA. 2005. URL: `https://www.mimsoftware.com`.

[39] Philipp Freislederer et al. *Recent advances in Surface Guided Radiation Therapy*. In: *Radiation Oncology* 15.1 (2020), p. 187. DOI: `10.1186/s13014-020-01629-w`.

[40] Luis I. Cerviño et al. *Using surface imaging and visual coaching to improve the reproducibility and stability of deep-inspiration breath-hold for left-breast-cancer radiotherapy*. In: *Physics in Medicine and Biology* 54.22 (2009), pp. 6853–6865. DOI: `10.1088/0031-9155/54/22/023`.

[41] Abraham Savitzky and Marcel J. E. Golay. *Smoothing and Differentiation of Data by Simplified Least Squares Procedures*. In: *Analytical Chemistry* 36.8 (1964), pp. 1627–1639. DOI: `10.1021/ac60214a047`.

[42] Jiapu Pan and Willis J. Tompkins. *A Real-Time QRS Detection Algorithm*. In: *IEEE Transactions on Biomedical Engineering* BME-32.3 (1985), pp. 230–236. DOI: `10.1109/TBME.1985.325532`.

[43] Chuan Zeng et al. *A Potential Pitfall and Clinical Solutions in Surface-Guided Deep Inspiration Breath Hold Radiation Therapy for Left-Sided Breast Cancer*. In: *Advances in Radiation Oncology* 8.5 (2023), p. 101298. DOI: `10.1016/j.adro.2023.101298`.

[44] Vance Keeling et al. *Quantitative evaluation of patient setup uncertainty of stereotactic radiotherapy with the frameless 6D ExacTrac system using statistical modeling*. In: *Journal of applied clinical medical physics / American College of Medical Physics* 17 (May 2016), p. 5959. DOI: `10.1120/jacmp.v17i3.5959`.

[45] G. Carl et al. *Optical Surface Scanning for Patient Positioning in Radiation Therapy: A Prospective Analysis of 1902 Fractions*. In: *Technology in Cancer Research & Treatment* 17.1 (2018), p. 1533033818806002. DOI: `10.1177/1533033818806002`.

[46] Michalis Psarras et al. *Surface-Guided Radiotherapy: Can We Move on from the Era of Three-Point Markers to the New Era of Thousands of Points?* In: *Bioengineering* 10.10 (2023), p. 1202. DOI: `10.3390/bioengineering10101202`. URL: `https://doi.org/10.3390/bioengineering10101202`.

[47] Estelle Batin et al. *Can Surface Imaging Improve the Patient Setup for Proton Postmastectomy Chest Wall Irradiation?* In: *Practical Radiation Oncology* 6.6 (2016), e235–e241. DOI: `10.1016/j.prro.2016.02.001`.

[48] Mengjiao Liu et al. *Application of Optical Laser 3D Surface Imaging System (Sentinel) in Breast Cancer Radiotherapy*. In: *Scientific Reports* 10.1 (2020), p. 7550. DOI: `10.1038/s41598-020-64496-1`.

[49] Jiahao Zeng et al. *Evaluation of rotational setup errors in surface-guided radiation therapy for breast cancer patients*. In: *Journal of Applied Clinical Medical Physics* 22.12 (2021), pp. 154–162. DOI: `10.1002/acm2.13410`.

[50] Philips Healthcare. *Pinnacle Treatment Planning System – TPSwiki*. 2023. URL: `https://tpswiki.com/pinnacle:about/`.

[51] Amy Frederick et al. *Performance of a Knowledge-Based Planning Model for Optimizing Intensity-Modulated Radiotherapy Plans for Partial Breast Irradiation*. In: *Journal of Applied Clinical Medical Physics* 23.3 (2022), e13506. DOI: `10.1002/acm2.13506`.

[52] Jing Wang et al. *Is it possible for knowledge-based planning to improve intensity modulated radiation therapy plan quality for planners with different planning experiences in left-sided breast cancer patients?* In: *Radiotherapy and Oncology* 12 (1 2017), p. 85. DOI: `10.1186/s13014-017-0822-z`.

[53] Carolyn W. Taylor and Anna M. Kirby. *Cardiac Side-effects From Breast Cancer Radiotherapy*. In: *Clinical Oncology (Royal College of Radiologists)* 27.11 (2015), pp. 621–629. DOI: `10.1016/j.clon.2015.06.007`.

[54] Pierre Loap et al. *Optimization and auto-segmentation of a high risk cardiac zone for heart sparing in breast cancer radiotherapy*. In: *Radiotherapy and Oncology* 153 (2020), pp. 146–154. DOI: `10.1016/j.radonc.2020.09.044`.

[55] Nelson Tsz Cheong Fung et al. *Geometric and dosimetric consequences of intrafractional movement in single isocenter non-coplanar stereotactic radiosurgery*. In: *Radiation Oncology* 18.1 (2023). DOI: `10.1186/s13014-022-02195-z`.

[56] M. Hussein, C. H. Clark, and A. Nisbet. *Challenges in calculation of the gamma index in radiotherapy – Towards good practice*. In: *Physica Medica* 36 (2017), pp. 1–11. DOI: `10.1016/j.ejmp.2017.02.006`.

[57] Wenli Lu et al. *Optimizing the Region for Evaluation of Global Gamma Analysis for Nasopharyngeal Cancer (NPC) Pretreatment IMRT QA by COMPASS: A Retrospective Study*. In: *Frontiers in Oncology* 12 (2022), p. 859415. DOI: `10.3389/fonc.2022.859415`.

[58] Min Fu et al. *In Silico Studies of the Impact of Rotational Errors on Translation Shifts and Dose Distribution in Image-Guided Radiotherapy*. In: *Technology in Cancer Research Treatment* 22 (2023), pp. 1–10. DOI: `10.1177/15330338231168763`.

[59] RaySearch Laboratories. *Robust Optimization in RayStation – White Paper*. `https://www.raysearchlabs.com/media/publications/white-papers/robust-optimization-in-raystation/`. Accessed: 2025-08-09. 2022.